Probing large-scale structure with the SKAO and other cosmological surveys

UNIVERSITY *of the*
WESTERN CAPE

Jan-Albert Viljoen

Department of Physics and Astronomy
University of the Western Cape

This dissertation is submitted for the degree of
Philosophiae Doctor

January 2022
Supervisor: Prof. Roy Maartens

Declaration

I declare that **Probing large-scale structure with the SKAO and other cosmological surveys** is my own work, that it has not been submitted for any degree or examination in any other university, and that all the sources I have used or quoted have been indicated and acknowledged by complete references.

Signature

Jan-Albert Viljoen
January 2022

This thesis is based on the work done by the author who has been supervised by Prof. Roy Maartens, of the Physics & Astronomy Department, University of the Western Cape. In collaboration with my supervisor and others, I have published the following articles:

- [1] J. Fonseca, **J-A. Viljoen** and R. Maartens,
  Constraints on the growth rate using the observed galaxy power spectrum,
  JCAP **12** (2019) 028 [arXiv:1907.02975]

- [2] **J-A. Viljoen**, J. Fonseca and R. Maartens,
  Constraining the growth rate by combining multiple future surveys,
  JCAP **09** (2020) 054 [arXiv:2007.04656]

- [3] R. Maartens, J. Fonseca, S. Camera, S. Jolicoeur, **J-A Viljoen**, C. Clarkson,
  Magnification and evolution biases in large-scale structure surveys,
  JCAP **12** (2021) 009 [arXiv:2107.13401]

- [4] **J-A. Viljoen**, J. Fonseca and R. Maartens,
  Multi-wavelength spectroscopic probes: prospects for primordial non-Gaussianity and relativistic effects,
  JCAP **11** (2021) 010 [arXiv:2107.14057]

- [5] **J-A. Viljoen**, J. Fonseca and R. Maartens,
  Multi-wavelength spectroscopic probes: biases from neglecting light-cone effects,
  JCAP **12** (2021) 004 [arXiv:2108.05746]

Chapters 3-5 are based on these publications.

Acknowledgements

I would like to thank my supervisor and mentor Prof. Roy Maartens, his guidance was invaluable in reaching this milestone. I will fondly remember our frequent consultations on the court, and never forget the opportunities made available to me. Also, I thank Dr José Fonseca who have been of great assistance for a significant part of this journey, it was a pleasure working with you.

I dedicate this thesis to my family, without their love and support, I certainly would never have attained this momentous accomplishment.

To my mother Grace, for her endless care and relentless dedication to my personal and academic success. The years of effort finally pays off - "Mom, I made it!".

To my father Jan, who taught me not to give up on my dreams, and never gave up on me when times were tough.

To my grandparents, whose years of sacrifice didn't go unnoticed, which played a crucial role in where I am today. Ouma Anna Sophia, for your honesty and always wanting the best for your family; Oupa Altus, for your great wisdom and kind heartedness, who always saw the best in me. I hope I finally proved you right; Oupa Ken, for the song in your heart, sense of humour and great example of etiquette. Finally, I am no longer a student; And my favourite, Ouma Annetjie, who taught me the importance of love and positivity for a long and happy life. It's always a joy to see you and a privilege to still have you with us. - "Nou het ons ook 'n doktor in die familie".

To my Elena, for your love, ambition and constant support. You always motivate me to be a better person, and I'm looking forward to our journey together.

Abstract

In recent history there have been several advances in cosmology, which has significantly shaped our understanding of the Universe. The current leading theory is called ΛCDM, which can successfully model the expansion of the Universe from a primordial state and describe the dynamics of its contents, thereby resulting in the large-scale structure present today. The model is based on general relativity, that describes gravitational interaction as the curvature of a four-dimensional manifold called space-time. However, despite the many successes of ΛCDM, there are a number of things that need further investigation.

The Cosmic Microwave Background (CMB) is the oldest observable radiation in the Universe, and this cosmological relic contains a detectable structure. The process leading up to the CMB determines the initial conditions of ΛCDM, but is still poorly understood. It is widely accepted that inflation was responsible for the rapid expansion after the Big Bang, although this is yet to be verified experimentally. The distribution of the primordial potential is imprinted on ultra-large scales of the matter distribution, which offers an important insight into uncovering this mystery.

In addition to the primordial Universe, there are other concepts that still puzzle us in ΛCDM itself. The fact that we have been unable to directly detect and explain these dark components (that make up around 96% of the Universe) has prompted several theorists to consider alternative cosmological models. Therefore, testing general relativity and ΛCDM is still an essential part of cosmological research. A key observational discriminant between general relativity and modified theories of gravity is the rate at which the large-scale structure grows from small perturbations. The relativistic effects (or light-cone effects) expected in general relativity also offer an independent test of the gravitational model.

The present experiments are not extensive or sensitive enough to make detections that can result in a definitive conclusion, however great advancements are expected from the telescopes of tomorrow. The next-generation of cosmological surveys will observe larger cosmic volumes with greater sensitivity than ever before, enabling us to access more information on the primordial Universe, peculiar velocity fields, as well as

relativistic effects. In addition to probing deeper in redshift over a larger sky area, the surveys will also create complementary data sets of dark matter tracers. By combining the information from different observations via multi-tracer cross-correlations, we can suppresses cosmic variance and more precisely measure cosmological parameters.

The distribution of galaxies are analysed using the angular power spectrum. The C_ℓ is observed in redshift space, therefore it includes relativistic effects without approximation and avoids the need for an Alcock-Packzynski correction. It also naturally incorporates wide-angle effects, and cosmic evolution is included through relatively narrow redshift bin widths. We also include the cross-correlations between bins, and utilise a "hybrid approximation" when the total number of bins is computationally unfeasible.

We use a Fisher Matrix analysis to forecast constraints on cosmological parameters expected from future spectroscopic galaxy surveys. In our forecasts we only consider linear scales. We also consider the uncertainty of several parameters, by marginalising over the amplitude of primordial fluctuations, the dark energy equation of state parameter, the clustering bias in each redshift bin, as well as other standard cosmological parameters.

As opposed to an exhaustive study of future surveys, we attempt to fill the redshift range $0 < z \lesssim 3$ with the potentially best contemporaneous spectroscopic surveys. We considered large-scale structure surveys in the optical, near-infrared and radio. Specifically, the neutral Hydrogen (HI) surveys in radio from the Square Kilometre Array Observatory (SKAO), the optical galaxy survey of Dark Energy Spectroscopic Instrument's Bright Galaxy Sample (DESI BGS), as well as the Euclid-like Hα survey in near-infrared. We also consider the combination of these surveys, specifically two pairs of 21cm and galaxy surveys: one pair at low redshift and one at high redshift.

An exciting prospect for future surveys is the detection of a non-Gaussian distribution in the primordial potential field, i.e. non-zero $f_{\rm NL}$. The accurate measurement of $f_{\rm NL}$ will enable us to determine whether the early Universe originated from a single- or multi-field inflationary model. We forecast the expected precision on $f_{\rm NL}$ and find that the full combination of surveys could deliver $\sigma(f_{\rm NL}) \sim 1.5$.

The observed power spectrum includes relativistic effects, which in addition to testing gravity can produce a signal similar to primordial non-Gaussianity. Therefore, it is important to accurately model such influences and establish how well we can distinguish between $f_{\rm NL}$ and light-cone effects. We consider the detectability of lensing magnification and other relativistic effects. The result from the full survey combination

shows we can detect the Doppler effect with a signal-to-noise ratio ∼8, and measure the lensing convergence contribution at ∼2% precision.

Furthermore, we assess the bias on the best-fit values of $f_{\rm NL}$ and other cosmological parameters, from neglecting these light-cone effects. We conclude that lensing magnification at higher redshifts must be included in the modelling of spectroscopic surveys. If lensing is neglected in the analysis, this produces a bias of more than 1σ – not only on $f_{\rm NL}$, but also on the standard cosmological parameters.

General relativity and its classical modifications have distinctive effects on the clustering of galaxies and their peculiar velocities. This implies that the growth rate of large-scale structure provides a powerful consistency test of the standard cosmological model and a probe of possible deviations from general relativity. We extract information on the growth index γ via the observational effect of redshift space distortions. We show that the signal-to-noise on γ increases as the redshift bin-width is decreased. Shot noise per bin also increases – but this is compensated by the increased number of auto- and cross-spectra. Neglecting cross-bin correlations increases the errors by $\sim 40 - 150\%$. We find that a DESI-like BGS survey and an HI intensity mapping survey with the SKAO precursor MeerKAT deliver similar errors of $\sim 4 - 6\%$, while a Euclid-like survey and an SKAO intensity mapping survey give $\sim 3\%$ errors.

Additionally, we forecast constraints on the growth rate from a combination of next-generation spectroscopic surveys. In the overlap survey volumes, we use a multi-tracer analysis to significantly reduce the effect of cosmic variance. The non-overlap individual survey volumes are included in the Fisher Matrix analysis in order to utilise the entire observed volume. We find that combining the surveys improves the error on γ from the best single-tracer by up to ∼50%, delivering a precision of $\sim 1.3\%$.

Table of contents

Chapter 1

Introduction

Cosmology is a branch of astronomy dedicated to describing the Universe from its origin to the large-scale structures observed today. More specifically it describes the contents, geometry and dynamics of the cosmos, as well as how these properties evolve over time. In recent decades the scientific community has developed a well established theoretical model that can accurately describe the evolution of the Universe by using only 6 cosmological parameters, called ΛCDM or the standard model of cosmology. The model is named after the exotic components needed to explain the dynamics of the Universe: dark energy Λ accounts for the late time accelerated expansion, and Cold Dark Matter (CDM) is required to model the clustering of galaxies. Additionally, the model assumes that dark energy and dark matter are uncoupled. ΛCDM has been meticulously tested in different epochs on different physical scales, using a variety of cosmological probes.

The era of so-called "precision cosmology" started in the early 90's, when the Cosmic Background Explorer (COBE) detected the anisotropies on the Cosmic Microwave Background (CMB) [6]. In subsequent years, additional experiments were able to improve measurements of the temperature fluctuations on the surface of last scattering, which contributed a wealth of information to our understanding of the Universe. For example Wilkinson Microwave Anisotropy Probe (WMAP), Boomerang and most recently Planck [7–10]. Many of the best constraints on the ΛCDM result from the CMB measurements, but they are not exclusive.

Numerous cosmological surveys are underway or planned that probe the large-scale structure (LSS) of the Universe at much later times, such as Galaxy And Mass Assembly (GAMA), Sloan Digital Sky Survey (SDSS), Dark Energy Survey (DES) and Euclid, to mention a few [11–21]. These surveys are considering the spatial distribution of

galaxies, which are expected to be strongly correlated to the anisotropies observed in the CMB. Therefore all the data-sets are consistent with ΛCDM and we should be able to constrain this model by considering both early- and late-time probes.

The significant difference between the CMB and LSS is the number of scales one can possibly extract. The CMB signal originates from a thin shell produced around the epoch of recombination, whereas the LSS gives us a three-dimensional insight into the nature of the Universe. Therefore we expect to extract more cosmological information from the LSS as compared to the CMB, however, only recently the LSS has delivered constraints comparable to that of the CMB. The reason is that the instrumentation to date is not sensitive enough to utilise all the information available at late times.

We are entering a new era in the study of the large-scale structure of the Universe. Not only will we map the sky over larger areas, but we will also go much deeper in redshift. The increasing volumes would provide access to the ultra-large scales necessary to measure the effects of primordial non-Gaussianity in the large-scale structure, which is an important scientific driver of future surveys. Primordial non-Gaussianity of the different types (local, equilateral, folded) provides an exquisite window into the physics of the very early Universe (see e.g. [22] for a review). These types of primordial non-Gaussianity have been constrained by the Planck survey [10], which is the current state-of-the-art.

Einstein's theory of gravity and its modifications (see e.g. the reviews [23–25]) leave distinctive imprints on the clustering of matter and its peculiar velocity. Identifying the statistical effect of peculiar velocities on the distribution of matter provides a powerful test of the cosmological model as well as the theory of gravity. Furthermore, relativistic contributions, like lensing magnification and Doppler effect can also be used as independent tests of general relativity.

In addition to the growing volumes, we will also probe the sky in different frequency ranges, creating complementary sets of dark matter tracers. The multiple tracers can be combined by using the multi-tracer technique [26] to minimise the effect of cosmic variance. Although the technique was initially proposed to measure local primordial non-Gaussianity without cosmic variance, its potential to better constrain the growth rate of LSS was shown by [27]. Also, the multi-tracers proves a compelling method to extract information on contributions from light-cone effects, such as lensing and the Doppler effect.

The structure of the thesis is as follows: chapter 1 gives a brief overview of the standard cosmological model, growth of the large-scale structure and observational light-cone effects. The statistical methods applied to analyse the galaxy distributions is reviewed in chapter 2, as well as the multi-tracer technique and the Fisher Matrix analysis. The technical details of modelling cosmological surveys and which dark matter tracers we considered is described in chapter 3. In chapter 4 and chapter 5 we give the main results of the thesis, which are the constraints from future spectroscopic surveys and their combinations on: growth rate of large-scale structure formation, primordial non-Gaussianity and relativistic effects. The thesis is briefly summarised in chapter 6.

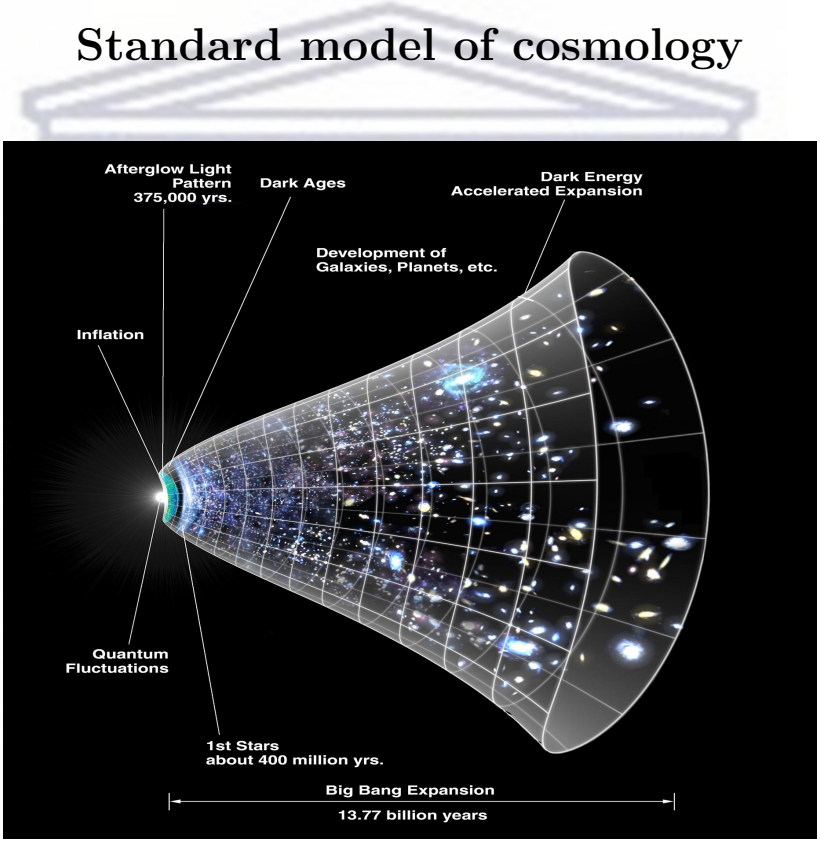

Fig. 1.1 An illustration of the expansion of the Universe assuming the standard cosmological model ΛCDM. Credit: Dana Berry, NASA/WMAP Science Team

The following section serves as a short review of the standard cosmological model and perturbation theory. We cover the primordial Universe up to large-scale structure formation, as well as the observational light-cone effects. For further details, please refer to the well-known textbooks of [28–30].

According to ΛCDM, the Universe is homogeneous and isotropic which presently consists of:

- **Baryons and photons (4%).** Only a small amount of the energy density in the Universe can be explained through ordinary atomic matter and radiation, such as baryons, photons and neutrinos.

- **Dark Matter (26%).** A significant portion is attributed to a hypothetical new particle (or set of particles), known as Dark Matter (DM). This type of matter has not been directly detected but have been inferred by gravitational interactions.

- **Dark Energy: (70%).** The remaining energy content is the vacuum energy Λ, which is responsible for the accelerated expansion of the Universe at late-times. This energy density is independent of time and referred to as the cosmological constant.

1.1 General relativity

The standard model of cosmology is based on General Relativity (GR) which links the geometry of the spacetime with the energy density contained in the Universe. The curvature of the four-dimensional manifold determines the geodesics and hence trajectory of free-falling particles. This information is contained within the Einstein tensor

$$G_{\mu\nu} = R_{\mu\nu} - \frac{1}{2} R\, g_{\mu\nu}\,, \tag{1.1}$$

where the spacetime metric is denoted by $g_{\mu\nu}$. This tensor is conserved under the covariant derivative by construction: $G^{\nu}_{\mu;\nu} = 0$. Einstein's tensor is expressed in terms of the Ricci tensor

$$R_{\mu\nu} = R^{\alpha}_{\mu\alpha\nu} = -R^{\alpha}_{\mu\nu\alpha} \tag{1.2}$$

and Ricci scalar

$$R = R_{\mu\nu} g^{\mu\nu}\,, \tag{1.3}$$

which are computed from the contraction of Riemann curvature tensor of the manifold:

$$R^{\mu}_{\nu\alpha\beta} = \partial_{\alpha}\Gamma^{\mu}_{\nu\beta} - \partial_{\beta}\Gamma^{\mu}_{\nu\alpha} + \Gamma^{\mu}_{\sigma\alpha}\Gamma^{\sigma}_{\nu\beta} - \Gamma^{\mu}_{\sigma\beta}\Gamma^{\sigma}_{\nu\alpha}\,. \tag{1.4}$$

The Christoffel symbol in the above equation is expressed in terms of the metric:

$$\Gamma^{\mu}_{\alpha\beta} = \frac{1}{2} g^{\mu\nu} \left(g_{\nu\alpha,\beta} + g_{\nu\beta,\alpha} - g_{\beta\alpha,\nu} \right)\,. \tag{1.5}$$

The dynamics of the contents of the Universe can be approximated by assuming that it is described by a perfect cosmological fluid. Therefore the energy-momentum

tensor depends only on the pressure p and density ρ of the fluid:

$$T_{\mu\nu} = \rho\, u_\mu u_\nu + p\,(u_\mu u_\nu + g_{\mu\nu})\ , \tag{1.6}$$

in the background the four-velocity $u^\mu = \delta^\mu_0$, and the conservation of energy and momentum is imposed by setting $T^\nu_{\mu;\nu} = 0$. The theory of GR is defined by the Einstein field equations (EFE):

$$G_{\mu\nu} = 8\pi G\, T_{\mu\nu}\,, \tag{1.7}$$

where G is Newton's gravitational constant, and we use units where the speed of light is $c = 1$, unless otherwise specified. Therefore the gravitational potential of the Newtonian limit is recovered in the weak field and slow motion approximation. The implication of (1.7) is that not only does the curvature of spacetime determine the motion of the cosmological fluid, but the energy density of the fluid itself influences the geometry of spacetime.

1.2 Friedmann equations

The Cosmological Principle (CP) states that the spatial distribution of matter in the Universe is statistically homogeneous and isotropic when viewed on large enough scales. The implication of the CP is that the spacetime manifold is spherically symmetric, and expands in all directions equally according to a scale factor $a(t)$. In a flat Universe we can express such a metric as

$$ds^2 = -dt^2 + a^2(t)\Big(dx^2 + dy^2 + dz^2\Big)\,, \tag{1.8}$$

which is known as the Friedmann, Lemaître, Robertson and Walker (FLRW) metric [31]. The expansion of the Universe is denoted by the Hubble rate, which is defined as the rate of change of the scale factor with respect to time, such that $H = \dot{a}/a$ in units of $\mathrm{km\,s^{-1}Mpc^{-1}}$. In a conformal coordinate system the Hubble rate is

$$\mathcal{H} = \frac{a'}{a} = aH, \tag{1.9}$$

where the prime denotes the derivative with respect to conformal time $\mathrm{d}\eta = a^{-1}\mathrm{d}t$. The dynamics of the background expansion of a spatially flat Universe can be computed

using (1.7), which results in the set of Friedmann equations:

$$\begin{aligned}\mathcal{H}^2 &= \frac{8\pi G}{3}\rho a^2 + \frac{\Lambda}{3}a^2\,,\\ \mathcal{H}' &= -\frac{8\pi G}{6}a^2(\rho + 3p) + \frac{\Lambda}{3}a^2\,,\\ \rho' &+ 3\mathcal{H}(\rho + p) = 0\,.\end{aligned} \tag{1.10}$$

In ΛCDM, the contribution from Dark Energy (DE) is assumed constant and denoted by Λ. It is often convenient to express the energy density of each component i in terms of the unitless energy density: $\Omega_i = \rho_i/\rho_c$, where $\rho_c = 3H^2/(8\pi G)$ is known as the critical density. The total energy density of the Universe is therefore

$$\Omega_{\rm tot} \equiv \frac{8\pi G\rho}{3H^2} + \frac{\Lambda}{3H^2} = \Omega_{\rm m} + \Omega_\Lambda = 1\,. \tag{1.11}$$

The surveys that we are considering in this thesis are observing a period significantly later than the matter-radiation equality, therefore we can safely neglect the contribution of radiation from photons and neutrinos. Note that the matter density is a combination of visible baryonic matter and cold DM: $\Omega_{\rm m} = \Omega_{\rm cdm} + \Omega_b$. Let the present-time parameter values be denoted by the subscript 0. The evolution of the expansion of the Universe is expressed in terms of the well known form of the Hubble rate

$$H^2(a) = H_0^2\left(\Omega_{\rm m0}\, a^{-3} + \Omega_{\Lambda 0}\right)\,. \tag{1.12}$$

1.3 Redshift, distance and volume

During the expansion of the Universe the electromagnetic radiation is stretched, which alters the wavelength of the emission. Let us consider the wavelength of an emission λ_e, which is detected by the observer as λ_o, then the redshift is defined in terms of the ratio of these quantities

$$1 + z = \frac{\lambda_o}{\lambda_e}\,. \tag{1.13}$$

The redshift is related to the scale factor via $a = (1+z)^{-1}$, hence serves as an indicator of both the distance to the source, as well as the time when the photon was emitted.

A vital part of cosmology is to accurately determine distances to the objects being observed. The proper distance Δs is the magnitude the of separation between two four-positions Δx at a constant time $\Delta t = 0$, computed using the metric i.e. FLRW in

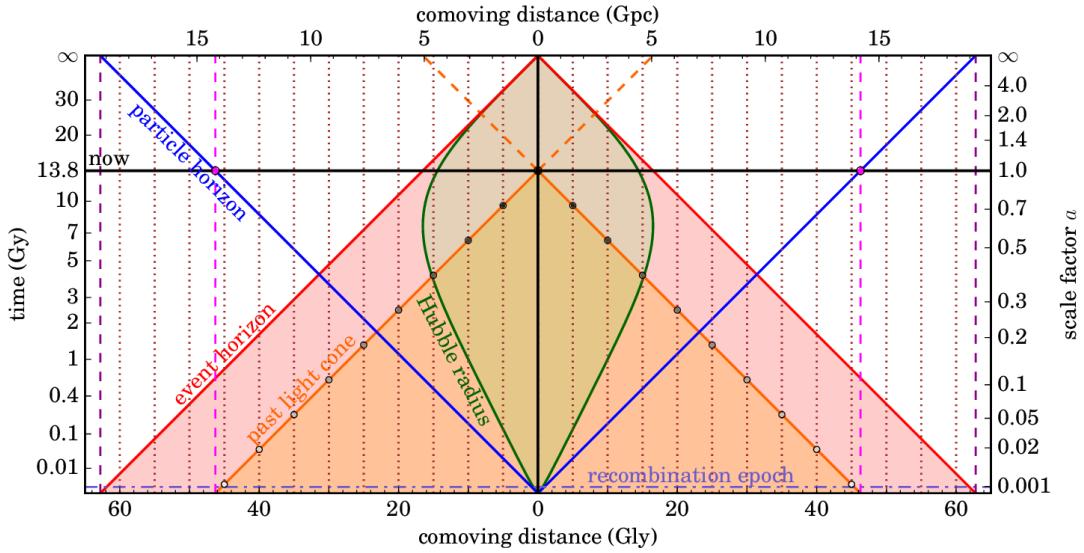

Fig. 1.2 The comoving distance (*x-axis*) as a function of scale factor (*y-axis*) given in conformal coordinates. The past light-cone (*orange*) indicates the current observable Universe. The event horizon (*red*) and particle horizon (*blue*) limits possible interactions. The Hubble radius cH^{-1} is shown in *green*. Based on Figure 1 in [32].

ΛCDM (1.8). The proper distance is dependent on the scale factor and hence cosmic time, therefore at the moment when the photons are detected this distance has likely changed significantly. Practically, we are more interested in where the source is at present-time. This notion leads us to the necessity to distinguish between *proper* and *comoving* distance.

The comoving distance χ enables us to factor out the expansion of the Universe by considering infinitesimal radial displacements along the light-ray, therefore providing a measure of distance that is independent of time

$$\chi(z) = \int_0^z \frac{c\,\mathrm{d}z'}{H(z')}\,. \tag{1.14}$$

The comoving distance in conformal coordinates is illustrated in Figure 1.2. A light-like interval is defined by the spacetime interval $\Delta s^2 = 0$, since by (1.8) the distance covered $\Delta x = c\Delta t$. Information cannot propagate faster than the speed of light and therefore an observer cannot perceive anything beyond this boundary. If the proper distance between source and observer exceeds the Hubble radius cH^{-1} (*green*), the photons will not be detected. This separation is the threshold at which spacetime expands at the speed of light. The particle horizon (*blue*) is the maximum distance an emitted photon can travel in a given time.

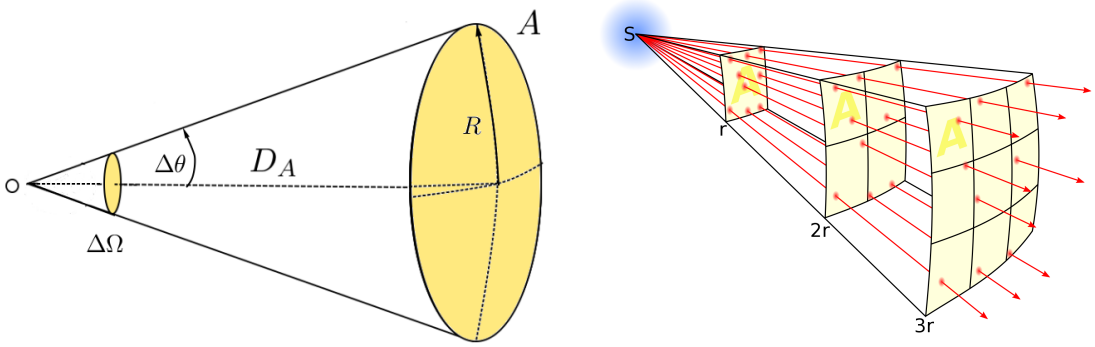

Fig. 1.3 *Left*: The angular diameter distance D_A to an object with surface area A subtends a solid angle of $\Delta\Omega$. *Right*: The observed flux is inversely proportional to r^2, which enables us to infer the luminosity distance D_L to standard candles[1].

Intuitively we all know that the further away an object is the smaller it will appear, since the angle of incidence from the incoming light-ray is reduced. From this principle one can infer the range to an object provided that we know the size of the target beforehand. An object with know size is referred to as *standard ruler*. Let us consider a distant object of proper area A subtend a solid angle $\Delta\Omega$ at the observer, as in Figure 1.3 (*left*), then the comoving angular diameter distance D_A is defined by

$$D_A^2 = \frac{A}{\Delta\Omega}\,. \tag{1.15}$$

In FLRW cosmology D_A is related to the comoving distance by

$$D_A(z) = \frac{\chi(z)}{1+z}\,, \tag{1.16}$$

where the $(1+z)$ factor takes into account the expansion of the Universe in the traversal direction.

Alternatively, we can determine the range to a source via the luminosity distance D_L. This method is based on the principle that a receding emitter will appear fainter with increasing distance. Consider a fixed number of photons homogeneously distributed on a spherical shell of radius r, radiated by a source of luminosity L. As the photons propagate through spacetime, the surface area of the sphere increases and hence the number of photons per area is reduced, see Figure 1.3 (*right*). The surface energy density of the photons is referred to as flux F, which is related to L by the surface

[1] Credit: https://commons.wikimedia.org/w/index.php?curid=3816716

area of a sphere

$$F = \frac{L}{4\pi r^2} \quad \text{in units of} \quad \frac{\text{ergs}\,\text{s}^{-1}}{\text{cm}^2}\,. \tag{1.17}$$

Therefore if the luminosity of the source is known, we can infer the distance to the so-called *standard candle* by measuring the flux at the observer. This distance is referred to as luminosity distance $D_L \equiv r$, which is related to the comoving distance by

$$D_L(z) = (1+z)\,\chi(z)\,. \tag{1.18}$$

Note that flux is measured in $\text{ergs}\,\text{s}^{-1}/\text{cm}^2$ and the luminosity is measured in $\text{ergs}\,\text{s}^{-1}$, therefore since D_L has units of Mpc, one has to covert units Mpc to cm in (1.17)[2].

The proper volume element $\mathrm{d}\mathcal{V}$ at the source is related to the observed volume via

$$\frac{\mathrm{d}\mathcal{V}}{a^3} = \frac{\chi^2}{H}\mathrm{d}z\,\mathrm{d}\Omega_o\,. \tag{1.19}$$

The sky area of a survey Ω_{sky} is frequently referred to in terms of the fraction of sky observed, $f_{\text{sky}} = \Omega_{\text{sky}}/4\pi$. The comoving volume of a redshift bin centered at z_i with a bin-width Δz is given by

$$\mathcal{V}_c(z_i, \Delta z) = 4\pi f_{\text{sky}} \int_{\chi_a}^{\chi_b} \chi^2\,\mathrm{d}\chi\,, \tag{1.20}$$

where the limits of integration correspond to the boundaries of the z-bin. Explicitly,

$$\chi_a = \chi\,(z_i - \Delta z/2) \quad \text{and} \quad \chi_b = \chi\,(z_i + \Delta z/2)\,.$$

1.4 Perturbation theory

The approximation of isotropy and homogeneity becomes increasingly ineffective as we transition to smaller scales. However, the small deviations from the FLRW background that make up the LSS may be modelled using linear perturbation theory.

The term perturbation hails from the Latin verb *turbare*, which means "to trouble" or "to disturb". The prefix *per* amplifies the action, so *perturbare* means to thoroughly trouble, or to disturb severely. In fluid mechanics, any solution θ of the fluid equations that is slightly altered from some background solution $\bar{\theta}$, is said to be a perturbation of the original solution,

$$\theta(\eta, \boldsymbol{x}) = \bar{\theta}(\eta) + \delta\theta(\eta, \boldsymbol{x})\,. \tag{1.21}$$

[2] $1\text{Mpc} = 3.086 \times 10^{24}$ cm

1.4.1 Perturbed Einstein field equations

The evolution of the density perturbations that describes the growth of LSS formation is also computed using EFE (1.7). In this case we use the perturbed FLRW metric, which in the Newtonian gauge is defined as:

$$ds^2 = a^2(\eta)\Big[-\Big(1+2\Phi\Big)d\eta^2 + \Big(1-2\Psi\Big)\delta_{ij}\,dx^i dx^j\Big]\,, \tag{1.22}$$

given the gravitational potential Φ and curvature perturbation Ψ. In this model there is no matter anisotropic stress and therefore $\Phi = \Psi$. The perturbed part of the Einstein tensor (1.1) is

$$\delta G_{\mu\nu} = \delta R_{\mu\nu} - \frac{1}{2}\Big(\bar{g}_{\mu\nu}\,\delta R + \bar{R}\,\delta g_{\mu\nu}\Big) \tag{1.23}$$

such that

$$\begin{aligned}
\delta G_{00} &= 2\nabla^2\Phi - 6\mathcal{H}\Phi'\,,\\
\delta G_{0i} &= 2\partial_i\Big(\Phi' + \mathcal{H}\Phi\Big)\,,\\
\delta G_{ij} &= \Big[2\Phi'' + 6\mathcal{H}\Phi' + 4\Big(2\mathcal{H}' + \mathcal{H}^2\Big)\Phi\Big]\delta_{ij}\,.
\end{aligned} \tag{1.24}$$

The perturbed energy-momentum tensor is

$$\delta T^\mu_\nu = (\delta\rho + \delta p)\,\bar{u}^\mu\bar{u}_\nu + (\bar{\rho}+\bar{p})\,(\bar{u}^\mu\,\delta u_\nu + \bar{u}_\nu\,\delta u^\mu) + \delta p\,\delta^\mu_\nu\,, \tag{1.25}$$

therefore

$$\delta T^0_0 = -\delta\rho\,, \quad \delta T^0_i = (\bar{\rho}+\bar{p})\partial_i V\,, \quad \delta T^i_j = \delta p\,\delta^i_j\,. \tag{1.26}$$

In the ΛCDM model $\bar{p} = 0 = \delta p$, and the velocity potential V is related to the velocity vector field v_i via

$$\partial_i V = v_i\,. \tag{1.27}$$

The matter density contrast $\delta_{\rm m}$ is a convenient way to express the deviation from the FLRW background solution. At position $\boldsymbol{x}$ and conformal time η, we define

$$\delta_{\rm m}(\eta,\boldsymbol{x}) = \frac{\rho(\eta,\boldsymbol{x}) - \bar{\rho}(\eta)}{\bar{\rho}(\eta)}\,. \tag{1.28}$$

For an observer, it is more useful to compute the density contrast in a comoving reference frame. Therefore we define the comoving matter density contrast as

$$\Delta_{\rm m} \equiv \delta_{\rm m} + \frac{\bar{\rho}'_{\rm m}}{\bar{\rho}_{\rm m}} V_{\rm m} = \delta_{\rm m} - 3\mathcal{H}V_{\rm m} \,. \tag{1.29}$$

By $T^{\nu}_{\mu;\nu} = 0$, the continuity and the Euler equation become

$$\Delta'_{\rm m} = -\nabla^2 V_{\rm m} \,, \tag{1.30}$$

$$V'_{\rm m} + \mathcal{H}V_{\rm m} = -\Phi \,. \tag{1.31}$$

In ΛCDM we assume that dark energy remains unperturbed, thus DE is only included in the background. Equating the Einstein tensor (1.23) and energy-momentum tensor (1.26), the perturbed field equations read

$$\delta G_{\mu\nu} = 8\pi G \delta T_{\mu\nu} \,, \tag{1.32}$$

such that the evolution of the perturbations are given by:

$$\begin{aligned} \text{Poisson}: \quad & \nabla^2\Phi = 4\pi G a^2 \bar{\rho}_{\rm m} \Delta_{\rm m} \,, \\ \text{momentum constraint}: \quad & \Phi' + \mathcal{H}\Phi = -4\pi G a^2 \bar{\rho}_{\rm m} V_{\rm m} \,, \\ \text{Bardeen}: \quad & \Phi'' + 3\mathcal{H}\Phi' + \Lambda^2\Phi = 0 \,. \end{aligned} \tag{1.33}$$

The Poisson equation can be expressed in unitless matter density (1.11) such that

$$\nabla^2\Phi = \frac{3}{2}\,\Omega_{\rm m}\mathcal{H}^2\Delta_{\rm m} \,, \tag{1.34}$$

therefore we can find the evolution of the density contrast by taking the time derivative of (1.30) and substituting in (1.31):

$$\Delta''_{\rm m} + \mathcal{H}\Delta'_{\rm m} - \frac{3}{2}\Omega_{\rm m}\mathcal{H}^2\Delta_{\rm m} = 0 \,. \tag{1.35}$$

1.4.2 The primordial universe

The Cosmic Microwave Background radiation (CMB) is the relic that bears the imprint of the primordial inhomogeneities in the density field, which can still be detected in the form of temperature fluctuations. The anisotropies measured in the CMB (of the order of only 10^{-5}K) have evolved into the present-day LSS as a result of gravitational

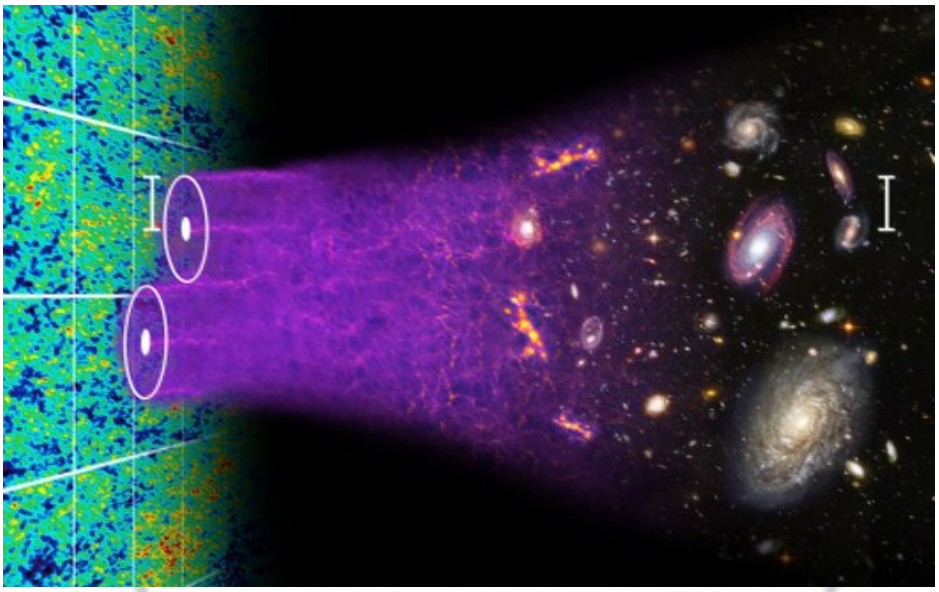

Fig. 1.4 Primordial temperature fluctuations on the surface of last scattering lead to the LSS we observe today. Credit: C. Blake and S.Moorfield

interaction, as illustrated in Figure 1.4. At later times, the signature of the primordial anisotropies are no longer available on small scales, due to the non-linear nature of small scale structure formation. However, the signal remains intact on ultra-large scales where structure formation remains linear. More detailed information on the very early Universe can be found in [33].

Due to the vast range of physical scales in the universe it is often more convenient to perform the statistical analysis of the matter distribution in Fourier space (or frequency space) as opposed to real space. The details of the Fourier transformation will be discussed in subsection 2.1.1, for now note that in Fourier space different scales are represented by $\boldsymbol{k}$, which have units of Mpc^{-1}, i.e. smaller values represent larger scales.

An interesting possibility is that the primordial potentials do not follow a Gaussian distribution. Inflation is the leading theory that describes the beginning of the universe and the origin of primordial curvature perturbations [34–37], which requires only a single scalar field to be consistent with current data. However, there is no theoretical basis for this assumption, and in fact, some fundamental physics models actually prefer multiple scalar fields (e.g. [38, 39]). The critical test required to distinguish between the different models is measuring the distribution of primordial potential and its deviation from Gaussianity.

Let us consider the local-type deviation from Gaussianity in the gravitational potential of the primordial curvature perturbation:

$$\Phi = \varphi + f_{\rm NL}\left(\varphi^2 - \langle\varphi^2\rangle\right) , \tag{1.36}$$

where φ is the first order Gaussian perturbation and $f_{\rm NL}$ is an indicator of deviations thereof. Primordial Non-Gaussianity (PNG) would imply that $f_{\rm NL} \neq 0$, which induces a large-scale modulation of the small-scale formation of haloes in the cold dark matter. The result produces a scale and redshift dependence in the halo bias (or clustering bias), which relate the observed galaxies to the underlying dark matter distribution. The correction to the clustering bias is given by a simple model [40–43], defined physically in the common rest frame of galaxies and dark matter:

$$\delta_{\rm g}(\boldsymbol{k}, z) = b(z)\,\Delta_{\rm m}(\boldsymbol{k}, z) + 2 f_{\rm NL}\,\delta_{\rm crit}\Big[b(z) - 1\Big]\varphi(\boldsymbol{k}, z) . \tag{1.37}$$

The scale-independent linear clustering bias is denoted by b, and $\delta_{\rm crit} = 1.686$ is the threshold density contrast for spherical collapse. In [44–46] they show that this model requires some improvement, but we will use the simplified model (1.37).

The primordial potential is related to the observed matter density contrast by linear evolution (see [47, 48] for details). Following the CMB convention of $f_{\rm NL}$:

$$\delta_{\rm g}(\boldsymbol{k}, z) = \left[b(z) + 3 f_{\rm NL}\,\frac{\delta_{\rm crit}\Big[b(z) - 1\Big] D(z_{\rm d})(1 + z_{\rm d})\,\Omega_{\rm m0} H_0^2}{D(z)\,T(k)\,k^2}\right]\Delta_{\rm m}(\boldsymbol{k}, z) , \tag{1.38}$$

where $z_{\rm d}$ is a redshift deep in the matter-dominated era. Note that the growth factor $D(z)$ and transfer function $T(k)$ are normalised to unity at present-day and on ultra-large scales respectively. The various inflationary models have different requirements for the distribution of primordial potential and therefore measuring $f_{\rm NL}$ will play an important role in discerning between them. The state-of-the-art constraint on the local-type primordial non-Gaussianity parameter $f_{\rm NL}$ is provided by Planck [10]:

$$f_{\rm NL} = -0.9 \pm 5.1 , \tag{1.39}$$

at 68% CL. Many single-field models are ruled out at $f_{\rm NL} \sim 1$. Therefore, being able to measure PNG with a precision of $\sigma(f_{\rm NL}) \lesssim 1$ is an exciting prospect for future cosmological surveys [49].

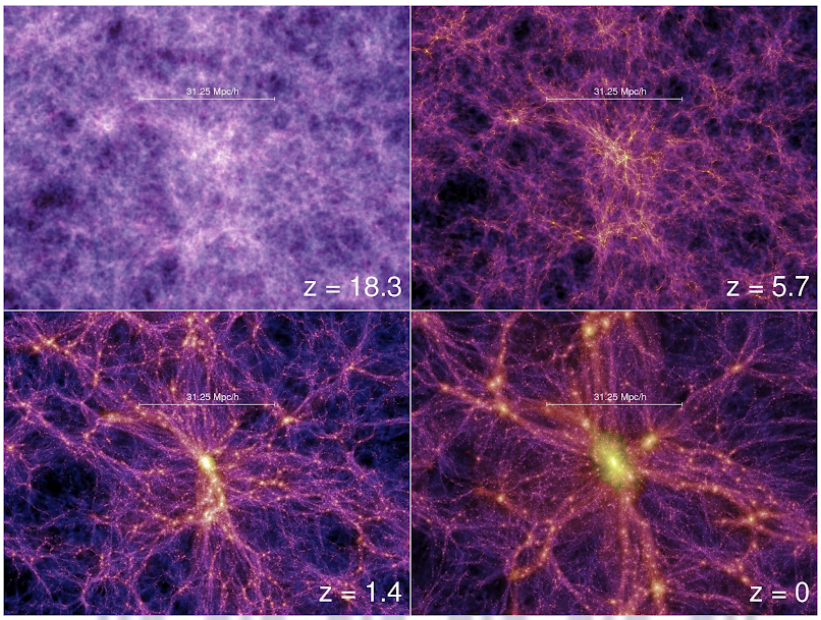

Fig. 1.5 A computer simulation of the evolution of the large scale structure of the Universe, i.e. the formation of the so-called cosmic web. Credit: [50]

1.4.3 Large-scale structure formation

The rate at which the LSS grows from small perturbations is illustrated in Figure 1.5, which offers a key observational discriminant between different cosmological (and hence gravitational) models [51, 52]. A variety of gravitational theories predict almost an indistinguishable background evolution and therefore, in order to discern between models of gravity, it is necessary to also consider the clustering of matter. The density contrast evolves over time via the growth factor D:

$$\Delta_{\rm m}(\eta, \boldsymbol{x}) = D(\eta)\, \Delta_{\rm m}(\eta_0, \boldsymbol{x})\,. \tag{1.40}$$

This factor is used to define the linear growth rate of large-scale structure formation,

$$f = \frac{1}{\mathcal{H}} \frac{D'}{D} = \frac{d \ln D}{d \ln a} \quad \Rightarrow \quad \Delta'_{\rm m} = f \mathcal{H} \Delta_{\rm m}\,. \tag{1.41}$$

Hence, by (1.35), the evolution of f is

$$\frac{{\rm d}f}{{\rm d}\ln a} + \frac{1}{2}\,(4 - 3\Omega_{\rm m})\, f + f^2 = \frac{3}{2}\Omega_{\rm m}\,. \tag{1.42}$$

The growth rate can be parameterised in terms of the matter density of the universe using a power-law [53]

$$f(\eta) = \Omega_{\rm m}(\eta)^{\gamma}\,, \tag{1.43}$$

where the exponent denotes the *growth index* and is assumed to be constant in ΛCDM. Although this does not allow for scale-dependence of the growth rate, it still delivers a consistency test of ΛCDM and standard dark energy models. A significant deviation from $\gamma = 0.55$ would indicate a breakdown of the standard model, as a result of either non-standard dark energy or modified gravity. For a review on modified theories of gravity see [54].

1.5 Observed density contrast

The observed number density contrast $\Delta_{\rm g}$ is given by the contrast at the source $\delta_{\rm g}$, modulated not only by redshift space distortions, but also by the Doppler effect, lensing magnification and other relativistic effects. The observed number of galaxies in a direction $\boldsymbol{n}$ within solid angle $\mathrm{d}\Omega_{\boldsymbol{n}}$ and redshift interval $\mathrm{d}z$ is

$$\mathrm{d}\mathbb{N}_{\rm g} = N_{\rm g}\,\mathrm{d}z\,\mathrm{d}\Omega_{\boldsymbol{n}} = n_{\rm g}\,\mathrm{d}\mathcal{V}\,. \tag{1.44}$$

Here $N_{\rm g}$ is the angular number density per redshift as measured by the observer. On the other hand, $n_{\rm g}$ is the number density and $\mathrm{d}\mathcal{V}$ is the volume element, which are not observed, since they are quantities at the emitting source.

The observed number density contrast is given by [43]

$$\Delta_{\rm g}(z, \boldsymbol{n}, F_c) = \frac{N_{\rm g}(z, \boldsymbol{n}, F_c) - \bar{N}_{\rm g}(z, F_c)}{\bar{N}_{\rm g}(z, F_c)}\,, \tag{1.45}$$

where F_c is the survey flux cut. The observed number density contrast in the Newtonian gauge is related to the comoving number density contrast at the source, $\delta_{\rm g} = b\,\Delta_{\rm m} = (n_{\rm g} - \bar{n}_{\rm g})/\bar{n}_{\rm g}$, via redshift-space (light-cone) effects:

$$\Delta_{\rm g} = \delta_{\rm g} + \Delta^{\rm RSD} + \Delta^{\rm Dopp} + \Delta^{\rm Lens} + \Delta^{\rm Pot}\,. \tag{1.46}$$

The Δ terms on the right are now described individually.

1.5.1 Redshift Space Distortions

The growth rate is increasingly better constrained via Redshift Space Distortions (RSD) and other peculiar velocity measurements, and one can model RSD on large scales using linear cosmological perturbation theory [55]. RSD is as a result of how we infer distance to an emitter using the redshift. The Hubble redshift of a galaxy is not only influenced by the background expansion (1.13), but is also modified by a Doppler correction due to the peculiar velocitiy $\boldsymbol{v}$ of the source. We observe the position of the galaxy as a combination of the two in redshift space. Consequently the observed position is given by [40]

$$\boldsymbol{x}_{\rm obs} = \boldsymbol{x} + \frac{\boldsymbol{v}\cdot\boldsymbol{n}}{\mathcal{H}}, \tag{1.47}$$

where $\boldsymbol{n}$ is a unit vector denoting the line-of-sight. Therefore, galaxies moving towards the observer will appear closer and conversely, receding galaxies will appear further away. Note that velocities in the traversal direction do not influence the observed position. The diagram in Figure 1.6 illustrates this principle for three distinct cases:

- **Linear regime:** At large scales, the peculiar velocity of an infalling shell is small compared to its radius, hence induce only a slight distortion in observed space. This scenario is easy to model using linear perturbation theory, which will be the focus of this work.
- **Turnaround:** In this configuration the peculiar velocity is just cancelling the general Hubble expansion, which appears collapsed to a single velocity in redshift space.
- **Non-linear regime:** Inside the shell of the turnaround point, the peculiar velocities of galaxies are large compared to the radius of the shell. Due to the extreme distortion the collapsing galaxies in real space appear turned "inside out" in redshift space.

The conservation of galaxy number counts enable us to relate (1.47) to the observed matter density contrast with the RSD correction, called the Kaiser formula [57]:

$$\Delta^{\rm RSD}(z,\boldsymbol{n}) = -\frac{1}{\mathcal{H}(z)}\boldsymbol{n}\cdot\nabla\Big[\boldsymbol{n}\cdot\boldsymbol{v}(z,\boldsymbol{n})\Big]\,. \tag{1.48}$$

Redshift surveys allow us to simultaneously measure the cosmic expansion history and growth rate of structure formation, by statistically analysing the three-dimensional clustering of galaxies [58]. To completely model the effect of RSD we also need to consider a "dispersion model", which includes a damping effect in addition to the Kaiser formula [59]. The small-scale damping takes into account a non-linear effects, which is beyond the scope of this thesis. Figure 1.7 illustrates the difference between

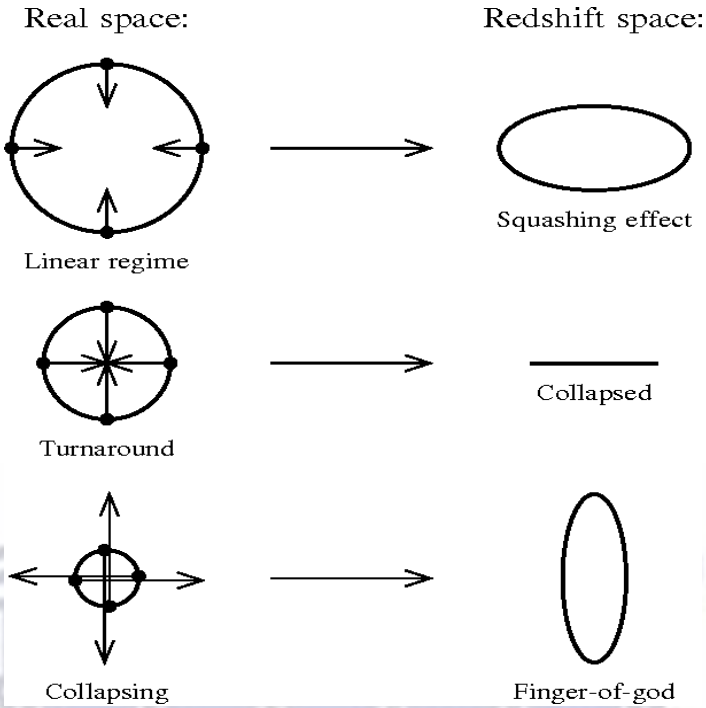

Fig. 1.6 The true position and velocity of a galaxy in real space (*left*), and the corresponding position observed in redshift space (*right*). The line-of-sight of the detector extends from the bottom to the top of the diagram. Credit: [56]

the observed density contrast $\Delta_{\rm g}$ in redshift space (*left*) and the actual baryonic matter distribution $\delta_{\rm g}$ after RSD have been corrected for (*right*).

1.5.2 Doppler effect

The Doppler term $\Delta^{\rm Dopp}$ in (1.46) is sourced by radial peculiar velocities. This not only affects the measured redshift, but it also has a (de-)magnification effect on galaxies [60]:

$$\Delta^{\rm Dopp}(z, \boldsymbol{n}, F_c) = A_{\rm D}(z, F_c)\, \boldsymbol{n} \cdot \boldsymbol{v}(z, \boldsymbol{n})\,, \tag{1.49}$$

which scales as $\Delta^{\rm Dopp} \sim \delta_{\rm m}\, H_0/k$ in Fourier space, and is only non-negligible on ultra-large scales. The amplitude of the Doppler term is

$$A_{\rm D}(z, F_c) = \frac{\left[5s(z, F_c) - 2\right]}{\mathcal{H}(z)\chi(z)} - 5s(z, F_c) + b_{\rm e}(z, F_c) + \frac{{\rm d}\ln \mathcal{H}(z)}{{\rm d}\ln(1+z)}, \tag{1.50}$$

where the s and $b_{\rm e}$ in (1.50) is the magnification bias and evolution bias respectively, which will be defined later in section 3.3. Roughly speaking, the magnification bias is the change in the galaxy number density with respect to the luminosity cut at fixed redshift,

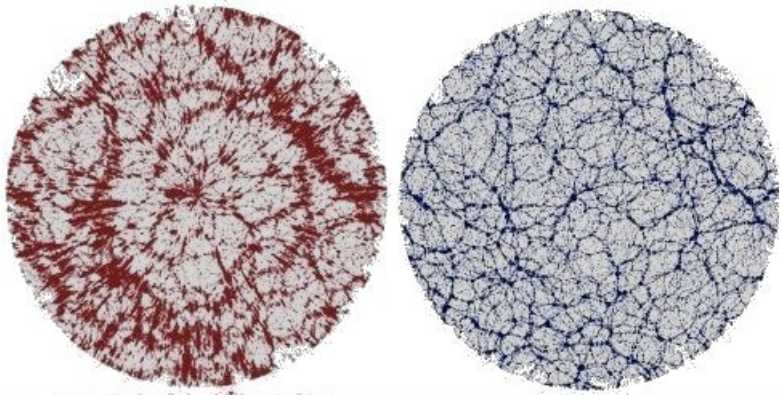

Fig. 1.7 The matter distribution observed in redshift space (*left*), as opposed to the true matter distribution (*right*). Credit: Hume A. Feldman

which is survey dependent. The evolution bias is the change in comoving number density with respect to redshift at fixed luminosity cut, which is tracer dependent. Halo and galaxy formation and evolution lead to a non-conserved comoving number density (e.g. due to mergers), that is reflected in nonzero $b_{\rm e}$, which then modulates the Doppler contribution.

Note also that part of the Doppler term, i.e. $(1+z)(5s-2)\,\boldsymbol{v}\cdot\boldsymbol{n}/(\chi H)$, is a Doppler contribution to lensing magnification, arising from the apparent radial displacements related to redshift perturbations, $\delta z = (1+z)\boldsymbol{v}\cdot\boldsymbol{n}$ [40] (see also [60–63]).

The Doppler contribution in the power spectrum [40, 43, 63–66], and even more in the cross-power spectrum of two tracers [67–73] and in the bispectrum of a single tracer [74–77], is a powerful and independent probe of gravity.

1.5.3 Lensing magnification

The large-scale gravitational lensing convergence contribution to the number density contrast in (1.46) is denoted by:

$$\begin{aligned}\Delta^{\rm Lens}(z,\boldsymbol{n}) &= A_{\rm L}(z,F_c)\,\kappa(z,\boldsymbol{n})\\ &= \big[5s(z,F_c)-2\big]\int_0^{\chi(z)}{\rm d}\tilde{\chi}\,\frac{\big[\chi(z)-\tilde{\chi}\big]}{\chi(z)\,\tilde{\chi}}\,\nabla^2_{\boldsymbol{n}}\Phi(\tilde{\chi},\boldsymbol{n})\,,\end{aligned} \tag{1.51}$$

where Φ is the Bardeen potential. Since κ is a line-of-sight integral over a weighted matter density contrast $\delta_{\rm m}$, the lensing term scales as $\Delta^{\rm Lens}\sim\delta_{\rm m}$. This means that the lensing term is partially degenerate with the Gaussian clustering bias b in $\delta_{\rm g}$.

For an idealised survey that detects all galaxies (i.e. $s = 0$), a positive κ in (1.51) decreases the observed number density contrast by increasing the solid angle. In a real survey, s is positive, and the effect of magnification bias when $\kappa > 0$ is to increase the observed number density contrast – since galaxies below the luminosity cut can be brightened by lensing and thus be observed. Similarly, when $\kappa < 0$, the effect of s is to reduce the number density contrast by de-magnifying galaxies that are above the luminosity threshold.

The lensing magnification contribution to number counts is itself another potentially important probe of gravity and dark matter [78–84], independent of weak lensing surveys. In order to realise the potential of these probes, it is necessary to include careful modelling of s and b_e.

1.5.4 Potential terms

Finally, the $\Delta^{\rm Pot}$ term in (1.46) collects the remaining, sub-dominant relativistic potential effects:

$$\Delta^{\rm Pot}(z,\boldsymbol{n}) = [A_{\rm L}(z,F_c) - A_{\rm D}(z,F_c)]\Phi(z,\boldsymbol{n}) + \frac{\partial\Phi(z,\boldsymbol{n})}{\partial\ln(1+z)} + \Big[3 - b_{\rm e}(z,F_c)\Big]\mathcal{H}V$$
$$- 2A_{\rm L}(z,F_c)\int_0^{\chi(z)}\frac{{\rm d}\tilde{\chi}}{\chi(z)}\,\Phi(\tilde{\chi},\boldsymbol{n}) - 2A_{\rm D}(z,F_c)\int_0^{\chi(z)}{\rm d}\tilde{\chi}\,\frac{\partial\Phi(\tilde{\chi},\boldsymbol{n})}{\partial\eta}, \tag{1.52}$$

The first two terms on the right of (1.52) are Sachs-Wolfe terms. The third term is the Newtonian gauge correction that is needed for the physical definition of clustering bias, where V is the velocity potential. In line 2 of (1.52), the first term is Shapiro time delay and the second is integrated Sachs-Wolfe. The potential term scales in Fourier space as $\Delta^{\rm Pot} \sim \Phi \sim \delta_{\rm m}\, H_0^2/k^2$, which is only non-negligible on even larger scales than the Doppler term.

In auto-correlations of a single tracer the leading Doppler contribution scales as ${\rm Doppler}^2 \sim (\delta_{\rm m})^2\, H_0^2/k^2$, like the leading potential contribution, $\delta_{\rm m} \times \Phi$. But in cross-correlations between tracers, the leading Doppler contribution is $\delta_{\rm m} \times$ Doppler [67, 75], which scales as $(\delta_{\rm m})^2\, H_0/k$ and dominates over the potential contribution. The ultra-large scale relativistic effects are partially degenerate with the contribution of scale-dependent clustering bias from $f_{\rm NL}$ [41–43, 85–88].

However, lensing and other relativistic effects are not simply a theoretical 'nuisance' that needs to be included in the modelling – they can also be important cosmological probes of gravity (see e.g. [89–98])

Chapter 2

Correlation functions, multi-tracers and Fisher forecasts

The following chapter gives a brief overview of how to analyse the matter distribution in the Universe and estimate the precision on cosmological parameters from future experiments.

The structure of the chapter is as follows: The matter density contrast in cosmological surveys are traditionally investigated via the two-point correlation function. These correlations are then analysed in either Fourier or harmonic space, which is recapped in section 2.1. Information from distinctly different dark matter tracers can be combined through cross-correlations using the multi-tracer technique, explained in section 2.2. Lastly, we review how to forecast the precision on parameters from future surveys using a Fisher Matrix analysis in section 2.3, as well as how we calculate the expected bias on these parameters from theoretical systematics, i.e. assuming an incorrect cosmological model.

2.1 Two-point correlation function

The main features of the galaxy distribution are described by the two-point correlation function (2PCF):

$$\xi_{\rm g}(\boldsymbol{r}) = \langle \Delta_{\rm g}(\boldsymbol{x})\, \Delta_{\rm g}(\boldsymbol{x'}) \rangle \,, \tag{2.1}$$

where $\boldsymbol{x'} = \boldsymbol{x} + \boldsymbol{r}$ refers to a point separated by $\boldsymbol{r}$ from the reference position $\boldsymbol{x}$. Statistical homogeneity implies $\xi_{\rm g}$ is independent of $\boldsymbol{x}$, and in the absence of redshift-space effects, isotropy depends only on the magnitude of separation $r = |\boldsymbol{r}|$. The 2PCF

describes the excess probability of finding two galaxies separated by this distance, and in a truly random distribution of galaxies $\xi_{\rm g} = 0$ for any r.

2.1.1 Fourier power spectrum

It is often convenient to perform the analysis in the Fourier domain, since the transform decomposes space-dependent functions into functions depending on spatial frequency. The convention for the Fourier and inverse Fourier transform used in the thesis is

$$\Delta_{\rm g}(\boldsymbol{k}) = \int d\boldsymbol{x}\, \Delta_{\rm g}(\boldsymbol{x}) e^{-i\boldsymbol{k}\cdot\boldsymbol{x}} \quad \text{and} \quad \Delta_{\rm g}(\boldsymbol{x}) = \int \frac{d\boldsymbol{k}}{(2\pi)^3}\, \Delta_{\rm g}(\boldsymbol{k}) e^{i\boldsymbol{k}\cdot\boldsymbol{x}}\,. \tag{2.2}$$

Under an assumption of statistical isotropy, the Fourier transform of the 2PCF defines the observed Fourier power spectrum as

$$P_{\rm g}(\boldsymbol{k'}) = \int d\boldsymbol{r}\, \xi_{\rm g}(r) e^{i\boldsymbol{k'}\cdot\boldsymbol{r}} \quad \text{or} \quad (2\pi)^3 \delta^D(\boldsymbol{k'} - \boldsymbol{k}) P_{\rm g}(k') = \langle \Delta_{\rm g}(\boldsymbol{k}) \Delta^*_{\rm g}(\boldsymbol{k'}) \rangle\,. \tag{2.3}$$

The Fourier power spectrum requires a choice of fiducial model to convert observed angles and redshifts to distances. This then requires an Alcock-Paczynski correction [99] to compensate for the error in the choice of fiducial. By assuming an incorrect fiducial model, the true comoving volume $\bar{\mathcal{V}}_{\rm c}$ will be distorted by a factor

$$\mathcal{V}_{\rm c}(z) = \frac{D_A^2(z)\, \bar{H}(z)}{\bar{D}_A^2(z)\, H(z)}\, \bar{\mathcal{V}}_{\rm c}\,. \tag{2.4}$$

$P_{\rm g}(\boldsymbol{k'})$ encodes a flat-sky approximation that neglects wide-angle correlations and doesn't include cross-bin correlations. In addition, it does not take into account the lensing effect expected in GR. There are prescriptions to deal with these issues (e.g. [100]). However, it is useful to explore an alternative analysis that avoids these problems from the start.

2.1.2 Angular power spectrum

The alternative to the 3D power spectrum is to use the angular power spectrum $C_\ell(z, z')$, which is the harmonic transform of the correlation function that is observed in redshift space — i.e., on the backward light-cone of the observer [40, 41, 101–103]. The C_ℓ has the advantage that it is an observable, hence we can ignore the uncertainty in the fiducial model and avoid the AP correction. In addition, it also naturally incorporates Doppler and lensing magnification effects on the auto- and cross-bin correlations, as

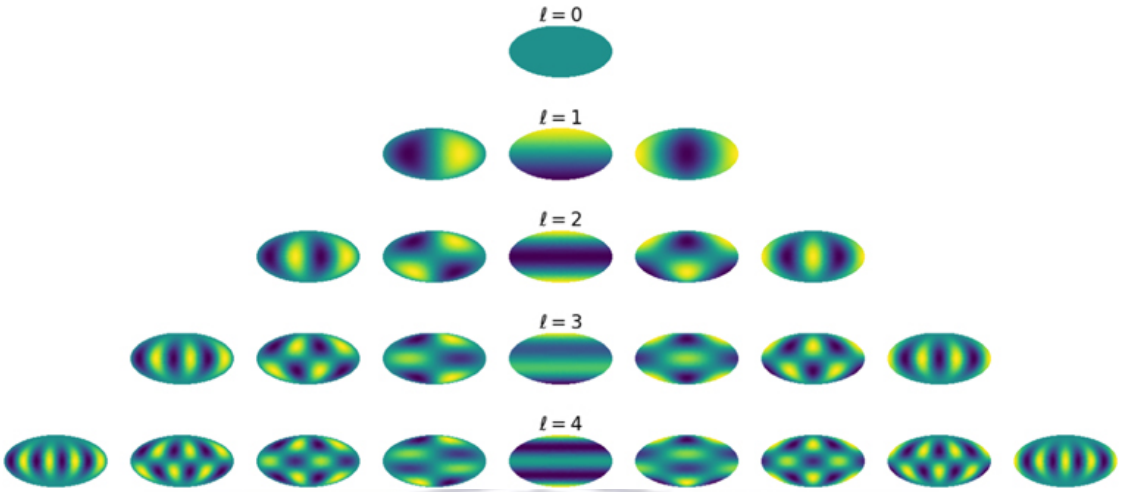

Fig. 2.1 A spherical harmonic decomposition of data into multipoles ℓ. The horizontal axis indicates the different possible configurations of m, ranging between $-\ell < m < \ell$. Credit [104].

well as other smaller relativistic observational effects. The number density contrast observed on the backward light-cone can be given directly in terms of the fundamental observables z and $\boldsymbol{n}$ by expanding in spherical harmonics:

$$\Delta_{\rm g}(z, \boldsymbol{n}) = \sum_{\ell m} a_{\ell m}(z) Y_{\ell m}(\boldsymbol{n}) \tag{2.5}$$

where the multipole ℓ corresponds to the angular size considered. As illustrated in Figure 2.1, this decomposition includes wide-angle effects as well.

The spherical harmonic coefficients $a_{\ell m}$ are expressed in terms of the spherical Bessel function $j_\ell(k\chi)$:

$$a_{\ell m}(z) = \frac{(i)^\ell}{2\pi^2} \int d\boldsymbol{k}\ \Delta_{\rm g}(z, \boldsymbol{k})\ j_\ell(k\chi) Y^*_{\ell m}(\boldsymbol{n})\,. \tag{2.6}$$

We assume that the $a_{\ell m}$ are Gaussian distributed with covariance

$$\langle a_{\ell m}(z_i)\ a^*_{\ell' m'}(z_j)\rangle = C_\ell(z_i, z_j)\ \delta_{\ell\ell'}\delta_{mm'}\,. \tag{2.7}$$

Following the notation and approach of [40] we relate the $a_{\ell m}$ coefficients to the power spectrum of the primordial curvature perturbations $\mathcal{P}(k)$:

$$C_\ell(z_i, z_j) = 4\pi \int {\rm d}\ln k\, \Delta^W_\ell(z_i, k) \Delta^W_\ell(z_j, k)\, \mathcal{P}(k). \tag{2.8}$$

The dimensionless primordial curvature power spectrum $\mathcal{P}(k) = A_s(k/k_0)^{n_s-1}$ generates the initial over- and under-densities from which present day large scale structures grew. It is expressed in terms of the amplitude A_s, the spectral index n_s and pivot scale $k_0 = 0.05\,\mathrm{Mpc}^{-1}$. The Δ_ℓ^W in (2.8) represents the windowed transfer functions that relate Δ_g to $\mathcal{P}$. We refer to it as the "windowed" transfer function since it describes the observable transfer function in each z-bin located at z_i via the window function W [1]:

$$\Delta_\ell^W(z_i,k) = \int \mathrm{d}z\, p(z)\, W(z_i,z)\, \Delta_\ell(z,k)\,, \tag{2.9}$$

where p is a selection function which in practice is the redshift distribution function of the observed sources: $p \propto N_\mathrm{g} = \mathrm{d}\mathbb{N}_\mathrm{g}/(\mathrm{d}z\mathrm{d}\Omega_{\boldsymbol{n}})$. Hence, p and W work as a weighting function for Δ_ℓ. The product of the selection function and the window function inside the bin is normalised such that $\int \mathrm{d}z\, p(z) W(z_i,z) = 1$ for all z_i.

In (2.9) the Δ_ℓ represents the theoretical transfer function (1.46) in harmonic space

$$\Delta_\ell(k) = \delta_\mathrm{g}\, j_\ell(k\chi) + \Delta_\ell^\mathrm{RSD} + \Delta_\ell^\mathrm{Dopp} + \Delta_\ell^\mathrm{Lens} + \Delta_\ell^\mathrm{Pot}\,. \tag{2.10}$$

The first term represents the matter density contrast with the scale dependent clustering bias (1.38), whereas the last term of (2.10) is simply the sum of the potential contributions, i.e. the Sachs-Wolfe, integrated Sachs-Wolfe and Shapiro time delay: $\Delta_\ell^\mathrm{Pot} = \Delta_\ell^\mathrm{SW} + \Delta_\ell^\mathrm{ISW} + \Delta_\ell^\mathrm{TD}$. The terms are written explicitly as [93, 94, 102, 105]:

$$\Delta_\ell^\mathrm{RSD} = \frac{k v_k}{\mathcal{H}}\, j_\ell''(k\chi)\,,$$

$$\Delta_\ell^\mathrm{Dopp} = \left(\frac{2-5s}{\mathcal{H}\chi} + 5s - b_e + \frac{\mathcal{H}'}{\mathcal{H}^2}\right) v_k j_\ell'(k\chi)\,,$$

$$\Delta_\ell^\mathrm{Lens} = \frac{\ell(\ell+1)(2-5s)}{2} \int_0^\chi \mathrm{d}\tilde{\chi} \frac{(\chi-\tilde{\chi})}{\chi\tilde{\chi}} \Big[\Phi_k(\tilde{\chi}) + \Psi_k(\tilde{\chi})\Big] j_\ell(k\tilde{\chi})\,,$$

$$\Delta_\ell^\mathrm{SW} = \left[(b_e-3)\frac{\mathcal{H}}{k} v_k + \left(1 + \frac{2-5s}{\mathcal{H}\chi} + 5s - b_e + \frac{\mathcal{H}'}{\mathcal{H}^2}\right)\Psi_k + [5s-2]\,\Phi_k + \frac{\Phi_k'}{\mathcal{H}}\right] j_\ell(k\chi)\,,$$

$$\Delta_\ell^\mathrm{ISW} = \left(\frac{2-5s}{\mathcal{H}\chi} + 5s - b_e + \frac{\mathcal{H}'}{\mathcal{H}^2}\right) \int_0^\chi \mathrm{d}\tilde{\chi} \Big[\Phi_k'(\tilde{\chi}) + \Psi_k'(\tilde{\chi})\Big] j_\ell(k\tilde{\chi})\,,$$

$$\Delta_\ell^\mathrm{TD} = \frac{(2-5s)}{\chi} \int_0^\chi \mathrm{d}\tilde{\chi} \Big[\Phi_k(\tilde{\chi}) + \Psi_k(\tilde{\chi})\Big] j_\ell(k\tilde{\chi})\,.$$

In order to simplify the notation we suppress the redshift and k dependence, except in the spherical Bessel function. The peculiar velocity field in k-space is denoted by $v_k = |\boldsymbol{v}|_k$. In our model there is no matter anisotropic stress, and therefore $\Phi_k = \Psi_k$.

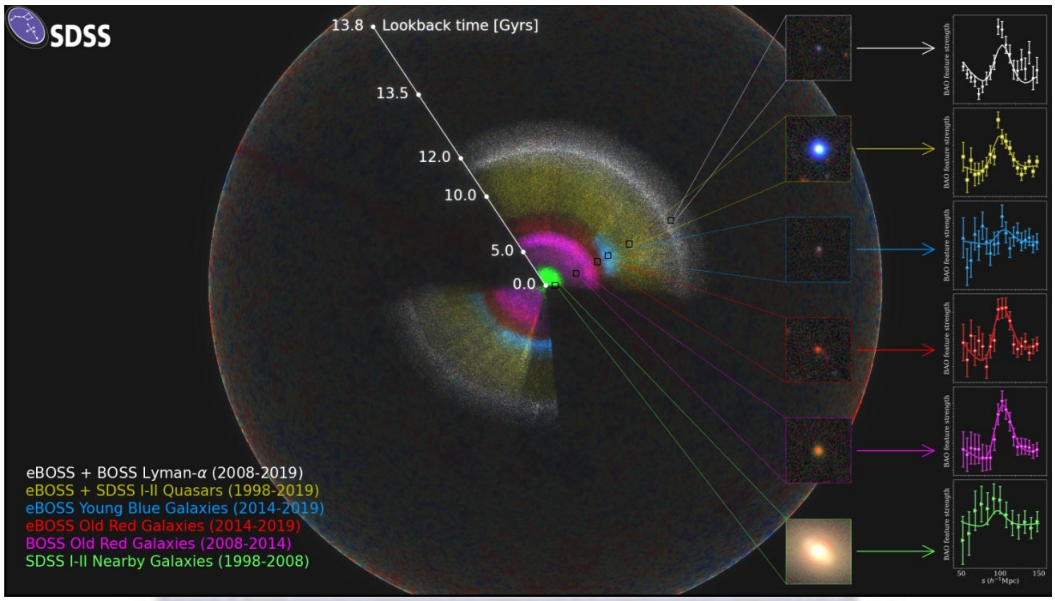

Fig. 2.2 A diagram of several different tracers observed by SDSS. Credit: eBOSS collaboration.

Note that the split in (2.10) changes if a different gauge is chosen - but the sum of all terms, Δ_ℓ, is gauge invariant.

An immediate issue with the angular power spectrum is that, unlike $P(\boldsymbol{k}, z)$, we cannot cleanly separate out the RSD effect. In addition, computational complexity arises from the oscillating spherical Bessel functions in $C_\ell(z_i, z_j)$, from cross-bin correlations when $z_i \neq z_j$. Also, to maximally exploit the potential of spectroscopic surveys we need to utilise very thin redshift bins, which could potentially introduce non-linear effects into large scale modes (see subsection 2.3.1). Nevertheless, advances in using the angular power spectrum to analyse galaxy survey data are ongoing (e.g. [17, 106–113]).

2.2 Multi-tracer technique

In the future there will be many surveys that cover large fractions of the sky with high completeness, therefore the variance due to the surveys finite volume (i.e. cosmic variance) is perhaps the most formidable obstacle to better extract information on cosmological parameters [114]. A natural extension to analysing cosmological experiments independently, is to combine different surveys and take advantage of the cross-correlations between tracers to improve the statistical power - called the multi-tracer (MT) technique. Using two distinctly different dark matter tracers that sample the same underlying density field (see Figure 2.2) enables us to significantly

reduce the effect of experimental systematics and cosmic variance [26, 27]. The authors have pointed out that for certain parameters the effect of cosmic variance can be circumvented, as is the case for: clustering bias, linear matter growth rate and primordial non-Gaussianity. The reason for this is that the bias-sensitive parameters are not subject to the same stochastic processes that lead to different realisations of the density field for some matter power spectrum. By comparing the clustering of different types of tracers that sample the same underlying matter distribution, we should be able to measure such parameters without cosmic variance. Therefore the precision will be limited only by the shot-noise of the experiment, or by the instrumental noise in the case of intensity mapping. The MT was applied using the angular power spectra in [91, 92], to constrain local-type primordial non-Gaussianity. The suppression of cosmic variance lead to significant improvements over single-tracer constraints. As a consequence, a smaller overlap volume still produces better results than a simple combination of the full larger volume of each individual tracer.

Let's consider multiple tracers $A = 1, 2, \cdots$, and define the generic angular power spectrum:

$$\left\langle \Delta_A(z_i, \boldsymbol{n}_i)\, \Delta_B(z_j, \boldsymbol{n}_j) \right\rangle = \sum_\ell \frac{(2\ell+1)}{4\pi} C_\ell^{AB}(z_i, z_j)\, \mathcal{L}_\ell\Big(\boldsymbol{n}_i \cdot \boldsymbol{n}_j\Big)\,, \tag{2.11}$$

where Δ_A corresponds to $\Delta_{\rm g}$ of tracer A and $\mathcal{L}_\ell$ denotes the Legendre polynomial. Therefore we can compute the multi-tracer by generalising from (2.8), such that

$$C_\ell^{AB}(z_i, z_j) = 4\pi \int \mathrm{d}\ln k\, \Delta_{A\ell}(z_i, k)\, \Delta_{B\ell}(z_j, k)\, \mathcal{P}(k)\,. \tag{2.12}$$

Note that $\Delta_{A\ell}$ is also the windowed transfer function, but for simplified notation we drop the superscript W. The multi-tracer is a matrix that contains both auto- and cross-power spectra. The former refers to correlations between the observed density contrast in the same survey ($A = B$), whereas the latter refers to the correlations between surveys ($A \neq B$). Explicitly, for N number of tracers the MT looks like

$$\boldsymbol{C}_\ell = \begin{bmatrix} C_\ell^{11}(z_i, z_j) & C_\ell^{12}(z_i, z_j) & \cdots & C_\ell^{1N}(z_i, z_j) \\ \cdots & \cdots & \cdots & \cdots \\ C_\ell^{N1}(z_i, z_j) & C_\ell^{N2}(z_i, z_j) & \cdots & C_\ell^{NN}(z_i, z_j) \end{bmatrix}, \tag{2.13}$$

where each entry in (2.13) is a matrix of all the auto- and cross-bin correlations in the power spectrum $C_\ell(z_i, z_j)$.

2.3 Fisher Matrix analysis

In order to estimate the precision expected from a future measurement (or experiment), we assume that the given observable is based on a theoretical model, which corresponds to a function dependent on a set of known parameters. We can forecast the precision on these parameters by turning to a Bayesian statistical method called the Fisher Matrix analysis. This method is used to quantify the amount of information that an observable random variable X carries about an unknown parameter value ϑ_α. Let $\mathcal{L}$ be the log-likelihood function and $\boldsymbol{\vartheta}$ the parameter vector under consideration. The Fisher matrix is simply evaluated at the parameter maximum-liklihood of the best-fit values $\bar{\boldsymbol{\vartheta}}$, namely

$$\boldsymbol{F}(\vartheta_\alpha, \vartheta_\beta) = \frac{\partial^2 \mathcal{L}}{\partial \vartheta_\alpha \vartheta_\beta}\bigg|_{\boldsymbol{\vartheta}=\bar{\boldsymbol{\vartheta}}} . \tag{2.14}$$

The multi-tracer Fisher matrix for angular power spectra is defined as follows [2, 91, 92]:

$$F_{\vartheta_\alpha \vartheta_\beta} = \sum_{\ell_{\min}}^{\ell_{\max}} \frac{(2\ell+1)}{2} f_{\rm sky} \, \mathrm{Tr}\Big[\Big(\partial_{\vartheta_\alpha} \boldsymbol{C}_\ell\Big) \boldsymbol{\Gamma}_\ell^{-1} \Big(\partial_{\vartheta_\beta} \boldsymbol{C}_\ell\Big) \boldsymbol{\Gamma}_\ell^{-1}\Big] , \tag{2.15}$$

where ϑ_α represents the parameters considered in the analysis. Furthermore,

$$\boldsymbol{\Gamma}_\ell = \boldsymbol{C}_\ell + \mathcal{N}_\ell , \tag{2.16}$$

where $\mathcal{N}_\ell$ is the expected noise of the surveys under consideration.

The Fisher matrix $\boldsymbol{F}$ is the inverse of the covariance of the parameters, therefore the conditional and marginal errors of the parameters are given by

$$\sigma^2(\vartheta_\alpha) = [F_{\vartheta_\alpha \vartheta_\alpha}]^{-1} \quad \text{and} \quad \sigma^2(\vartheta_\alpha) = \Big[\boldsymbol{F}^{-1}\Big]_{\vartheta_\alpha \vartheta_\alpha} , \tag{2.17}$$

respectively. The marginal error includes the uncertainty of all the parameters under consideration in the estimate, whereas the conditional error assumes all other parameters are known.

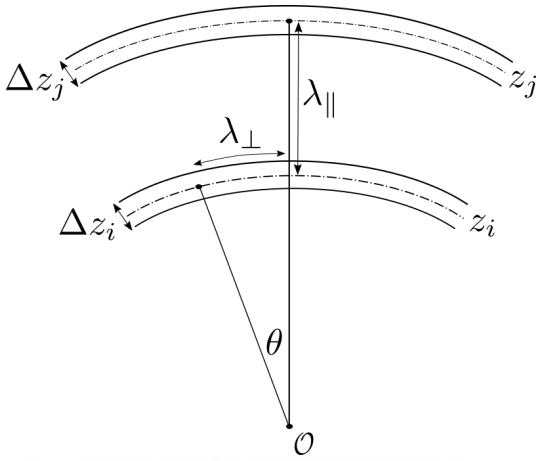

Fig. 2.3 Scales associated with a multipole ℓ.

2.3.1 Scales included

The largest scales that we can include in the Fisher Matrix analysis is dependent on the size of the sky area $\Omega_{\rm sky}$ of the survey under consideration, where $\Omega_{\rm sky} = 4\pi\, f_{\rm sky}$. We can compute the largest observable scale in harmonic space using $\ell_{\rm min} = {\rm int}(\pi/\sqrt{\Omega_{\rm sky}}) + 1$, and introduce it into the computation via the lower limit of the summation in (2.15). For the MT, we consider only the overlapping sky area of the surveys in the Fisher Matrix analysis.

In reality, we cannot perfectly extract all the observable scales from the data – there will be a loss of ultra-large-scale modes due to systematics, e.g. extinction due to Galactic dust or stellar contamination in galaxy surveys, or foreground contamination of intensity mapping. The cosmological signal from 21cm emission is several orders of magnitude lower than the galactic and extra-galactic foreground contamination. In order to extract the cosmological information, it is therefore necessary to first remove or model the systematics in galaxy and intensity mapping surveys. In order to take account of the loss of some ultra-large scale signal due to systematics, we need to impose a minimum angular multipole $\ell_{\rm min}$. For a multi-tracer analysis, the same $\ell_{\rm min}$ is used for each survey. In the case of very large sky area, $\ell_{\rm min} \sim 5$ may be feasible for intensity mapping [115], and we take this as our 'optimistic' minimum.

We only consider linear perturbations in our Fisher forecasts. The inclusion of nonlinear effects is beyond the scope of this thesis and we therefore need to choose $\ell_{\rm max}$ in (2.15) to exclude these effects from the Fisher matrix.

In Fourier space, the scale marking the breakdown of a perturbative analysis of matter clustering is given in [116] as

$$k_{\rm nl}(z) = k_{\rm nl,0}(1+z)^{2/(2+n_s)} \quad \text{with} \quad k_{\rm nl,0} \simeq 0.2h\,{\rm Mpc}^{-1}\,. \tag{2.18}$$

On the scales of interest, the multipole ℓ corresponds to a transverse comoving length scale $\lambda_\perp = 2\pi/k$, which subtends an angle $\theta = \lambda_\perp/\chi$ at the observer (see Figure 2.3). Using $\theta = 2\pi/\ell$, this gives $\ell = \chi k$. It follows that the maximum multipole for auto-correlations is

$$\ell_{\rm max}(z_i, z_i) = \chi(z_i) k_{\rm nl}(z_i)\,. \tag{2.19}$$

The case of cross-bin correlations is more complicated (see the discussion in [102]). In principle, one can allow for $\ell \gg 1$ in the case of near-radial correlations, for which $\theta \ll 1$ and $\lambda_\perp \ll 2\pi/k_{\rm nl}$ – provided that $\lambda_\parallel > 2\pi/k_{\rm nl}$, to ensure that $\lambda > 2\pi/k_{\rm nl}$. However, in order to fully exclude nonlinearities from the Fisher matrix, we need to exclude them also from the covariance of $C_\ell(z_i, z_j)$, which contains the term $C_\ell(z_i, z_i)C_\ell(z_j, z_j)$. If $\lambda_\perp$ is nonlinear then $C_\ell(z_i, z_i)$ includes nonlinear effects, and hence the covariance contains nonlinearities. Therefore we impose the cut

$$\ell_{\rm max}(z_i, z_j) = \min\Big\{\ell_{\rm max}(z_i, z_i), \ell_{\rm max}(z_j, z_j)\Big\}\,. \tag{2.20}$$

Note that our modelling of the linear cut is simplistic and optimistic. An improved model has recently been presented in [117], which recognises the subtle relationship between scales in Fourier and harmonic space, but which does not include redshift space effects. Stage IV surveys probably require a more robust scale cut, which can be made using the BNT method [118]. Advances in analysis of this relationship in redshift space are presented in [119] and references cited therein. In their work they have found that by decreasing the redshift bin-width below $\Delta z \lesssim 0.01$, non-linear effects are introduced into the large scale modes. The uncontrolled nonlinearities can lead to a biased growth rate estimate. We use $\Delta z \geq 0.01$, while recognising that further work is needed to improve the removal of non-linear contamination.

2.3.2 Best-fit bias

The best-fit values will be influenced by unaccounted systematics or incomplete theoretical modelling. In order to estimate this bias one can use the 'correct' mock data and do inference on this data using the 'wrong' model, as done in [120]. This approach provides a precise evaluation of the biasing introduced, however it is a time-consuming

and computationally expensive process. We rather follow the alternative approach, which uses the Fisher information in the case of nested model selection [121].

In the Fisher formalism we assume that the posterior distribution of a set of m parameters $\boldsymbol{\vartheta}$, given some n dimensional data vector $\boldsymbol{X}$, is Gaussian:

$$\mathcal{P}(\boldsymbol{\vartheta}|\boldsymbol{X}) = \left[(2\pi)^m \det\left(\boldsymbol{F}^{-1}\right)\right]^{-1/2} \exp\left[-\frac{1}{2}(\boldsymbol{\vartheta}-\bar{\boldsymbol{\vartheta}})^T \boldsymbol{F}\,(\boldsymbol{\vartheta}-\bar{\boldsymbol{\vartheta}})\right] . \tag{2.21}$$

The best-fit values $\bar{\boldsymbol{\vartheta}}$ maximise the posterior. Using Bayes theorem, we relate the posterior with the likelihood of the data $\mathcal{L}$ via

$$\mathcal{P}(\boldsymbol{\vartheta}|\boldsymbol{X}) \propto \mathcal{L}(\boldsymbol{X}|\boldsymbol{\vartheta})\,\Pi(\boldsymbol{\vartheta})\,, \tag{2.22}$$

where Π is the prior. For simplicity we do not consider any priors on the parameters. Assuming the likelihood to be Gaussian,

$$\mathcal{L}(\boldsymbol{X}|\boldsymbol{\vartheta}) = [(2\pi)^n \det \boldsymbol{\Gamma}]^{-1/2} \exp\left[-\frac{1}{2}(\boldsymbol{X}-\bar{\boldsymbol{X}})^T\boldsymbol{\Gamma}^{-1}(\boldsymbol{X}-\bar{\boldsymbol{X}})\right] , \tag{2.23}$$

where $\boldsymbol{\Gamma}$ is the covariance of the data and $\bar{\boldsymbol{X}}$ is the value that maximises the likelihood.

Making incorrect model assumptions will therefore lead to a shift in the best-fit value of the parameters considered. In the example of nested models, there is a sub-model with parameters ψ_i, so that $\vartheta_\alpha = \{\psi_i, \varphi_I\}$. Suppose that we make an incorrect assumption, and fix the values of φ_I to incorrect values $\hat{\varphi}_I$, instead of the true values $\bar{\varphi}_I$. This shifts φ_I by the amount

$$\delta\varphi_I = \hat{\varphi}_I - \bar{\varphi}_I\,. \tag{2.24}$$

As a consequence, we will estimate the remaining parameter values to be $\hat{\psi}_i$, instead of their true values $\bar{\psi}_i$. The bias on the best-fit values is:

$$\delta\psi_i = \hat{\psi}_i - \bar{\psi}_i\,. \tag{2.25}$$

We relate (2.25) to (2.24) through the covariance of the parameters, determined by the amount of information we expect to extract from the survey [122, 123]:

$$\delta\psi_i = -\sum_{I,j} \delta\varphi_I\, F_{\varphi_I\psi_j} \left[\boldsymbol{H}^{-1}\right]_{\psi_j\psi_i} , \tag{2.26}$$

where $\boldsymbol{F}$ is the Fisher matrix of the total set ϑ_α, and $\boldsymbol{H}$ is the Fisher matrix of the sub-model with the parameters ψ_i that we wish to fit.

Chapter 3

Next-generation cosmological surveys

In this work we forecast the constraints on cosmological parameters expected from future spectroscopic surveys. To accomplish this we are required to model the observed matter distribution, based on the survey specifications and instrumental sensitivity.

Measurements of galaxy clustering in upcoming surveys will not only be sensitive to the standard redshift-space distortions, but the observed galaxy number counts will also be distorted by lensing magnification and Doppler effects. The amplitude of these contributions depends sensitively on magnification bias and evolution bias in the galaxy number density. Magnification bias quantifies the change in the observed number of galaxies gained or lost by lensing magnification, while evolution bias quantifies the physical change in the galaxy number density relative to the conserved case.

In our forecasts we consider several different dark matter tracers that are observed over a large redshift range, namely: neutral Hydrogen observed by the Square Kilometre Array Observatory (SKAO); in the optical band we model the Dark Energy Spectroscopic Instrument (DESI)-like bright galaxy survey (BGS); as well as the Euclid-like Hα surveys in near-infrared (NIR). The following chapter serves as an overview of the more technical aspects of simulating such surveys, and is largely based on [3] - of which I am co-author.

This chapter is structured as follows. We give a brief review of the luminosity function and how it is used to calculate the comoving number density in section 3.2. We then carefully define and explain how the astrophysical parameters of magnification bias and evolution bias are computed in section 3.3, explicitly highlighting subtleties in their definition. The details on the luminosity functions and corresponding astrophysical

parameters of the near-infrared and optical galaxy surveys are given in section 3.4. Similarly, we explain such details on the neutral Hydrogen surveys in section 3.5. The noise specifications for the surveys under consideration (and their combinations) are explained in section 3.6. Finally, we summarise the survey specifications, noise properties and fitting functions used in our simulations in section 3.7.

3.1 Preamble

The result of an experiment is not only dependent on the instrumental specifications (for example the physical dimensions and sensitivity of the detector), but also on the survey specifications like sky area and redshift range observed. An increased cosmological volume will contain a greater number of sources, improve the statistical capability of the survey and render higher precision measurements. Furthermore, we also have to take into account relativistic effects that alter the observed galaxy number counts via redshift space distortions, lensing magnification and other light-cone effects. The last point proves to be the most challenging and therefore we carefully address this issue in the following sections.

In section 3.2 we show how to compute the comoving number density (1.44) using the luminosity function, which is unique to each survey. There are important astrophysical parameters that are dependent on the comoving number density and hence the luminosity function. The magnification bias is defined as the rate at which the comoving number density changes with respect to the luminosity threshold, and is related to the sensitivity of the detector. The evolution bias compensates for how the number density evolves over time, which is tracer dependent. In section 1.5 we explicitly state the contribution of each light-cone effect to the observed density contrast (1.45). The amplitude of the Doppler effect (subsection 1.5.2), lensing magnification (subsection 1.5.3) and potential terms (subsection 1.5.4) are highly sensitive to the magnification bias s and evolution bias $b_{\rm e}$. In addition, the lensing and Doppler contributions are powerful and independent tests of gravity. Therefore, in order to properly model the density contrast and take advantage of these tests, we need to accurately model s and $b_{\rm e}$ contributions. We estimate that errors on s and b_e need to be $\lesssim 10\%$ in order to preserve detectability of the lensing and Doppler effects [91].

We clarify some subtleties involved in the meaning and calculation of the magnification and evolution biases, and to derive these important astrophysical parameters for a broad variety of different future galaxy surveys. These biases are given by derivatives of the number density, and consequently are very sensitive to the form of the luminosity

function. We give a careful derivation of the magnification and evolution biases in section 3.3, clarifying a number of results in the literature.

We then relate the general theory of s and b_e to specific luminosity functions for Hα-like surveys like Euclid in subsection 3.4.1 – illustrating how different survey sensitivities affect the luminosity curves and corresponding astrophysical parameters. We expand the analysis to surveys with K-correction, like Dark Energy Spectroscopic Instrument (DESI)-like bright galaxy survey (see subsection 3.4.2). Finally in section 3.5 we consider both the galaxy and intensity mapping surveys of SKAO 21cm neutral Hydrogen (HI). The intensity mapping surveys do not resolve individual galaxies, rather they infer the matter distribution from temperature fluctuations by measuring the integrated line emissions. Therefore, the intensity mapping surveys are not dependent on the detector sensitivity, which means that the evolution bias is only dependent on the background brightness temperature, i.e. survey independent. The magnification bias is a constant, since surface brightness is conserved.

Instead of computing the luminosity functions, comoving number densities and resulting astrophysical parameters, we simplify the process by determining fitting functions for: the number density (comoving and observed), as well as the magnification and evolution biases for all the surveys considered.

Following this, we model the uncertainties in the measurement of the various surveys by determining their specific noise properties in section 3.6. The main uncertainty in galaxy surveys are as a result of the discrete nature of the galaxy number count approach, and therefore is dominated by shot-noise. Conversely, the intensity mapping surveys observe integrated emission and hence are more affected by instrumental noise. We also model noise for the combination of surveys, which is necessary when computing the multi-tracer correlation of different surveys, and we show in subsection 3.6.3 that the cross-shot noise in our survey configurations may be neglected.

The results of the chapter is summarised in section 3.7 for the convenience of the reader.

3.2 Luminosity function

Cosmological experiments traditionally analyse the observed number density contrast (1.45) via galaxy number count surveys. The amount of galaxies an experiment is able to observe depends on the sensitivity of the detector, i.e. the flux cut F_c of the survey (which is constant). The faintest galaxies detectable by the instrument is dependent on the brightness of the galaxy and the distance to the source. Therefore,

the corresponding luminosity cut L_c is related to the flux cut through the luminosity distance (1.17). Written in terms of co-moving distance:

$$L_c(z) = 4\pi\, F_c(1+z)^2\chi^2(z). \tag{3.1}$$

In this chapter we will only work with the background quantities so the over-bars are omitted. The number of galaxies $\mathbb{N}_{\rm g}$ that are observed above the flux cut is the same as the number at the source that are above the corresponding luminosity threshold:

$$\mathrm{d}\mathbb{N}_{\rm g} = N_{\rm g}(z, F_{\rm c})\,\mathrm{d}z\,\mathrm{d}\Omega_{\boldsymbol{n}} = n_{\rm g}(a, L_{\rm c})\,\mathrm{d}\mathcal{V}\,, \tag{3.2}$$

where $n_{\rm g}$ is the comoving number density and $\mathrm{d}\mathcal{V}$ is the comoving volume element. The above equation explicitly states the dependence of (1.44) on the sensitivity of the survey and corresponding luminosity threshold. The number density measured at the observer $N_{\rm g}$ are related to the comoving number density at the source $n_{\rm g}$ by

$$N_{\rm g} = \frac{\chi^2}{H} n_{\rm g}\,. \tag{3.3}$$

The survey will detect all the galaxies that are brighter than the luminosity threshold, and so we compute $n_{\rm g}$ by integrating the (comoving) luminosity function Φ over luminosity:

$$n_{\rm g}(a, L_{\rm c}) = \int_{L_{\rm c}(a)}^{\infty} \mathrm{d}L\, \frac{\Phi(a, L)}{L_*(a)}\,, \tag{3.4}$$

where L_* is a characteristic luminosity in the luminosity function. We can express the luminosity function analytically in the simple form:

$$\Phi(z, y) = \phi_*(z)\, g(y) \quad \text{and} \quad y \equiv \frac{L}{L_*}\,, \tag{3.5}$$

where $\phi_*(z)$ is a characteristic number density. Note than an alternative definition of the luminosity function is also used:

$$n_{\rm g}(a, L_{\rm c}) = \int_{L_{\rm c}(a)}^{\infty} \mathrm{d}\ln L\; \hat{\Phi}(a, L) \quad \text{where} \quad \hat{\Phi} = \frac{L}{L_*}\,\Phi\,. \tag{3.6}$$

In the case of galaxy surveys, accurate knowledge of the luminosity function is needed, since small changes in the luminosity function can lead to large changes in its partial derivatives at fixed redshift and fixed luminosity cut. For example, a Schechter type function and a broken power-law model have both been considered as models for

a Stage IV Hα spectroscopic survey. While both give very similar number densities, they produce significantly different evolution biases.

3.3 Magnification and evolution bias

Observations of galaxy number counts trace not only the underlying matter density, but are distorted by effects of observing them on our past lightcone. The dominant part of this is the linear redshift-space distortions (RSD). There is also an effect on number counts from lensing magnification – and other relativistic effects become potentially important on ultra-large scales. These are the same scales where local primordial non-Gaussianity are strongest, and could possibly influence the measurement on $f_{\rm NL}$.

There are three important astrophysical parameters in $\Delta_{\rm g}$ (1.45): the clustering bias b relating number and matter density contrasts ($\delta_{\rm g} = b\,\Delta_{\rm m}$); the evolution bias $b_{\rm e}$ and the magnification bias s. Here we focus on the last two. Note that the magnification bias has two different but equivalent forms, denoted by $s = 2\mathcal{Q}/5$. The relation between the notations are expressed later in (3.12).

The magnification bias and evolution bias are astrophysical parameters that depend on the intrinsic galaxy properties at the source, and on the survey-dependent flux cut. They are defined by *partial* derivatives that respectively hold a fixed and hold $L_{\rm c}$ fixed [40, 43]:

$$\mathcal{Q}(a, L_{\rm c}) = -\frac{\partial \ln n_{\rm g}(a, L_{\rm c})}{\partial \ln L_{\rm c}}\,, \tag{3.7}$$

$$b_{\rm e}(a, L_{\rm c}) = \frac{\partial \ln n_{\rm g}(a, L_{\rm c})}{\partial \ln a}\,. \tag{3.8}$$

In general, these parameters are very sensitive to the galaxy sample and the type of survey, thus modelling them accurately is important when taking into account the lensing magnification and Doppler contributions. Light beams from sources reach the observer via the intervening large-scale structure: $\mathcal{Q}$ determines the number of galaxies gained at the observer due to magnification ($\kappa > 0$), or lost due to de-magnification ($\kappa < 0$). Magnification bias is positive, except in the idealised case of all possible galaxies are detected, $\mathcal{Q} = 0$. The background comoving number density evolves according to the properties of the haloes that host galaxies in the survey, as well as the properties of the halo environment. Halo and galaxy formation and evolution lead to a non-conserved comoving number density (e.g. due to mergers), that is reflected in nonzero $b_{\rm e}$, which then modulates the Doppler contribution. The idealised case is

the conservation of the comoving number density, corresponding to $b_e = 0$. In a real scenario, processes such as mergers will produce a nonzero b_e. It can be positive (more galaxies in a comoving volume) or negative (less galaxies), and it can change sign. Both parameters affect the observed fluctuations in number density.

The relations (3.4), (3.7) and (3.8) are expressed in terms of quantities at the source. It is often more convenient to rewrite them in terms of the corresponding observer quantities N_g, z and F:

$$N_g(z, F_c) = \frac{\chi^2(z)}{H(z)} \int_{F_c}^{\infty} dF \, \frac{\Phi(z, F)}{F_*(z)} \,, \tag{3.9}$$

$$Q(z, F_c) = -\frac{\partial \ln N_g(z, F_c)}{\partial \ln F_c} \,, \tag{3.10}$$

$$b_e(z, F_c) = -\frac{\partial \ln N_g(z, F_c)}{\partial \ln(1+z)} - \frac{d \ln H(z)}{d \ln(1+z)} + \frac{2(1+z)}{\chi(z) H(z)} \,. \tag{3.11}$$

Here $F_* = L_*/(4\pi\, D_L^2)$ and we used $dL/L_* = dF/F_*$ and $\partial/\partial \ln L_c = \partial/\partial \ln F_c$, since the integral and derivative are at fixed z.

Note that it is common to use a different (but equivalent) definition of magnification bias, as in section 1.5 and (2.10):

$$s = -\frac{2}{5} \frac{\partial \ln n_g}{\partial \ln L_c} = -\frac{2}{5} \frac{\partial \ln N_g}{\partial \ln F_c} = \frac{\partial \log_{10} n_g}{\partial M_c} = \frac{\partial \log_{10} N_g}{\partial m_c} \equiv \frac{2}{5} \mathcal{Q} \,. \tag{3.12}$$

Here $M = m - 5 \log_{10}(D_L/10\,\mathrm{pc})$ is the absolute magnitude and $m = -2.5 \log_{10} F + \mathrm{const}$ is the apparent magnitude.

From the expressions (3.4), (3.7) and (3.8) we find:

$$Q(a, L_c) = \frac{L_c(a)}{L_*(a)} \frac{\Phi(a, L_c)}{n_g(a, L_c)} \,, \tag{3.13}$$

$$b_e(a, L_c) = \frac{1}{n_g(a, L_c)} \int_{L_c(a)}^{\infty} dL \, \frac{\partial}{\partial \ln a} \left[\frac{\Phi(a, L)}{L_*(a)} \right] . \tag{3.14}$$

The alternative definition (3.6) of the luminosity function leads to the equivalent expressions

$$Q(a, L_c) = \frac{\hat{\Phi}(a, L_c)}{n_g(a, L_c)} \,, \tag{3.15}$$

$$b_e(a, L_c) = \frac{1}{n_g(a, L_c)} \int_{L_c(a)}^{\infty} d \ln L \, \frac{\partial \hat{\Phi}(a, L)}{\partial \ln a} \,, \tag{3.16}$$

and similarly in terms of z and F.

3.3.1 Caveat regarding evolution bias

There is a subtle and important point associated with (3.14): these expressions follow strictly from the use of *partial* derivatives in the definition (3.8). The use of the *total* derivative gives a very different result (see also [124]). Implementing the Leibniz integral rule to compute the total derivative leads to:

$$\frac{\mathrm{d}\ln n_{\mathrm{g}}}{\mathrm{d}\ln a} = \frac{\partial \ln n_{\mathrm{g}}}{\partial \ln a} + \frac{\partial \ln n_{\mathrm{g}}}{\partial \ln L_{\mathrm{c}}}\frac{\mathrm{d}\ln L_{\mathrm{c}}}{\mathrm{d}\ln a} = b_{\mathrm{e}} + 2\left(1+\frac{1}{\chi\mathcal{H}}\right)\mathcal{Q}\,, \tag{3.17}$$

where we used (3.1) in the second equality. The same result follows if we use variables z and F_{c}. Therefore, (3.17) makes it clear that for a realistic sky survey ($\mathcal{Q} \neq 0$) *the total log-derivative of number density is not the correct expression for the evolution bias.*

To illustrate this point, let us consider a simple toy model with luminosity function

$$\Phi = \phi_{*0}(1+z)\,\mathrm{e}^{-L/L_*}\,, \tag{3.18}$$

where ϕ_{*0} is constant and $L_* = L_{*0} = \text{const}$. From here onwards we adopt the background redshift ($z = a^{-1} - 1$) instead of the scale factor. Then by (3.4) and (3.13),

$$n_{\mathrm{g}} = \phi_{*0}(1+z)\mathrm{e}^{-L_{\mathrm{c}}/L_{*0}}\,, \quad \mathcal{Q} = \frac{L_{\mathrm{c}}}{L_{*0}}\,. \tag{3.19}$$

The derivative of n_{g} in (3.19) gives

$$\frac{\mathrm{d}\ln n_{\mathrm{g}}}{\mathrm{d}\ln(1+z)} = 1 + \frac{L_{\mathrm{c}}}{L_{*0}}\frac{\mathrm{d}\ln L_{\mathrm{c}}}{\mathrm{d}\ln(1+z)}\,. \tag{3.20}$$

Using the definition (3.14) of the evolution bias, we find

$$b_{\mathrm{e}} = -\frac{\partial \ln n_{\mathrm{g}}}{\partial \ln(1+z)} = -\frac{1}{n_{\mathrm{g}}}\int_{L_{\mathrm{c}}}^{\infty}\frac{\mathrm{d}L}{L_{*0}}\frac{\partial\Phi}{\partial\ln(1+z)} = -1\,. \tag{3.21}$$

Therefore, the general result of (3.17) is verified by illustrating the difference between the total and partial derivatives using the toy model (equations (3.19)–(3.21)). An example for a more realistic Stage IV Hα cosmological survey like Euclid is shown in Figure 3.1. Details of this model can be found in subsection 3.4.1.

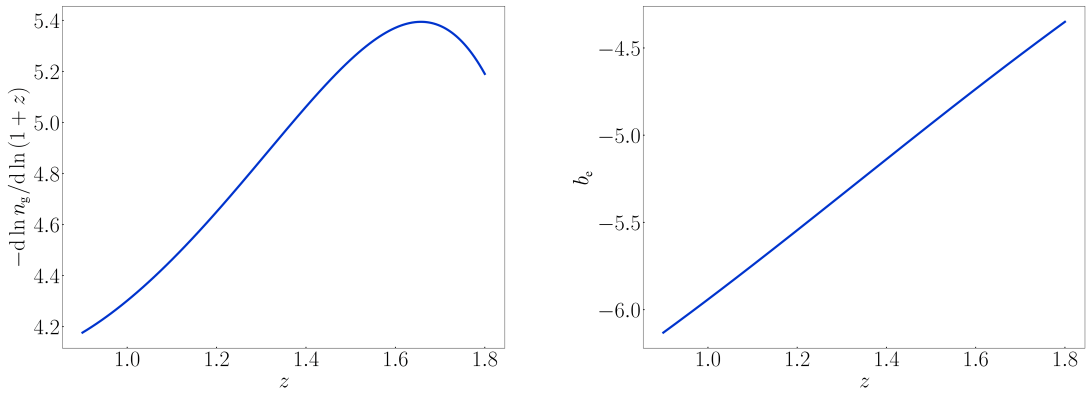

Fig. 3.1 The difference between the logarithmic total derivative of number density (*left*) and the partial derivative, i.e. the evolution bias (*right*), for a Hα Model 3 luminosity function.

When dealing with survey data or simulated data, the luminosity function is in principle known as a function of luminosity in each redshift bin. Then the tracer properties can be extracted as follows.

- The number density in each redshift bin is a simple luminosity integral (a sum over luminosity bins) of the luminosity function [see (3.4)].
- Then the magnification bias is given by a simple ratio at the luminosity threshold of the luminosity function and the number density [see (3.13)].
- By contrast, the direct expression for b_e in (3.14) is a luminosity integral in each redshift bin of the redshift partial derivative of the luminosity function.
- For b_e, it is simpler to numerically determine the total redshift derivative of the computed number density and then algebraically compute the evolution bias via (3.17):

$$b_\mathrm{e} = -\frac{\mathrm{d}\ln n_\mathrm{g}}{\mathrm{d}\ln(1+z)} - 2\left(1+\frac{1+z}{\chi H}\right)\mathcal{Q}\,. \tag{3.22}$$

Practically speaking, it is more convenient to express (3.22) in terms of the observed number density contrast, thus from (3.3) we find

$$b_\mathrm{e} = -\frac{\mathrm{d}\ln N_\mathrm{g}}{\mathrm{d}\ln(1+z)} - \frac{\mathrm{d}\ln H}{\mathrm{d}\ln(1+z)} + \frac{2(1+z)}{\chi H} - 2\left(1+\frac{1+z}{\chi H}\right)\mathcal{Q}\,. \tag{3.23}$$

Comparing with [43], we agree with their equation (33), except for a typo: their $\partial \log N_{\rm g}/\partial \log(1+z)$ should be replaced by the total derivative $\mathrm{d}\log N_{\rm g}/\mathrm{d}\log(1+z)$[1].

3.4 Spectroscopic galaxy surveys

In the following section we build upon the theoretical background established in section 3.2 and section 3.3. The principles explained in these sections will now be applied to the specific surveys we employed in our analysis. First, we consider the more traditional cosmological surveys that observe in the optical and near-infrared bands. We define the luminosity function models for Euclid-like Hα and DESI's BGS surveys, and compute them for a range of different detection sensitivities. We then determine the expression for the comoving number density and plot $n_{\rm g}$ corresponding to different flux cuts. Consequently, we compute the astrophysical parameters $b_{\rm e}$ and $\mathcal{Q}$, and how they evolve with redshift for different $F_{\rm c}$ or $m_{\rm c}$. As mentioned previously, these astrophysical parameters are survey dependent, and play an important role in the observed number density contrast via the light-cone effects.

3.4.1 Euclid-like Hα survey

Euclid[2] space telescope is planned to launch in 2022, with a Near Infrared Spectrometer and Photometer (NISP) instrument which is designed to detect galaxies in the near-infrared (NIR) band. In our forecasts we only consider the spectroscopic observations since we require high redshift accuracy for our analysis. The spectroscopic channel will be equipped with 4 different low resolution near-infrared grisms, 3 "red" (1250−1850nm) and 1 "blue" (920 − 1250 nm), but no slit ("slitless spectroscopy"). The survey will measure the redshifts of up to 30 million Hα galaxies over 15 000 deg^2 in the redshift range $0.9 \leq z \leq 1.8$ [125].

Based on several datasets, [126] have presented fits for Hα luminosity functions as a function of redshift. We consider a Stage IV Hα spectroscopic survey similar to Euclid. The updated luminosity function given by [125] corresponds to Model 3 in [126].

The best-fit to the Model 3 luminosity function of the form (3.5) is the broken power law case:

$$g(y) = \frac{y^{\alpha}}{1+(\mathrm{e}-1)y^{\nu}}\,, \tag{3.24}$$

[1] Without this replacement, our (3.11) shows that their equation (33) leads to $\mathcal{Q} = 0$.
[2] www.euclid-ec.org

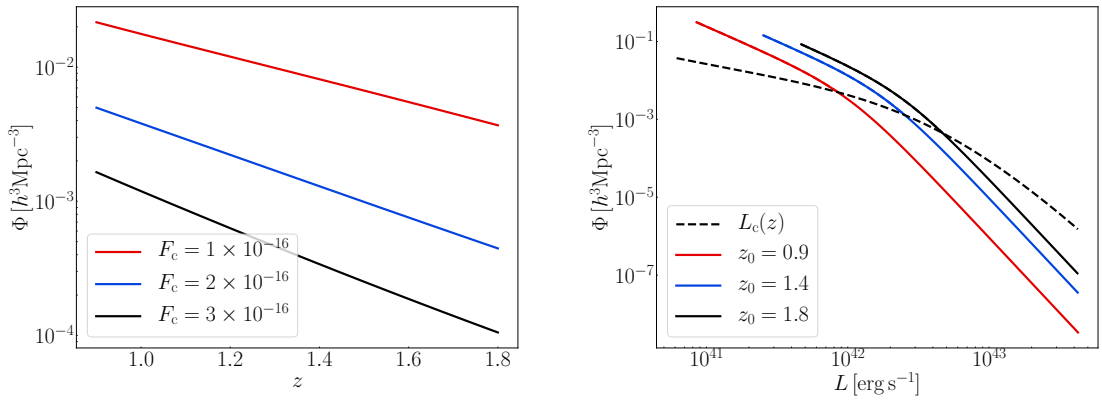

Fig. 3.2 Stage IV Hα survey (Model 3) luminosity function. *Left:* $\Phi(z, L_c)$, at the threshold luminosity L_c, for 3 flux cuts, using (3.1). *Right:* $\Phi(z_0, L)$, at 3 fixed redshifts. The threshold luminosity $L_c(z)$, with $F_c = 2 \times 10^{-16}\,\mathrm{erg\,cm^{-2}\,s^{-1}}$, is shown by the dashed line.

where $\alpha - \nu$ is the bright-end slope. The factor $\mathrm{e} - 1$ is chosen so that L_* is the luminosity at which Φ falls to 1/e of the faint-end power law, as in the Schechter case. The expressions for $\phi_*(z)$ and $L_*(z)$ from [126] are given by:

$$\log L_*(z) = \log L_{*\infty} + \left[\frac{1.5}{(1+z)}\right]^{\beta} \log\left[\frac{L_*(0.5)}{L_{*\infty}}\right], \quad \phi_* = \phi_{*0}\,, \tag{3.25}$$

where

$$L_*(0.5) = 10^{41.733}\ \mathrm{erg\ s^{-1}}\,, \quad L_{*\infty} = 10^{42.956}\ \mathrm{erg\ s^{-1}}\,, \quad \phi_{*0} = 10^{-2.92}\ \mathrm{Mpc^{-3}}\,,$$
$$\alpha = -1.587\,, \quad \nu = 2.288\,, \quad \beta = 1.615\,. \tag{3.26}$$

In Figure 3.2, we show the luminosity function at the luminosity cut against redshift for 3 different flux cuts (*left*), and against luminosity at 3 redshifts (*right*), showing also the threshold luminosity.

Therefore, we can compute the number density and magnification bias using (3.4) and (3.13) respectively:

$$n_g(z, y_c) = \phi_*(z)\, G(y_c) \tag{3.27}$$

$$\mathcal{Q}(z, y_c) = y_c \frac{g(y_c)}{G(y_c)}\,, \tag{3.28}$$

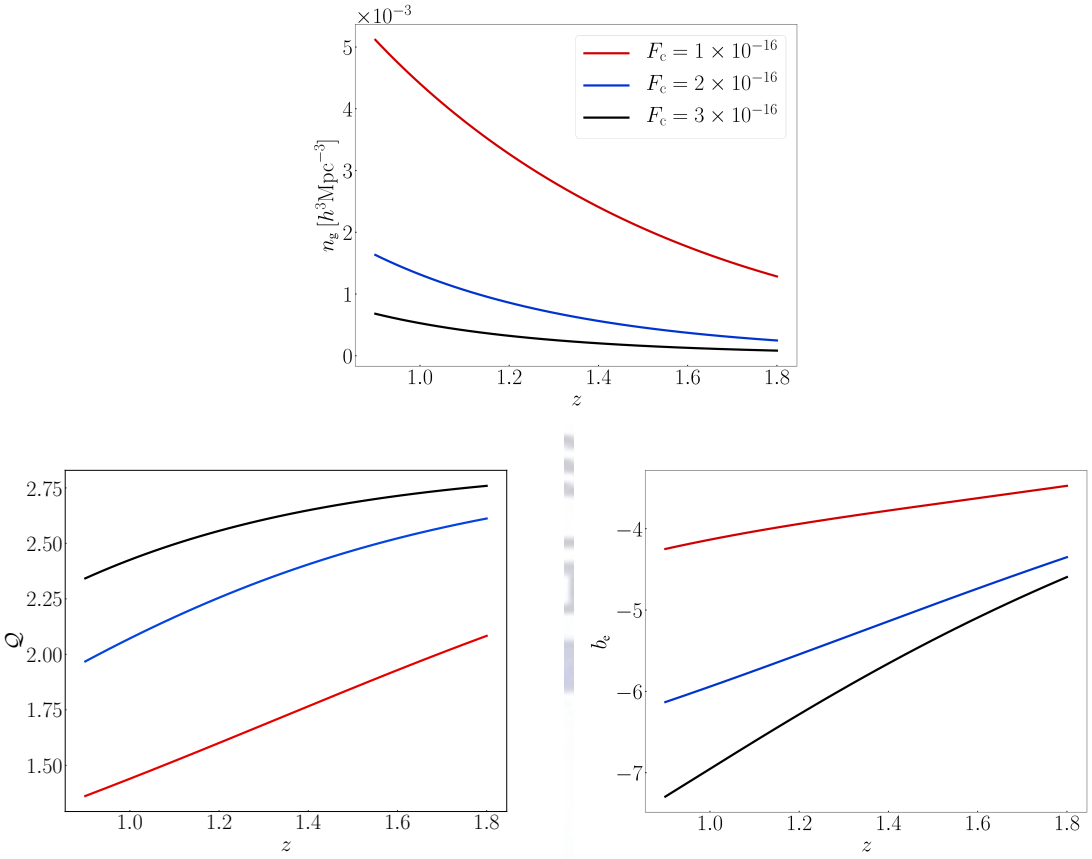

Fig. 3.3 Stage IV Hα survey (Model 3): number density (*top*), magnitude bias (*bottom left*) and evolution bias (*bottom right*), for 3 different flux cuts (in units erg cm^{-2} s^{-1}).

where

$$G(y_c) = \int_{y_c}^{\infty} \mathrm{d}y\, g(y)$$

needs to be evaluated numerically. Using the total derivative to compute b_e, we need

$$\frac{\mathrm{d}\ln G(y_c)}{\mathrm{d}\ln(1+z)} = \frac{\mathrm{d}\ln G(y_c)}{\mathrm{d}\ln y_c}\,\frac{\mathrm{d}\ln y_c}{\mathrm{d}\ln(1+z)} = -\frac{y_c\, g(y_c)}{G(y_c)}\left[\frac{\mathrm{d}\ln L_c}{\mathrm{d}\ln(1+z)} - \frac{\mathrm{d}\ln L_*}{\mathrm{d}\ln(1+z)}\right], \quad (3.29)$$

then (3.22) and (3.28) give

$$b_e(z, y_c) = -\frac{\mathrm{d}\ln\phi_*(z)}{\mathrm{d}\ln(1+z)} - \frac{\mathrm{d}\ln L_*(z)}{\mathrm{d}\ln(1+z)}\,\mathcal{Q}(z, y_c)\,. \quad (3.30)$$

Note how the derivative of the luminosity threshold L_c in (3.29) has been cancelled out and replaced by a derivative of L_* in (3.30).

Alternatively, we can determine b_e via the definition (3.14) to check the result. We start with

$$\frac{\partial \ln(\Phi/L_*)}{\partial \ln(1+z)} = \frac{\mathrm{d}\ln\phi_*}{\mathrm{d}\ln(1+z)} - \frac{\mathrm{d}\ln L_*}{\mathrm{d}\ln(1+z)} + \frac{\mathrm{d}\ln g}{\mathrm{d}\ln y}\frac{\partial \ln y}{\partial \ln(1+z)}\,, \tag{3.31}$$

which leads to

$$\begin{aligned} b_e &= -\frac{1}{\phi_* G(y_c)}\int_{y_c}^{\infty} \mathrm{d}y\, \phi_*\, g\left[\frac{\mathrm{d}\ln\phi_*}{\mathrm{d}\ln(1+z)} - \frac{\mathrm{d}\ln L_*}{\mathrm{d}\ln(1+z)} - \frac{y}{g}\frac{\mathrm{d}g}{\mathrm{d}y}\frac{\mathrm{d}\ln L_*}{\mathrm{d}\ln(1+z)}\right] \\ &= -\frac{\mathrm{d}\ln\phi_*}{\mathrm{d}\ln(1+z)} + \frac{\mathrm{d}\ln L_*}{\mathrm{d}\ln(1+z)} + \frac{\mathrm{d}\ln L_*}{\mathrm{d}\ln(1+z)}\frac{1}{G(y_c)}\int_{y_c}^{\infty}\mathrm{d}y\, y\,\frac{\mathrm{d}g}{\mathrm{d}y}\,. \end{aligned} \tag{3.32}$$

Integrating by parts, we recover (3.30). Figure 3.3 shows the associated number density, magnitude bias and evolution bias, for 3 different flux cuts.

The physical properties of the Euclid sample determine the true luminosity function – this can be estimated via simulations and will be measured when the survey is operating. In order to forecast the precision of the measurements expected from a Euclid-like Hα survey, we assume that the sensitivity of Euclid is $F_c = 2\times10^{-16}\,\mathrm{erg\,cm^{-2}\,s^{-1}}$. The corresponding number density, magnitude bias and evolution bias was computed, and for convenience we also determined the fitting functions:

$$n_g(z) = 0.00363\, z^{-0.910}\, \mathrm{e}^{0.402z} - 0.00414 \quad h^3\mathrm{Mpc}^{-3}\,, \tag{3.33}$$

$$\mathcal{Q}(z) = 0.583 + 2.02z - 0.568z^2 + 0.0411z^3\,, \tag{3.34}$$

$$b_e(z) = -7.29 + 0.470z + 1.17z^2 - 0.290z^3\,. \tag{3.35}$$

3.4.2 DESI-like bright galaxy survey

The Dark Energy Spectroscopic Instrument (DESI)[3] is a ground-based experiment whose spectrometer will determine the redshift of millions of galaxies with a redshift resolution of around 1%. The survey will target, among others, Luminous Red Galaxies (LRG), Emission Line Galaxies (ELG), Quasars and a Bright Galaxy Sample (BGS) [127]. The BGS sample is at low redshifts in the range $0.05 < z < 0.58$, while the others are at higher redshifts. Here we consider a DESI-like BGS survey only, as a low-redshift complement to a Euclid-like Hα survey. DESI will conduct an optical survey covering $15\,000\,\mathrm{deg}^2$ and expecting to detect 1.2 million bright galaxies [127].

[3] www.desi.lbl.gov

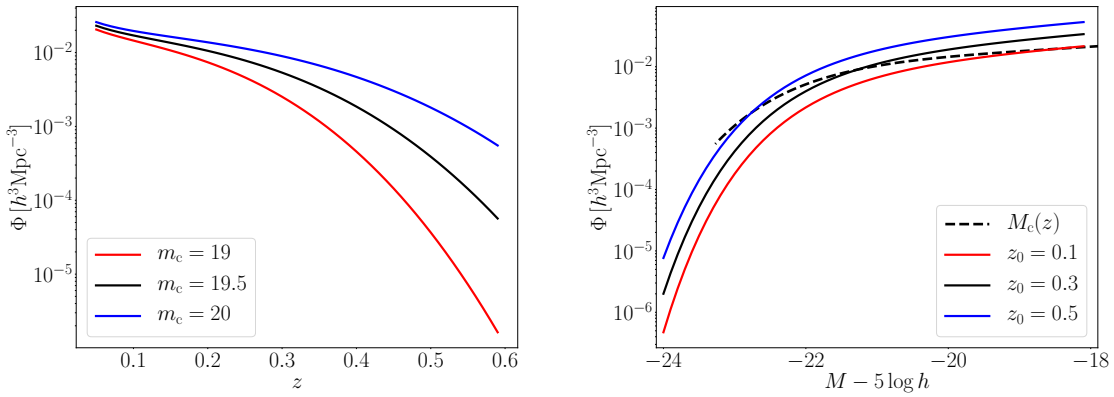

Fig. 3.4 DESI-like BGS luminosity function. *Left:* $\Phi(z, M_c)$, at the absolute magnitude threshold for 3 different apparent magnitude cuts, where $M = m - 5\,\log_{10}(d_L/10\,\mathrm{pc})$. *Right:* $\Phi(z_0, M)$, at 3 fixed redshifts, showing also the threshold absolute magnitude (dashed) with apparent magnitude cut $m_c = 20$.

If a survey measures galaxy fluxes in fixed wavelength bands, this leads to a K-correction for the redshifting effect on the bands. In that case, it is standard to work in terms of dimensionless magnitudes. The correction to the threshold absolute magnitude is

$$M_c(z) = m_c - 5\log\left[\frac{D_L(z)}{10\,\mathrm{pc}}\right] - K(z)\,, \tag{3.36}$$

where the apparent magnitude cut is m_c.

For the DESI Bright Galaxy Sample (BGS), we follow [66, 84, 127], making small adjustments. We use a Schechter luminosity function of the form (3.5), with

$$g(y) = (0.4\ln 10)\,10^{-0.4(\alpha+1)y}\,\exp\left(-10^{-0.4y}\right) \quad \text{where} \quad y = M - M_*(z)\,. \tag{3.37}$$

The number density of the DESI BGS will closely follow the Galaxy and Mass Assembly (GAMA) survey [127, 128]. Therefore we can use the r-band parameters in Table 5 of [129], with fiducial redshift $z_0 = 0.1$ (which is where the magnitudes are K-corrected) in the luminosity function (3.37):

$$\alpha = -1.23\,, \quad \phi_*(z) = 10^{-2.022+0.92\,z}\ h^3\mathrm{Mpc}^{-3}\,, \quad M_*(z) = 5\log_{10} h - 20.65 - 0.6\,z\,.$$

The K-correction is modelled as $K = 0.87\,z$, following [84], and we take $m_c = 20$, following [128]. In Figure 3.4, we show the luminosity function at the absolute magnitude cut against redshift for 3 different apparent magnitude cuts (*left*), and

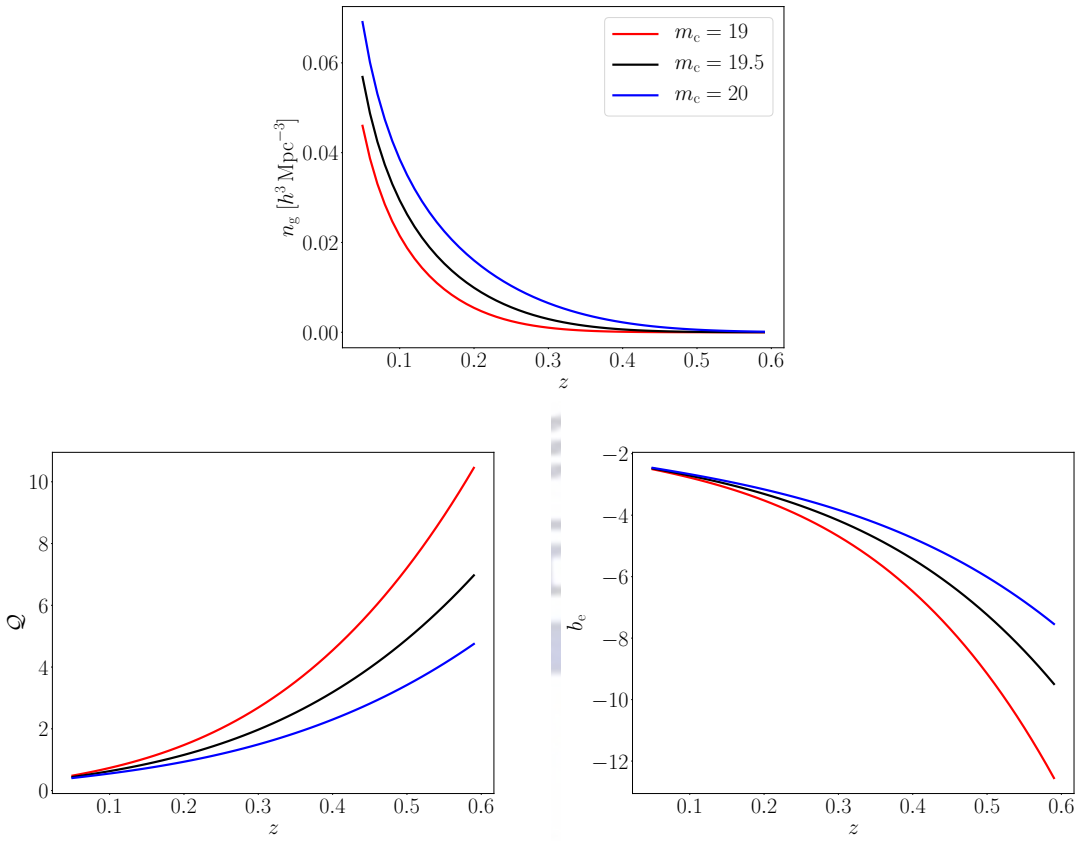

Fig. 3.5 DESI-like BGS number density (*top*), magnitude bias (*bottom left*) and evolution bias (*bottom right*), at 3 different limiting apparent magnitudes.

against absolute magnitude at 3 redshifts (*right*), showing also the threshold absolute magnitude (*dashed*).

As before, the luminosity function is employed to compute the galaxy number density, magnification bias and evolution bias via:

$$n_g(z, M_c) = \int_{-\infty}^{M_c(z)} \mathrm{d}M\, \Phi(z, M)\,, \tag{3.38}$$

$$\mathcal{Q}(z, M_c) = \frac{5}{2}\frac{\partial \log_{10} n_g(z, M_c)}{\partial M_c} = \frac{5}{2\ln 10}\frac{\Phi(z, M_c)}{n_g(z, M_c)}\,, \tag{3.39}$$

$$b_e(z, M_c) = -\frac{1}{n_g(z, M_c)}\int_{-\infty}^{M_c(z)} \mathrm{d}M\, \frac{\partial \Phi(z, M)}{\partial \ln(1+z)}\,. \tag{3.40}$$

In Figure 3.5 we show the the associated number density, magnitude bias and evolution bias, for 3 different magnitude cuts. Comparing Figure 3.3 with Figure 3.5, we find that the $\mathcal{Q}$ has a similar trend with redshift, but $\mathrm{d}b_e/\mathrm{d}z$ has an opposite sign.

This could be due to the types of galaxies and/or to a different evolution at low and high redshifts.

We can avoid the need to compute the integral in (3.40) as follows. We compute the total derivative:

$$\frac{\mathrm{d}n_{\mathrm{g}}}{\mathrm{d}z} = \int_{-\infty}^{M_{\mathrm{c}}} \mathrm{d}M \, \frac{\partial \Phi}{\partial z} + \frac{\mathrm{d}M_{\mathrm{c}}}{\mathrm{d}z} \, \Phi_{\mathrm{c}} = \int_{-\infty}^{M_{\mathrm{c}}} \mathrm{d}M \, \frac{\partial \Phi}{\partial z} + \frac{2 \ln 10}{5} \, \frac{\mathrm{d}M_{\mathrm{c}}}{\mathrm{d}z} \, \mathcal{Q} \, n_{\mathrm{g}} \,, \tag{3.41}$$

where we used (3.39). This leads to a modification of (3.22) for the photometric case, using (3.36):

$$b_{\mathrm{e}} = -\frac{\mathrm{d} \ln n_{\mathrm{g}}}{\mathrm{d} \ln(1+z)} - 2 \left[1 + \frac{1+z}{\chi H} + \frac{2 \ln 10}{5} \, \frac{\mathrm{d}K}{\mathrm{d} \ln(1+z)} \right] \mathcal{Q} \,. \tag{3.42}$$

For the BGS sensitivity, we assumed $m_{\mathrm{c}} = 20$, in order to include the faint sample [130]. The parameters have been slightly adjusted from [129] (within 1σ uncertainty) to better represent the number densities given in Table 2 of [66]. The true luminosity functions will be estimated when the surveys take data, and the data will determine how accurate the simple models of luminosity function are.

The fitting functions of DESI's BGS survey for the number density, magnitude bias and evolution bias, with $m_{\mathrm{c}} = 20$, are given by:

$$n_{\mathrm{g}}(z) = 0.031 \, z^{-0.373} \, \mathrm{e}^{-5.85z} - 0.002 \quad h^3 \mathrm{Mpc}^{-3} \,, \tag{3.43}$$

$$\mathcal{Q}(z) = 0.282 + 2.36z + 2.27z^2 + 11.1z^3 \,, \tag{3.44}$$

$$b_{\mathrm{e}}(z) = -2.25 - 4.02z + 0.318z^2 - 14.6z^3 \,. \tag{3.45}$$

3.5 21cm HI surveys (SKAO-like)

We now turn our attention to a relatively new observational technique, to measuring neutral Hydrogen (HI) in the radio band via the 21cm line emission. The abundance of Hydrogen in the Universe have been known for a long time, and the idea of using it to trace the matter distribution of the Universe is not a novel one. A simple explanation why this technique has not been considered until recently, is that only now modern radio receivers are sensitive enough to detect HI and extract a cosmological signal. Following the end of the epoch of reionisation, the vast majority of neutral Hydrogen are contained within galaxies [131]. Therefore, the emission of HI is a good tracer of the underlying dark matter distribution. We are able to detect the neutral Hydrogen atom via the 21cm emission line originating from the hyperfine spin-flip transition of

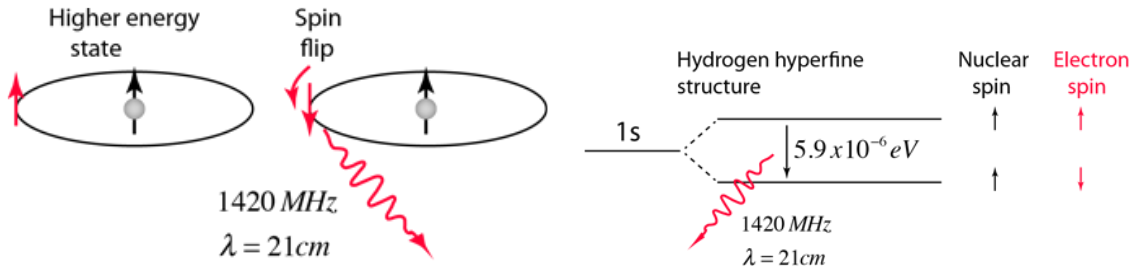

Fig. 3.6 The spin-flip transition of a neutral Hydrogen atom emitting a photon of wavelength $\lambda_{21} = 21$cm (*left*). The hyperfine structure associated with the transition (*right*). Credit: R. Nave[4]

HI. The HI atom has only two distinct configuration states: the electron and proton either has the same or the opposite direction of spin (see Figure 3.6). The former configuration is associated to the higher energy state, which naturally transitions to the latter. The change in energy releases a photon of wavelength λ_{21} =21cm, corresponding to a frequency of 1420MHz.

There are two types of HI cosmological survey:

- **HI galaxy survey**
  Detecting individual galaxies via the 21cm emission line, much in the same way as Hα and other emission-line galaxies, using the interferometer mode of the radio telescope.

- **HI intensity mapping**
  Measuring the integrated 21cm intensity of the sky at a given frequency, without resolving individual galaxies, using either interferometer or single-dish mode.

3.5.1 HI galaxy surveys

The Square Kilometre Array Observatory (SKAO)[5] is planned to become the largest radio telescope array on the planet, which intends to conduct a HI galaxy survey over the redshift range $0 < z \lesssim 0.5$ and covering 5 000 deg^2. The 10 000 hr long observation is expected to detect ~ 3 million galaxies [95]. This survey will use the next-generation 197-dish mid-frequency array, which will absorb the existing 64-dish MeerKAT array. A more futuristic 'Phase 2' survey, which we denote 'SKAO2', could cover 30 000 deg^2 over the range $0.1 < z \lesssim 2$ and detect 1 billion galaxies [132].

[4] http://hyperphysics.phy-astr.gsu.edu/hbase/quantum/h21.html
[5] https://www.skatelescope.org/

As in the case of optical/NIR surveys, the number density of HI galaxies is dependent on the sensitivity threshold of the instrument. Radio surveys use the flux density S_ν, usually abbreviated as S. This is the flux per frequency, in units of $\mathrm{Jy} = 10^{-26}\,\mathrm{W\,m^{-2}\,Hz^{-1}}$.

The root-mean-square (rms) noise associated with a flux density measurement by an interferometer can be approximated by [132, 133]

$$S_{\rm rms}(\nu) = \frac{2k_{\rm B}\,T_{\rm sys}(\nu)}{A_{\rm eff}N_{\rm d}\sqrt{2\,t_{\rm p}(\nu)\,\delta\nu}}\,, \tag{3.46}$$

where $\nu = \nu_{21}/(1+z)$ is the observed frequency, in terms of the rest-frame frequency $\nu_{21} = 1420\,\mathrm{MHz}$. The system temperature, that combines instrumental and sky temperature, is denoted by $T_{\rm sys}$. The Boltzmann constant is indicated by $k_{\rm B}$, the number of dishes is $N_{\rm d}$ and $\delta\nu$ is the frequency channel width. The time per pointing

$$t_{\rm p} = t_{\rm tot}\,\frac{\theta_{\rm b}^2}{\Omega_{\rm sky}}\,, \tag{3.47}$$

depends on the total integration time $t_{\rm tot}$, the total survey area $\Omega_{\rm sky}$ and the effective primary beam (field of view) from a mosaicked sky [134]:

$$\theta_{\rm b}^2 = \frac{\pi}{8}\left[1.3\,\frac{\lambda_{21}(1+z)}{D_{\rm d}}\right]^2\,, \tag{3.48}$$

where $D_{\rm d}$ is the dish diameter and λ_{21} is the rest-frame wavelength. The effective collecting area is

$$A_{\rm eff} = \epsilon\,\frac{\pi}{4}\,D_{\rm d}^2\,, \tag{3.49}$$

where $\epsilon \sim 0.6 - 0.9$ is the aperture efficiency.

The detection limit of HI galaxies depends not only on flux threshold, but also on the observed line profile. In order to take this into account, we include an $N_{\rm cut}\,\sigma$ detection threshold so that the detection is done with sufficient spectral resolution. This leads to a detection limit [132, 133]

$$S_{\rm c}(z) = S_{\rm rms}(z)\,\frac{N_{\rm cut}}{10}\,. \tag{3.50}$$

Models of a HI luminosity function would require a relation between the HI luminosity of a galaxy and its host dark matter halo, which depends on other factors in addition to the halo mass. This would need to be calibrated against full simulations.

Table 3.1 Fitting coefficients for SKA HI galaxy surveys (3.51), details in [133].

	c_1	c_2	c_3	c_4	c_5	$S_{\rm rms}$
SKAO	5.45	1.41	15.49	0.6052	1.0859	100μJy
SKAO2	6.55	1.93	6.22	0.5504	0.8015	5μJy

An alternative approach, bypassing the need for a luminosity function, is followed by [133], which uses the S^3-SAX simulation. Each galaxy in the simulation has a redshift, an HI luminosity and a line profile. This is used to determine the number of galaxies that are expected to be detected in a survey. The result is a fitting formula for the observed angular number density $N_{\rm g}(z, S_{\rm c})$ [133], given in terms of $S_{\rm rms}$. We adopt this fitting formula, adjusting it to the detection threshold:

$$N_{\rm g}(z, S_{\rm c}) \equiv \frac{{\rm d}\mathbb{N}_{\rm g}(z, S_{\rm c})}{{\rm d}z\,{\rm d}\Omega} = 10^{c_1(S_{\rm c})}\, z^{c_2(S_{\rm c})}\, \exp\left[-c_3(S_{\rm c})z\right]\ {\rm deg}^{-2}. \tag{3.51}$$

The parameters c_i for a range of flux sensitivities $S_{\rm c}$ are given in Table 3 of [133] and summarized in Table 3.1 (see also [47, 132]). In Figure 3.7, we provide similar plots to [133] for $N_{\rm g}(z, S_{\rm c})$, against z for various $S_{\rm c}$ and against $S_{\rm c}$ for various z.

For both SKAO and SKAO2 surveys, we assume frequency resolution $\delta\nu = 50\,{\rm kHz}$ and observation time $t_{\rm tot} = 10\,000\,{\rm hr}$. For SKAO we follow the SKA Cosmology Science Working Group Red Book [95]:

$$N_{\rm d} = 197\,,\ D_{\rm d} = 15\,{\rm m},\ \Omega_{\rm sky} = 5\,000\ {\rm deg}^2,\ \epsilon = 0.66,\ N_{\rm cut} = 5\,, \tag{3.52}$$

where $T_{\rm sys}(\nu)$ is given in [95] and the $N_{\rm cut} = 5$ choice follows [133]. The system temperature is modelled by

$$T_{\rm sys} = T_{\rm rec} + 60\left(\frac{\nu}{300\,{\rm MHz}}\right)^{-2.5}\ {\rm K}\,. \tag{3.53}$$

For the futuristic SKAO2, we follow [132] and use the survey details:

$$\begin{aligned} &T_{\rm rec} = 15\,{\rm K},\ N_{\rm d} = 70\,000\,,\ D_{\rm d} = 3.1\,{\rm m},\\ &\Omega_{\rm sky} = 30\,000\ {\rm deg}^2,\ \epsilon = 0.81,\ N_{\rm cut} = 10\,. \end{aligned} \tag{3.54}$$

The $N_{\rm cut} = 10$ choice follows [133]. The results for $S_{\rm c}(z)$ are shown in Figure 3.7.

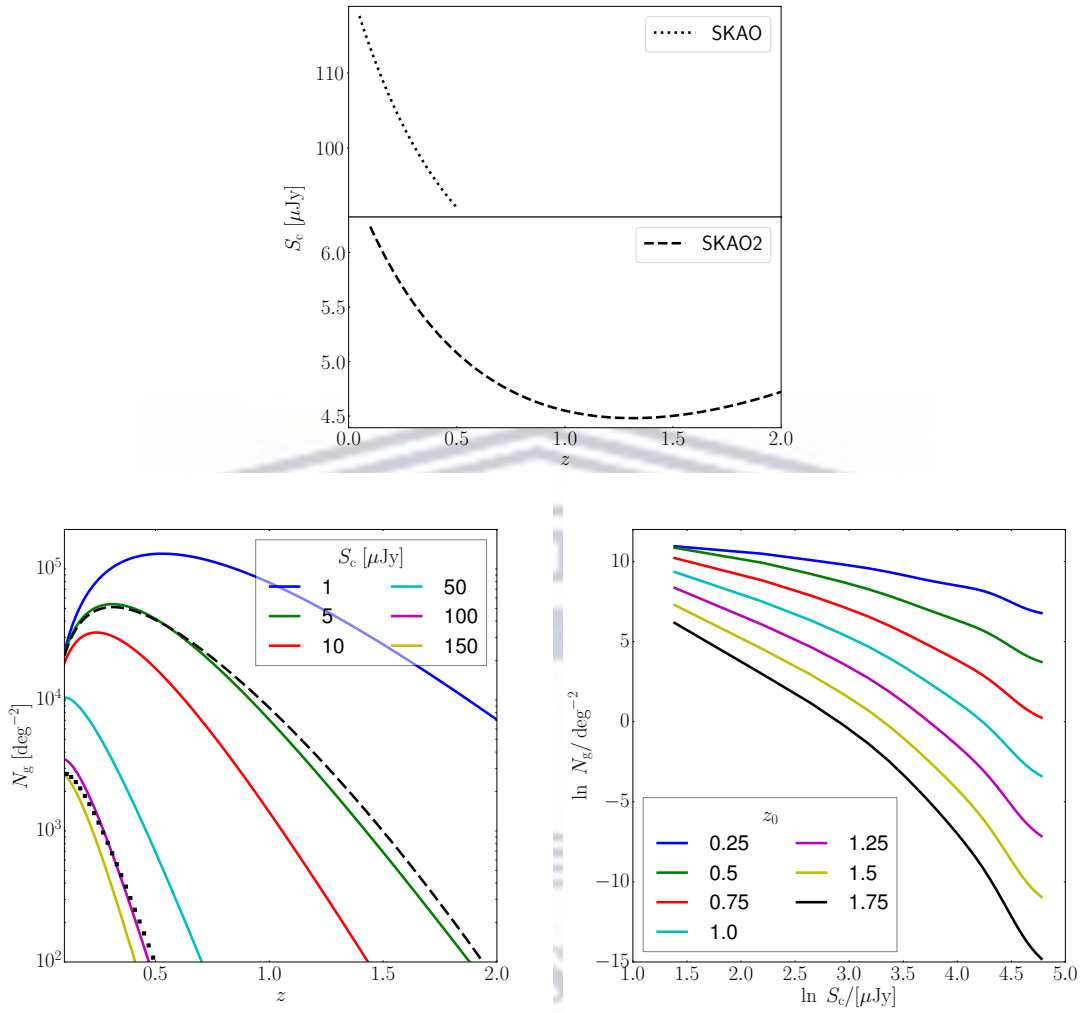

Fig. 3.7 *Top:* Flux sensitivity of SKAO HI galaxy survey (*upper panel*) and its futuristic upgrade SKAO2 (*lower panel*). *Bottom:* Observed number density of HI galaxies: against redshift at different flux cuts, showing SKAO (dotted) and SKAO2 (dashed) (*left*); against flux cut for different redshifts (*right*).

The magnification bias is computed from (3.51) as

$$\mathcal{Q} = -\frac{\partial \ln N_{\rm g}}{\partial \ln S_{\rm c}}\,, \tag{3.55}$$

which follows from (3.10), using the fact that $\partial/\partial \ln F = \partial/\partial \ln S$ for a fixed frequency channel width. At each fixed redshift z_i, we define the flux densities $S_j = S_i + j\,h$, where $j = 0, \pm 1, \pm 2$ and h is a small increment. We compute $\ln N_{\rm g}(z_i, S_j)$ from (3.51) for each $\ln S_j$ (using suitable interpolation of Table 3 in [133]). Then we use the

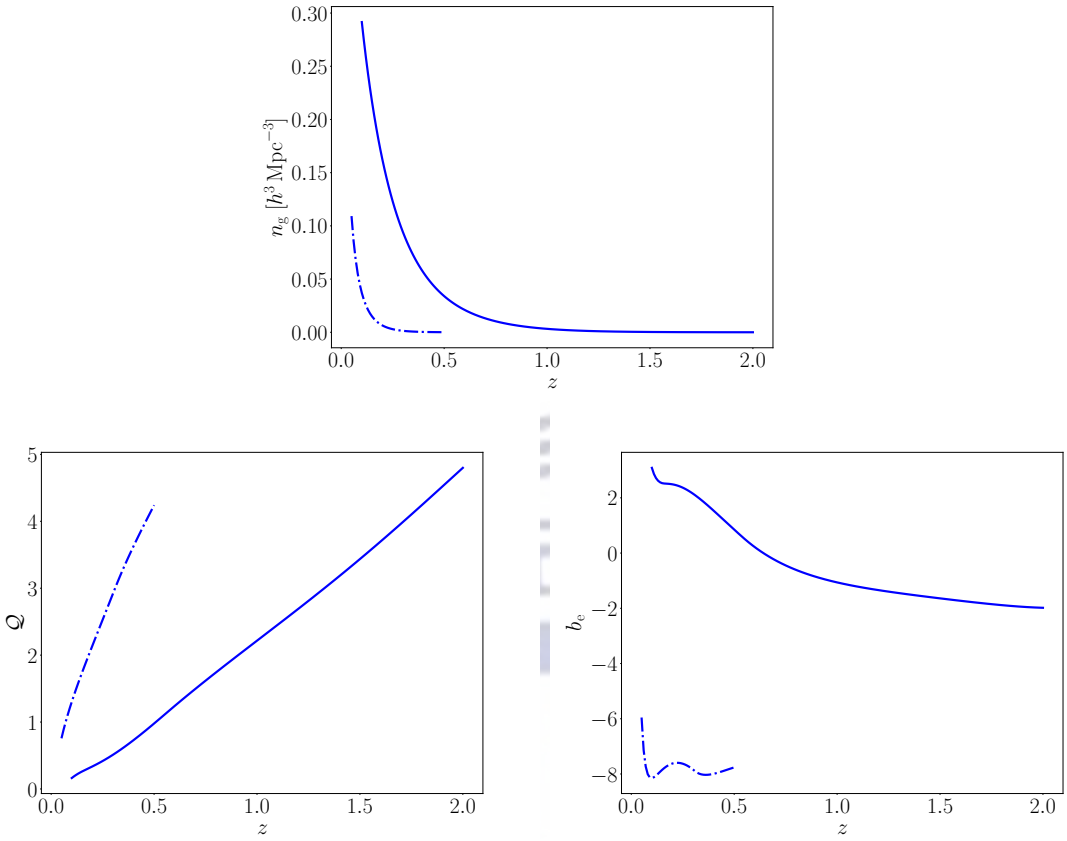

Fig. 3.8 Comoving number density (*top*), magnification bias (*bottom left*) and evolution bias (*bottom right*) for HI galaxy surveys with SKAO (*dot-dashed*) and a futuristic SKAO2 (*solid*).

five-point stencil method to compute the derivative (3.55). We tested the stability of the derivative and concluded that $h = 0.001$ was a stable interval to use in this context. This approach is related to that of [47] for an SKAO2 HI galaxy survey, which parametrises $\ln N_g(z_j, S_c)$ as a function of $\ln S_c$ for different redshifts (see also [80, 120, 135]).

For the evolution bias, we take the total redshift derivative of N_g and then use (3.3):

$$b_e = -\frac{\mathrm{d}\ln N_g}{\mathrm{d}\ln(1+z)} - \frac{\mathrm{d}\ln H}{\mathrm{d}\ln(1+z)} + 2\frac{(1+z)}{\chi H} - 2\left(1+\frac{1+z}{\chi H}\right)\mathcal{Q}\,, \tag{3.56}$$

where $\mathcal{Q}$ has already been computed as described above. The resulting comoving number density, magnification bias and evolution bias are shown in Figure 3.8.

Fitting functions for the number density, magnitude bias and evolution bias for SKAO are:

$$\begin{aligned} n_{\rm g}(z) =& 127\,z^4 - 241\,z^3 + 172\,z^2 - 55\,z + 6.66 \\ & - \exp\left(-90.9\,z^4 + 27\,z^3 - 17.1\,z^2 - 7.3\,z + 1.8\right) \quad h^3\,{\rm Mpc}^{-3}\,, \end{aligned} \tag{3.57}$$

$$\mathcal{Q}(z) = -\,51.37\,z^4 + 58.92\,z^3 - 27.13\,z^2 + 13.36\,z + 0.17\,, \tag{3.58}$$

$$\begin{aligned} b_{\rm e}(z) =& 2867\,z^4 - 4910\,z^3 + 3146\,z^2 - 892\,z + 86.3 \\ & - \exp\left(-862\,z^4 + 406.8\,z^3 - 100\,z^2 - 1.3\,z + 4.3\right)\,, \end{aligned} \tag{3.59}$$

while for SKAO2:

$$\begin{aligned} n_{\rm g}(z) =& 1.47\,z^4 - 11.7\,z^3 + 35.1\,z^2 - 47.4\,z + 24.2 \\ & - \exp\left(-0.16\,z^4 + 0.08\,z^3 - 0.65\,z^2 - 1.87\,z + 3.2\right) \quad h^3\,{\rm Mpc}^{-3}\,, \end{aligned} \tag{3.60}$$

$$\mathcal{Q}(z) = 0.28\,z^4 - 1.18\,z^3 + 1.76\,z^2 + 1.36\,z\,, \tag{3.61}$$

$$\begin{aligned} b_{\rm e}(z) =& 0.07\,z^5 - 5.47\,z^4 + 16.4\,z^3 - 19.6\,z^2 + 7.35\,z + 0.22 \\ & - \exp\left(89.2\,z^4 + 169.2\,z^3 - 102.5\,z^2 + 15.5\,z + 0.24\right)\,. \end{aligned} \tag{3.62}$$

3.5.2 HI intensity mapping surveys

In addition to the HI galaxy surveys, the SKAO will also be conducting another type of survey called Intensity Mapping (IM) survey. As opposed to galaxy surveys, IM does not require the resolution of individual galaxies. Rather, it measures the integrated line emission from the sources and infer the distribution of matter from the temperature fluctuations - as in the CMB analysis. The advantage of IM is that one can scan larger sky areas in the same amount of time, hence extract information on the large scale structure more efficiently. In this work we are interested in the HI IM survey observed by the future SKAO radio telescope array, because of the unprecedented cosmological volumes oberved by this experiment. The SKAO IM survey will cover 20 000deg^2. In addition, the observation does not only include the bright galaxies, but the fainter emissions as well - like filaments in the large-scale structure.

The integrated 21cm emission is measured in a three-dimensional pixel, which is assembled by the frequency channel width and the telescope beam, called a voxel. The frequency resolution of the instrument is $\sim$ 50kHz, which translates into a redshift accuracy of $z \sim 10^{-4}$. We are considering the single-dish configuration of the telescope

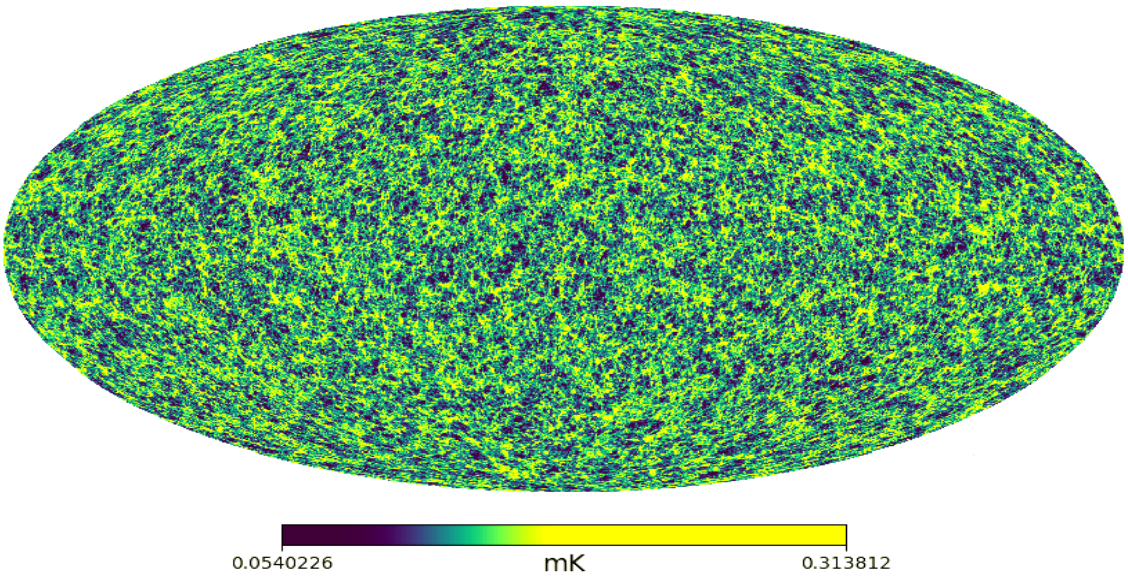

Fig. 3.9 The temperature fluctuations of a HI intensity map located at $z = 1$.

array, thus the beam is defined by

$$\beta_\ell(z_i) = \exp\left[-\frac{\ell(\ell+1)}{16\ln 2}\theta_{\rm b}^2(z_i)\right], \tag{3.63}$$

where $\theta_{\rm b} = 1.22\lambda_{21}(1+z)/D_{\rm d}$ is the effective field of view and $D_{\rm d}$ is the dish diameter. The intensity mapping angular power spectrum is modulated by the telescope beam, which leads to a loss of small-scale transverse power:

$$C_\ell^{\rm IM\,IM}(z_i, z_j) \quad \to \quad \beta_\ell(z_i)\,\beta_\ell(z_j)\,C_\ell^{\rm IM\,IM}(z_i, z_j)\,. \tag{3.64}$$

The resulting IM tomography is a three dimensional map of the temperature fluctuations at different z, with an extremely high redshift precision. In Figure 3.9 we show a temperature map of SKAO-like HI IM, centered around $z = 1$ and redshift bin width $\Delta z = 0.1$. The image was generated using software called HEALPIX.

The HI brightness temperature measured at redshift z in direction $\boldsymbol{n}$ is related to the observed number of 21cm emitters per redshift per solid angle, $N_{\rm HI}$, as follows:

$$T_{\rm HI}(z, \boldsymbol{n}) = \text{const}\,\frac{N_{\rm HI}(z, \boldsymbol{n})}{D_A(z, \boldsymbol{n})^2}\,, \tag{3.65}$$

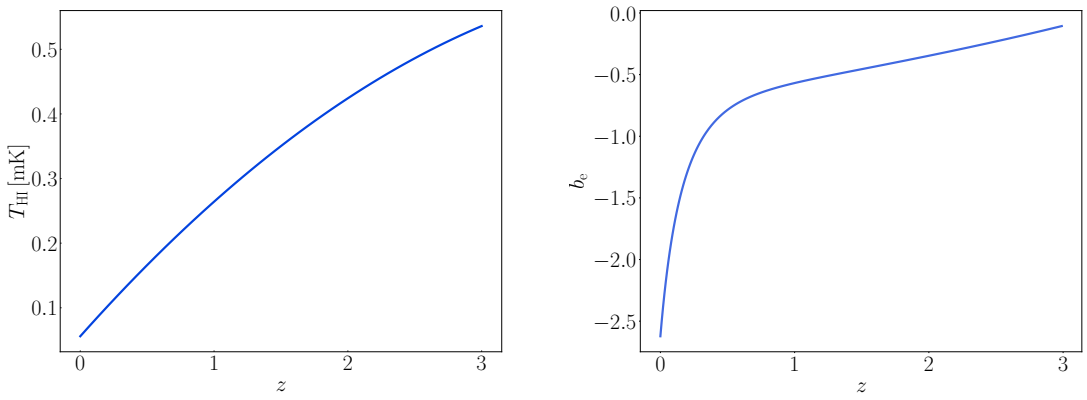

Fig. 3.10 Background temperature (*left*) and evolution bias (*right*) for post-reionisation 21cm intensity mapping.

for further details see [43, 136]. This relation implies that the surface brightness is conserved, therefore it follows that the effective magnification bias is [43, 76, 136, 137]

$$\mathcal{Q} = 1\,. \tag{3.66}$$

Considering the background quantities, (3.65) implies that

$$T_{\rm HI} = \text{const}\,\frac{n_{\rm HI}\,\chi^2\,H^{-1}}{a^2\chi^2} = \text{const}\,\frac{(1+z)^2}{H}\,n_{\rm HI}\,, \tag{3.67}$$

where $n_{\rm HI}$ is the comoving number density of HI emitters in the source rest-frame. Intensity mapping integrates over the entire luminosity function in each voxel [138]. Therefore the brightness temperature does not depend on a luminosity threshold, but depends only on redshift. By (3.67), this is also the case for the number density, so that [76, 136]

$$b_{\rm e} \equiv -\frac{\partial \ln n_{\rm HI}}{\partial \ln(1+z)} = -\frac{{\rm d}\ln T_{\rm HI}}{{\rm d}\ln(1+z)} - \frac{{\rm d}\ln H}{{\rm d}\ln(1+z)} + 2\,. \tag{3.68}$$

Equation (3.67) also leads to [131]

$$T_{\rm HI}(z) = 189h\,(1+z)^2\frac{H_0}{H(z)}\,\Omega_{\rm HI}(z)\ \ \text{mK}, \tag{3.69}$$

where $\Omega_{\rm HI}(z)$ is the comoving HI density in units of the critical density today. This is poorly constrained by current observations and we use the fit [139]:

$$T_{\rm HI}(z) = 0.056 + 0.23\,z - 0.024\,z^2 \quad \text{mK}. \tag{3.70}$$

Using the background temperature (3.70), we can find the evolution bias (3.68), which is shown in Figure 3.10. For convenience, we have also determined a fitting formula for $b_{\rm e}$, suitable for any post-reionisation HI IM survey:

$$b_{\rm e} = -0.32 - 0.11\,z + 0.06\,z^2 - \exp\left(-0.9\,z^3 + 3.12\,z^2 - 4.61\,z + 0.78\right) . \tag{3.71}$$

Note that $\mathcal{Q}$ and $b_{\rm e}$ are survey-dependent for galaxy surveys, since they depend on the survey flux cut. By contrast, for 21cm intensity mapping there is no flux limit and the evolution bias therefore depends only on the background brightness temperature and the Hubble rate, while the effective magnification bias is 1.

The evolution bias for intensity mapping has the same physical meaning as for galaxy surveys, since it is given in (3.68) by the comoving number density of 21cm emitters. However, since the IM surveys do not resolve the individual galaxies, the change of the galaxy number counts are not as easily observed, as compared to the galaxy surveys that detect individual galaxies.

3.6 Survey noise

Another important aspect necessary to include when modeling future cosmological observations is: how well will the survey be able to extract the desired signal from the measurement? The precision of the measurement is dependent on the uncertainty in the detection, which we call the survey noise. We take this uncertainty into account in our analysis by adding the noise to C_ℓ, which enters the Fisher forecast in (2.16).

3.6.1 Galaxy surveys

The main contribution of noise in the galaxy surveys is called Poisson noise, commonly known as shot-noise. The shot-noise originates from the discrete nature of galaxy observations, and an increased sample size reduces this uncertainty. The angular shot-noise power is inversely proportional to the number of galaxies observed per solid angle:

$$\mathcal{N}_\ell^{\rm g}(z_i, z_j) = \frac{1}{N_\Omega(z_i)}\,\delta_{ij}\,, \tag{3.72}$$

where N_Ω is the windowed observed number density

$$N_\Omega(z_i) = \int \mathrm{d}z\, W(z, z_i)\bar{N}_\mathrm{g}(z)\,. \tag{3.73}$$

The above equation determines the expected number of galaxies observed in the redshift bin centered about z_i. Given the precise redshift resolution of spectroscopic galaxy surveys, we have opted to use a top-hat like window function W that is smoothed at the edges [1]:

$$W(z, z_i) = \frac{1}{2\tanh(\Delta z_i/2\sigma_{zi})}\left[\tanh\left(\frac{z-z_i+\Delta z_i/2}{\sigma_{zi}}\right) - \tanh\left(\frac{z-z_i-\Delta z_i/2}{\sigma_{zi}}\right)\right], \tag{3.74}$$

where Δz_i is the redshift bin size, σ_z is the redshift resolution and $\sigma_{zi} = \sigma_z(1+z_i)$.

3.6.2 HI Intensity mapping surveys

For HI IM experiments the main source of noise is instrumental and we can neglect shot noise on the scales of interest (see Figure 3.12, *right*). For single-dish surveys, the noise is [140, 141]

$$\mathcal{N}_\ell^{\mathrm{HI}}(z_i, z_j) = \frac{4\pi\, f_\mathrm{sky}\, T_\mathrm{sys}^2(z_i)}{2N_\mathrm{d}\, t_\mathrm{tot}\, \Delta\nu}\,\delta_{ij}\,. \tag{3.75}$$

The system temperature T_sys is frequency dependent (3.53), N_d represents the number of dishes, the frequency band of observation is $\Delta\nu$, the total integration time is t_tot and the sky fraction is $f_\mathrm{sky} = \Omega_\mathrm{sky}/4\pi$.

The full SKAO observation will be conducted by a combination of two different radio antennas that measure signals using four separate receivers, each with distinct noise properties. The new phase of SKAO have a 133 dishes of 15m diameter, and will observe the high- and low-z using Band1 and Band2 receivers respectively. The precursor to SKAO is called MeerKAT, which consists of 64 radio dishes of diameter 13.5m, which will be incorporated into the total array. The dishes are equipped with Lband and UHF receivers, that detect the high and low frequencies respectfully. We need to weight the noise and beam properties from the MeerKAT dishes and the new SKAO dishes, with different diameters and receiver bands (see Table 3.2).

The contributions of the different antennas are weighted using the individual root-mean-square (RMS) error. For the UHF/L-bands and Band 1/2 we have:

$$w_\mathrm{U/L} = w_\mathrm{tot}^{-1}\,\frac{N_\mathrm{d,U/L}}{T_\mathrm{sys,U/L}^2}\,, \quad w_{1/2} = w_\mathrm{tot}^{-1}\,\frac{N_{d,1/2}}{T_\mathrm{sys,1/2}^2}\,, \tag{3.76}$$

Table 3.2 SKAO and MeerKAT: dish and receiver properties.

Receiver	Frequency range [MHz]	Redshift range	$D_{\rm d}$ [m]	# dishes
Band 1	350 – 1050	0.35–3.06	15	133
Band 2	950 – 1760	0.1–0.49	15	133
UHF-band	580 – 1015	0.4–1.45	13.5	64
L-band	900 – 1670	0.1–0.58	13.5	64

where

$$w_{\rm tot} = \frac{N_{\rm d,U/L}}{T^2_{\rm sys,U/L}} + \frac{N_{\rm d,1/2}}{T^2_{\rm sys,1/2}} \,. \tag{3.77}$$

The weighted instrumental noise for SKAO surveys is given by

$$\mathcal{T}_\ell^{\rm SKAO\,IM1/2} = w_{\rm U/L}\mathcal{T}_\ell^{\rm U/L} + w_{1/2}\mathcal{T}_\ell^{1/2} = \frac{2\pi}{\Delta\nu}\frac{f_{\rm sky}}{t_{\rm tot}}\frac{T^2_{\rm sys,eff}}{N_{\rm d,tot}} \,, \tag{3.78}$$

where $\mathcal{T}_\ell^{\rm U/L}$ is the noise for 64 MeerKAT dishes in UHF/L-bands, and $\mathcal{T}_\ell^{1/2}$ is the noises for 133 new SKA dishes in Bands 1/2 – each given by (3.75). In (3.78) $T_{\rm sys,eff}$ corresponds to the effective system temperature, which is the weighted average of the system temperatures from the individual receivers in the full telescope array.

The system temperatures, in the form $T^2_{\rm sys}/N_{\rm d}$, are shown in Figure 3.11, for the individual receivers (*left*) and for SKAO using the weighted noise (3.78) (*right*). For the MeerKAT bands the system temperature and the effective one are the same. Note that the jumps in the effective system temperature for SKAO IM1/2 arise from the fact that the frequency range of the SKAO bands and the MeerKAT bands do not perfectly overlap.

Additionally, we also have to weight the impact of the beam because the diameter of the dishes differ. The total weighted beam is simply given by

$$B_\ell^{\rm SKAO\,IM1/2} = w_{1/2}B_\ell^{1/2} + w_{\rm U/L}B_\ell^{\rm U/L} \,. \tag{3.79}$$

From here on out we refer to SKAO IM1/2 simply as IM1 and IM2 respectively.

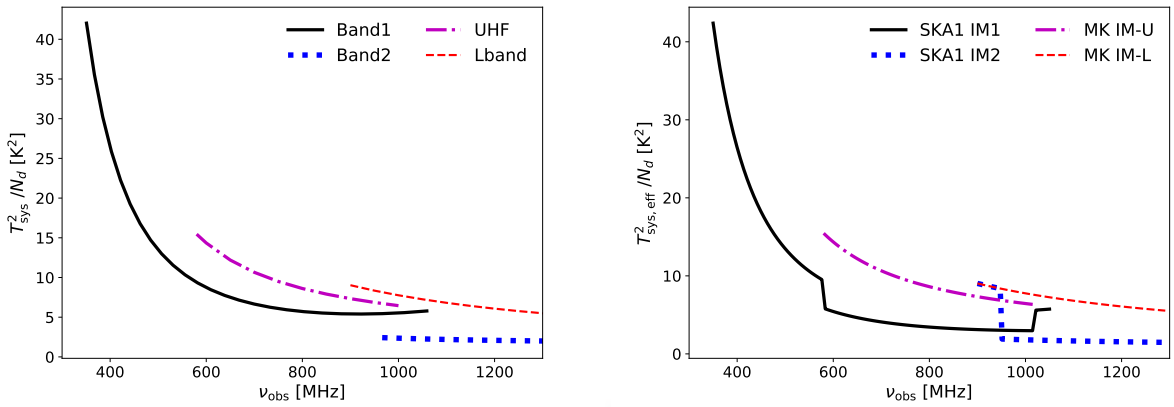

Fig. 3.11 System temperature (in the form $T^2_{\rm sys}/N_{\rm d}$) for the 4 receiver bands of HI IM (*left*) and the weighted effective system temperature for SKAO and MeerKAT (*right*).

3.6.3 Multi-tracers

In addition to looking at the noise properties of individual surveys, we also have to take into account what happens when we combine surveys via the multi-tracer technique. In the case of a MT analysis we use only the overlapping sky area, hence we fix the scanning ratio of the HI IM surveys, i.e the sky area over time. This implies that the observational time $t_{\rm tot}$ needs to be adjusted proportionally to the reduction in sky area.

Given the overlap between the BGS and IM2 surveys, and between the Hα and IM1 surveys, we need to consider the cross-shot noise. For correlations between tracers one expects an overlap in the dark matter halos seen by both surveys. An exception is for example the red and blue galaxies in photometric galaxy surveys, which by selection are disjoint tracers of the dark matter. When we consider HI IM, all halos in a voxel containing HI will contribute to the integrated temperature observed in the voxel. Some of these halos, especially the most massive ones, will host emission line galaxies which appear in spectroscopic galaxy surveys such as the DESI-like BGS survey. These overlap halos will induce a shot-noise term contribution in the cross-correlation.

The comoving HI density is given by

$$\rho_{\rm HI} = \int_{M_{\rm HI}^{\rm min}}^{M_{\rm HI}^{\rm max}} {\rm d}M\, n_h(M)\, M_{\rm HI}(M)\,, \tag{3.80}$$

where n_h is the halo mass function, $M_{\rm HI}$ is the mass of HI in a halo of mass M, and we take $M_{\rm HI}(M) \propto M^{0.6}$ [142]. The HI shot noise power spectrum is [131, 143]

$$\mathcal{N}^{\rm HI}_{{\rm sn},\ell} = \frac{H}{\chi^2}\frac{\bar{T}^2_{\rm HI}}{\rho^2_{\rm HI}}\int_{M^{\rm min}_{\rm HI}}^{M^{\rm max}_{\rm HI}} {\rm d}M\, n_h(M)\, M_{\rm HI}(M)^2\,, \tag{3.81}$$

and the galaxy shot noise power spectrum $1/N_{\rm g}$ can be determined by (3.3). The cross-shot noise power spectrum can be estimated as [92]

$$\mathcal{N}^{\times}_{{\rm sn},\ell} = \frac{1}{N_{\rm g}}\frac{\bar{T}_{\rm HI}}{\rho_{\rm HI}}\int_{M^{\rm min}}^{M^{\rm max}} {\rm d}M\, n_h(M)\, M_{\rm HI}(M)\,\Theta(M)\,, \tag{3.82}$$

where Θ is a weighting function accounting for the fraction of halos that are present in both samples. For simplicity, we dropped the redshift dependence, and in what follows we neglect the width of the bins and just take their central values. In the absence of an exact model, one can approximate that all halos within a mass range $M^{\rm min} \leq M \leq M^{\rm max}$ overlap and set $\Theta(M) = 1$ in this interval and zero elsewhere. This implicitly assumes that all halos within this mass range have HI and host a bright galaxy, which is incorrect. However, assuming $\Theta(M) = 1$ leads to an over-estimation of the noise contribution within the mass range.

In order to find $M^{\rm min}$ and $M^{\rm max}$ in (3.82), we need to estimate the halo mass ranges of each survey. The BGS survey will cover a range of higher mass halos, while the HI IM surveys cover lower mass halos which are small enough to contain neutral Hydrogen. For the BGS survey, we use abundance matching between the number of galaxies in a bin and the expected number from the halo mass function, i.e.,

$$N_{\rm g} = \frac{\chi^2}{H}\int_{M_g^{\rm min}}^{\infty} {\rm d}M\, n_h(M)\,. \tag{3.83}$$

In this approximation we assume that all massive halos will host a bright galaxy, which is not necessarily true. In fact the minimum halo mass that host an observed bright galaxy depends on the completeness of the sample. A lower completeness results in a lower minimum halo mass. This does not trivially translate into a higher cross-shot noise, but it would extend the overlap into higher redshifts. For demonstration purposes we assume the sample is complete. In a given redshift bin we perform abundance matching to find $M_g^{\rm min}$, using the Sheth-Tormen halo mass function [144] and the number density for the BGS survey, (3.86). The minimum mass is shown in Figure 3.12 (left panel), and it compares well with Figure 3.4 of [127].

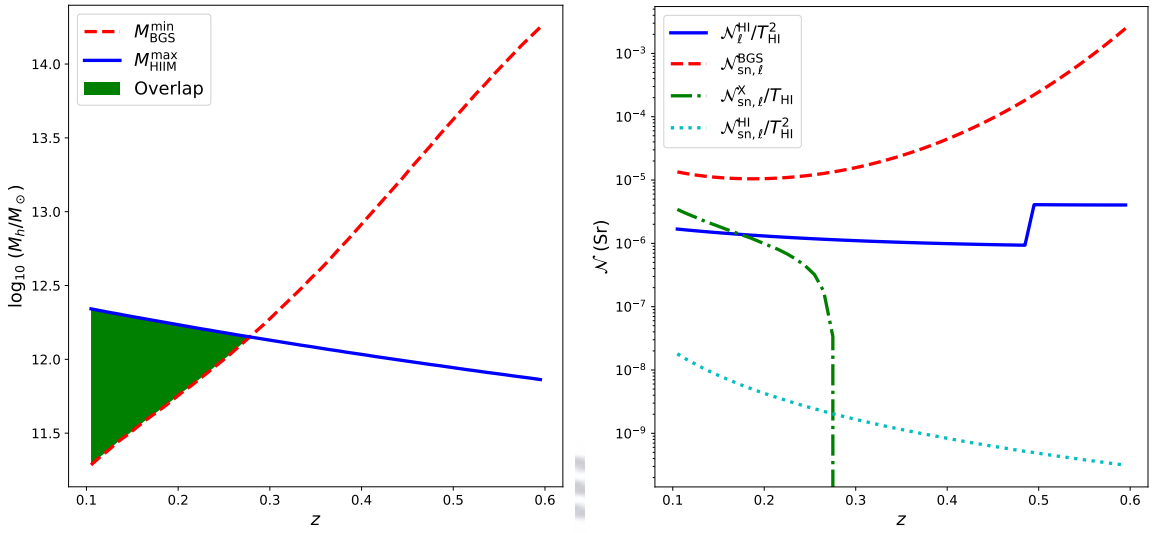

Fig. 3.12 *Left:* Mass overlap between HI IM and BGS halos. *Right:* Shot-noise power spectra for HI IM and BGS, together with the over-estimate of their cross-shot noise. The instrumental-noise power spectrum for HI IM is also shown.

In order to estimate the maximum HI halo mass, we need to determine the mass range of halos that contribute to HI IM. To this end, we assume that only halos with circular velocities between 30 and 200 km/s host HI, where [142]

$$v_{\rm circ} = 30\sqrt{1+z}\left(\frac{M}{10^{10}M_\odot}\right)^{1/3} \text{ km/s}. \tag{3.84}$$

The maximum HI halo mass is shown in Figure 3.12 (*left panel*), together with the overlap region. The overlap for BGS is only at low redshift. We do not find any mass range overlap between HI IM and the Hα survey.

The right panel of Figure 3.12 displays the shot-noise power spectra for BGS, HI IM and their cross noise. Our over-estimate of cross-shot noise is well below the galaxy shot noise and rapidly vanishes. Hence we neglect this term in our forecasts, see for example [131, 143, 145, 146]. We include the instrumental noise for HI IM, which is clearly much larger than the HI IM shot noise. The step in the instrumental noise arises from the fact that the frequency ranges of the SKAO bands and the MeerKAT bands do not perfectly match, as shown in Figure 3.11.

Since the cross-shot noise in the multi-tracer can safely be neglected in the surveys under consideration, the MT noise for N number of tracers is the diagonal matrix:

$$\mathcal{N}_\ell = \begin{bmatrix} \mathcal{N}_\ell^{11}(z_i^1, z_j^1) & 0 & \cdots & 0 \\ \cdots & \cdots & \cdots & \cdots \\ 0 & 0 & \cdots & \mathcal{N}_\ell^{NN}(z_i^N, z_j^N) \end{bmatrix}. \tag{3.85}$$

3.7 Synopsis

The observed (linear) number density contrast $\Delta_{\rm g}$ depends on three astrophysical biases, which in turn depend on the sample of galaxies considered. The linear clustering bias b has been the subject of extensive studies, therefore in this chapter we have focused on determining the magnification and evolution biases. These two biases modulate the amplitude of light-cone effects which, for forthcoming surveys, need to be included in the modeling of the two- and three-point statistics.

Forecasts for future galaxy surveys require physically self-consistent models of $\mathcal{Q}$ and $b_{\rm e}$, especially when lensing and other relativistic effects are important. Key examples when this is the case are:

- constraints on primordial non-Gaussianity [4, 43, 47, 91, 92];
- detection of the lensing potential and Doppler effect in the number counts, via the two-point statistics [40, 43, 63–73, 78, 82, 83, 91] and three-point statistics [48, 74–76];
- investigation of the possible biases on best-fit parameter values that may be induced by neglecting relativistic effects [5, 48, 79, 80, 84, 86, 147, 148].

When lensing and other relativistic effects are detectable, they can themselves provide novel probes of gravity and matter. However, such probes are only possible if magnification and evolution biases are accurately modelled [5, 43, 84, 87, 91].

For simulated or observed galaxy data, the luminosity function is in principle known as a function of luminosity in each redshift bin. Then $\mathcal{Q}$ and $b_{\rm e}$ may be extracted as follows.

- Number density $n_{\rm g}$ in each redshift bin is found from a simple luminosity integral of the luminosity function, (3.4).

Table 3.3 Basic details of the surveys.

Experiment	Tracer	Sky area $[10^3\,\mathrm{deg}^2]$	t_{tot} $[10^3\mathrm{hr}]$	Redshift range	Spectral resolution
MeerKAT IM-L	HI IM	4	4	0.1–0.58	10^{-4}
MeerKAT IM-U	HI IM	4	4	0.4–1.45	10^{-4}
SKAO IM2	HI IM	20	10	0.1–0.58	10^{-4}
SKAO IM1	HI IM	20	10	0.35–3.06	10^{-4}
SKAO1 Gal	HI galaxies	5	—	0.1–0.58	10^{-4}
SKAO2 Gal	HI galaxies	30	—	0.1–2.0	10^{-4}
Euclid-like	Hα galaxies	15	—	0.90–1.80	10^{-3}
DESI-like	Bright galaxies	15	—	0.1–0.58	10^{-3}

- Then $\mathcal{Q}$ is determined by a ratio at the luminosity threshold of the luminosity function and the number density, (3.13).
- For b_{e}, instead of using its definition, it is simpler to take a total redshift derivative of the computed n_{g} and then use $\mathcal{Q}$ to compute b_{e} via (3.22).

The survey specification of the experiments under consideration are collected and displayed in Table 3.3. The instrumental and shot-noise for HI intensity mapping and galaxy surveys are compared in Figure 3.13.

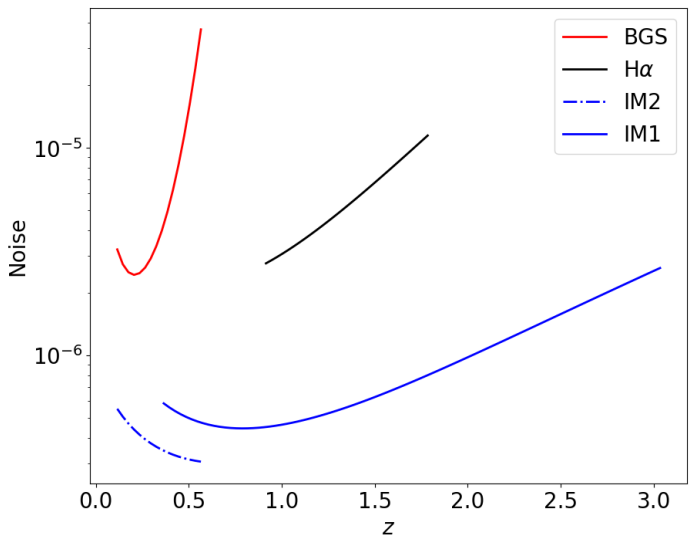

Fig. 3.13 Shot noise for galaxy surveys and instrumental noise (normalised by T_{HI}^2) for intensity mapping surveys.

3.7.1 Cosmological survey fits

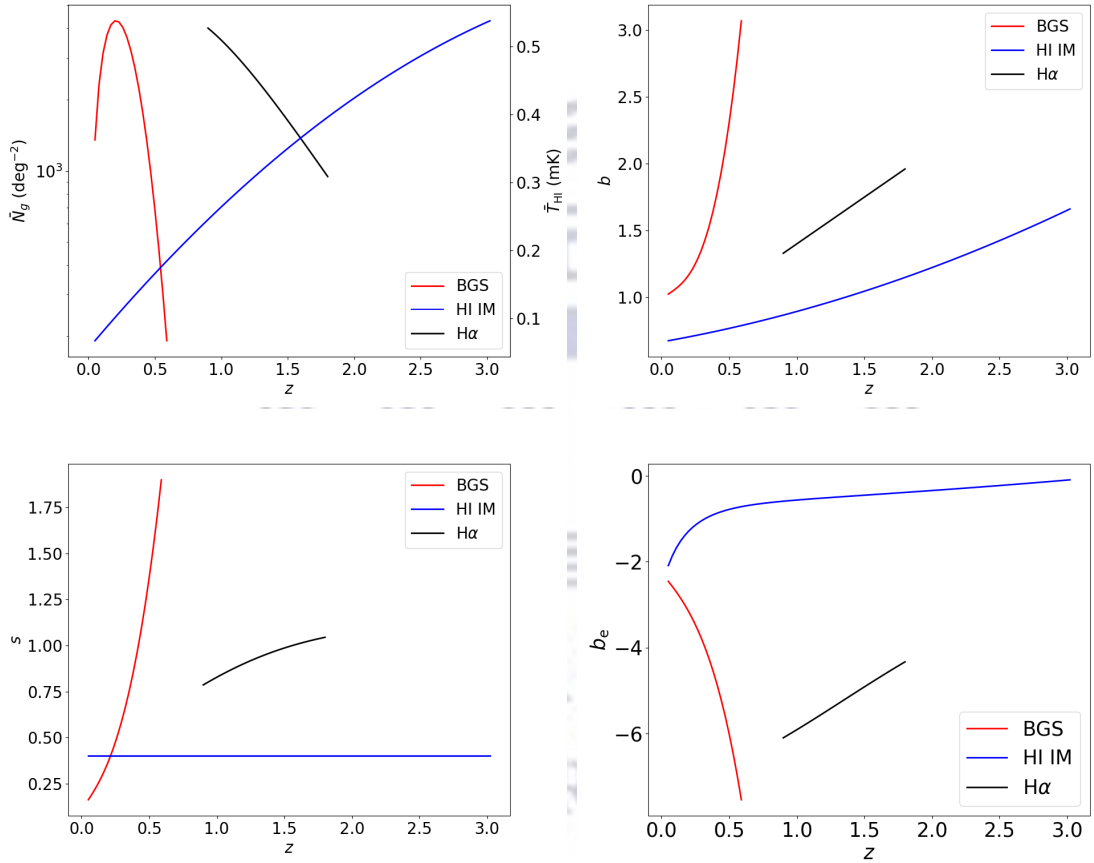

Fig. 3.14 *Top:* Number density and HI temperature in mK (*left*), and Gaussian clustering bias (*right*), for the surveys. *Bottom:* Magnification bias (*left*) and evolution bias (*right*), for the surveys.

For the reader's convenience, the fits for the observed number density and resulting astrophysical parameters used in the forecasts, *including the linear clustering bias* b, are given below:

- DESI-like BGS survey:

$$N_{\rm g} = z^{1.161} \exp\left[10.75 - \left(\frac{z}{0.27}\right)^{2.060}\right], \tag{3.86}$$

$$b = 0.99 + 0.73\,z - 1.29\,z^2 + 10.21\,z^3\,, \tag{3.87}$$

$$s = 0.113 + 0.945\,z + 0.908\,z^2 + 4.442\,z^3\,, \tag{3.88}$$

$$b_{\rm e} = -2.25 - 4.02\,z + 0.318\,z^2 - 14.6\,z^3\,. \tag{3.89}$$

- Euclid-like Hα survey:

$$N_{\rm g} = z^{1.985} \exp\left(0.019\,z^4 - 0.052\,z^3 + 0.147\,z^2 - 3.405\,z + 11.471\right), \tag{3.90}$$

$$b = 0.7(1+z)\,, \tag{3.91}$$

$$s = 0.234 + 0.801\,z - 0.222\,z^2 + 0.015\,z^3\,, \tag{3.92}$$

$$b_{\rm e} = -7.29 + 0.470\,z + 1.17\,z^2 - 0.290\,z^3\,. \tag{3.93}$$

- HI intensity mapping (any survey):

$$T_{\rm HI} = 0.0559 + 0.2324\,z - 0.0241\,z^2 \ \ {\rm mK}\,, \tag{3.94}$$

$$b = 0.667 + 0.178\,z + 0.050\,z^2\,, \tag{3.95}$$

$$s = 0.4\,, \tag{3.96}$$

$$b_{\rm e} = -0.32 - 0.11\,z + 0.06\,z^2 - \exp\left(-0.9\,z^3 + 3.12\,z^2 - 4.61\,z + 0.78\right). \tag{3.97}$$

The fits are illustrated in Figure 3.14. The evolution bias can be positive (more galaxies in a comoving volume than the conserved case) or negative (less galaxies) and it can change sign. Note that the evolution of sources in intensity mapping is less susceptible to galaxy mergers as compared to the number counts in galaxy surveys, since intensity mapping does not resolve individual galaxies. The magnification bias is always positive; it is most easily computed not via a derivative, but from the ratio of the luminosity function and number density, as in (3.13).

Chapter 4

Constraining the growth rate of large-scale structure

The growth rate of large-scale structure provides a powerful consistency test of the standard cosmological model and a probe of possible deviations from general relativity. We use a Fisher Matrix analysis to anticipate the constraints on the growth index γ from future spectroscopic surveys, using the power spectrum that is observed in redshift space, i.e., the angular power spectrum. We include the cross-correlations between redshift bins, using a hybrid approximation when the total number of bins is computationally unfeasible. We forecast the constraints on the growth rate from independent next-generation spectroscopic galaxy surveys, after which we determine the improvement in precision expected by combining these surveys via the multi-tracer technique.

The following chapter is based on [1, 2], of which I am co-author and first author respectively. This chapter is structured as follows. In section 4.1 we give a brief overview about the background and utility of the work. We explain the specifics of the Fisher Matrix analysis in section 4.2, as it pertains to this chapter. We analyse the effect of redshift binning on RSD precision in section 4.3, and explain the details of the tomographic analysis. The details of combining surveys in the analysis is explained in section 4.5. Our results are presented in section 4.4 and we draw conclusions in section 4.6. The fiducial model selected for the forecasts is a concordance ΛCDM model with the Planck 2018 best-fit parameters.

4.1 Preamble

We are entering a new era in the study of the large-scale structure (LSS) of the Universe. Not only will we map the sky over larger areas, but we will also go deeper in redshift. In addition to the increasing volumes, we will probe the sky at higher precision in different frequency ranges, creating exquisite sets of complementary dark matter tracers. The cross-correlation between these tracers reduces cosmic variance, which can improve constraints [93, 149–151]. Additionally, correlations between datasets suppresses some systematics.

General relativity and its classical modifications (see e.g. the reviews [23–25, 54]) have distinctive effects on the clustering of galaxies and their peculiar velocities. Identifying the statistical effect of peculiar velocities on the distribution of matter provides a powerful test of the cosmological model and the theory of gravity. This test is based on using redshift-space distortions (RSD) to measure the LSS growth rate f (1.41) or growth index $\gamma = \ln f / \ln \Omega_{\rm m}$ (1.43). To implement this test one requires the redshift accuracy of the spectroscopic surveys. Upcoming spectroscopic surveys, in optical, near infra-red and in radio bands [95, 152–159], will have greater redshift accuracy and observe larger volumes than ever before, allowing for higher precision tests.

The standard analysis of RSD data for tests of gravity uses the spatial power spectrum $P_{\rm g}(\boldsymbol{k}, z)$ in Fourier space, which allows one to cleanly separate the RSD effect via a Legendre multipole expansion. The state-of-the-art measurement is from the extended Baryon Oscillation Spectroscopic Survey (eBOSS) Data Release 14 quasar (DR14Q) survey [160], giving $\gamma = 0.580 \pm 0.082$, which is consistent with the standard ΛCDM value $\gamma = 0.55$. Similarly, most forecasts for future surveys rely on the same analysis (e.g. [132, 149, 161]). However, the Fourier power spectrum is not without its disadvantages (see subsection 2.1.1), therefore opt to rather use the angular power spectrum. Unlike $P_{\rm g}(\boldsymbol{k}, z)$, the C_ℓ is analysed in redshift space and thus we need not consider uncertainties in the fiducial model. Furthermore, it naturally includes wide-angle and relativistic effects, as well as cross-bin correlations (details in subsection 2.1.2).

It is intuitively clear that averaging over peculiar velocities in thick redshift bins in C_ℓ will wash out the RSD signal, therefore thin bins are needed for precision measurements on RSD. As redshift bins are decreased in size, the reduced number of galaxies translates into higher shot-noise, so one might expect to reach a 'sweet spot' in bin width where the precision is optimal. This expectation is however not correct,

since it ignores the additional information that arises from the growing number of auto- and cross-correlations. We confirm that information on the growth index γ continues to increase with decreasing bin width, reaching a theoretical maximum for infinitely thin bins. In practice we need to choose a bin width that is feasible for numerical computation.

We use Fisher forecasting and marginalise over the standard cosmological parameters, in particular including the amplitude of primordial fluctuations and the dark energy equation of state parameter, as well as over the clustering bias in each bin. Modelling nonlinear RSD is beyond the scope of this work and therefore we use information only from the linear scales (see subsection 2.3.1). For our forecasts we use the growth index γ, which we assume to be constant. Although this does not allow for scale-dependence of the γ (in common with most work on the growth rate), it still delivers a consistency test of ΛCDM and standard dark energy models. A significant deviation of $\gamma = 0.55$ would indicate a breakdown of the standard model, due either to non-standard dark energy or modified gravity.

We use survey specifications that are similar to those planned for the DESI BGS, the Euclid-like Hα survey, and for the SKAO HI surveys, summarised in section 3.7. For now we use a simplified model for the DESI survey. Since the BGS is a low-redshift sample, the lensing contribution is very small and we can safely neglect κ in (2.10). Also, in BGS the magnification effect is negligible, therefore we set $s = 0$ in the Doppler term (1.50). We find that the errors on γ for a Euclid-like survey and an SKAO HI intensity mapping survey are $\sim 3\%$. We also find that an HI intensity mapping survey with the SKAO precursor MeerKAT and a DESI-like BGS survey have a similar accuracy of $\sim 5\%$. Percent-level errors from independent observations seem to be only within reach for the futuristic SKAO2 HI galaxy survey. We also show that if only auto-correlations $C_\ell(z, z)$ are used and cross-bin correlations $C_\ell(z, z')$ are neglected, then the constraints degrade by a factor of $\sim 40 - 150\%$.

Using two distinctly different dark matter tracers that sample the same underlying density field enables us to significantly reduce the effect of systematics and cosmic variance (details in section 2.2). In addition, we include the information from the remaining observed volume by adding the Fisher matrices from non-overlap regions to Fisher information from the multi-tracer. In order to do this, we must assume that one can break the sky area into independent patches- which implies that one neglects modes above the size of the patches. Due to the large tomographic matrices we break down the redshift range into independent subsurveys. All cross-bin correlations within

each subsurvey are computed, but cross-correlations between subsurveys are neglected, as explained in more detail below.

We find that the errors on γ (including Planck priors on standard cosmological parameters) from combining a high-z SKA-like HI IM and a Euclid-like Hα survey are $\sim$2.3%. The combination of DESI-like BGS and low-z SKA HI IM surveys deliver $\sim$1.6% precision. Combining all the information from high- and low-redshift surveys further improves the error on growth index to $\sim$1.3%, which is an improvement of $\sim$55% on constraints from the best independent survey.

4.2 Fisher matrix analysis

The expected precision of measurement on γ from future spectroscopic surveys was estimated using the Fisher forecast, as explained in section 2.3. In the analysis we consider the following set of parameters:

$$\vartheta_\alpha = \Big\{\gamma, A_s, n_s, \Omega_{\rm cdm}, \Omega_{\rm b}, w, H_0, b(z_i)\Big\}. \tag{4.1}$$

For the cosmological parameters we use the fiducial values: $A_s = 2.142 \times 10^{-9}$, $n_s = 0.967$, $\Omega_{\rm cdm} = 0.26$, $\Omega_{\rm b} = 0.05$, $w = -1$, $H_0 = 67.74$ km/s/Mpc. For the growth index, we take $\gamma = 0.55$, as discussed above. In addition, the clustering bias in each bin, $b(z_i)$, is a free parameter, with fiducial value set by the bias models for each survey (see section 3.7). We assumed Gaussian priors from Planck 2018 [162] for all standard cosmological parameters. The priors are on the parameters, not their logarithms; we use the log of the parameters in the Fisher matrix purely because this gives a numerically more stable inversion of the matrix (see [110] for more detail).

We marginalise over the uncertainty of linear clustering bias $b(z_i)$ as a nuisance parameter, in each redshift bin z_i. The number of bias parameters is therefore survey- and binning-dependent and is further discussed in section 4.3. As will become clear, in some experiments the number of bins introduces computational limitations, and we develop a means to deal with this, following the idea proposed in [110].

The angular power spectra and their derivatives are computed using CAMB_sources . The derivatives with respect to $\Omega_{\rm cdm}, \Omega_{\rm b}, w, H_0$ are taken numerically using the five-point stencil method. For the remaining parameters, we use a modified CAMB_sources to accept analytical derivatives[1]. The analytical derivative with respect to γ uses the

[1] https://github.com/ZeFon/CAMB_sources_MT_ZF.git

parametrisation (1.43), so that $\partial f/\partial\gamma = f \ln\Omega_{\rm m}$. Then

$$\frac{\partial}{\partial\gamma}C_\ell(z_i,z_j) = \int \mathrm{d}\ln k \Big[\Delta_\ell^W(z_j)\int \mathrm{d}z'\; p(z')\; W(z',z_i)\;\ln\Omega_{\rm m}\Delta_\ell^{\boldsymbol{v}} \tag{4.2}$$

$$+\,\Delta_\ell^W(z_i)\int \mathrm{d}z''\; p(z'')\; W(z'',z_j)\;\ln\Omega_{\rm m}\;\Delta_\ell^{\boldsymbol{v}}\Big]\;\mathcal{P}(k)\,, \tag{4.3}$$

where $\Delta_\ell^{\boldsymbol{v}}$ denotes the RSD and Doppler terms in (2.10). The analytical derivatives with respect to A_s, n_s and the biases are given in Appendix A of [94].

4.3 Redshift binning and the precision on RSD

In a Fisher Matrix analysis of the Fourier power spectrum $P_{\rm g}(\boldsymbol{k})$, the redshift bin width does not affect the analysis, provided that Δz is not too large (typically $\Delta z \lesssim 0.1$ is chosen). The important binning in the Fourier case happens in k-space. On the contrary, the bin width plays an important role in the Fisher Matrix analysis using C_ℓ, especially for spectroscopic surveys. In this case, we need to apply redshift binning in a way that corresponds to the observable of interest. For example, if we choose broad redshift bins, this will suppress the RSD signal, since the stochastic nature of peculiar motions tend to average out. We can confirm this expectation by looking at the relative strength of RSD in the angular power spectrum as the bin width is decreased. A typical example is shown in Figure 4.1 (*top left*), where we plot $C_\ell(z_i,z_i)$ without RSD (*dashed*) and with RSD (*solid*), for different bin widths Δz; the fractional RSD contribution is shown in the *bottom left* panel. The Fisher information on the growth rate index γ also increases with decreasing bin width, as shown via $\partial C_\ell/\partial\gamma$ in the *top right* plot.

It is clear from these plots that one can in principle extract more information from RSD by decreasing the width of the redshift bin. On the other hand, this also increases the shot-noise (3.72), since $N_\Omega \sim N\Delta z$ (and similarly for the instrumental noise (3.75)). The increase in shot-noise with decreasing bin width is illustrated in Figure 4.1 (bottom right).

One might expect that the battle between increasing signal and growing shot-noise produces an idealised binning configuration where information is maximised. The left panel of Figure 4.2 appears to show this, for a bin centred at redshift $z_i = 1$ in a Euclid-like Hα survey (*red*) and SKAO IM1 survey (*blue*). We vary the width of a single redshift bin and find an optimal bin size that minimises the conditional error from auto-correlations. However, the problem with this apparent optimisation is that

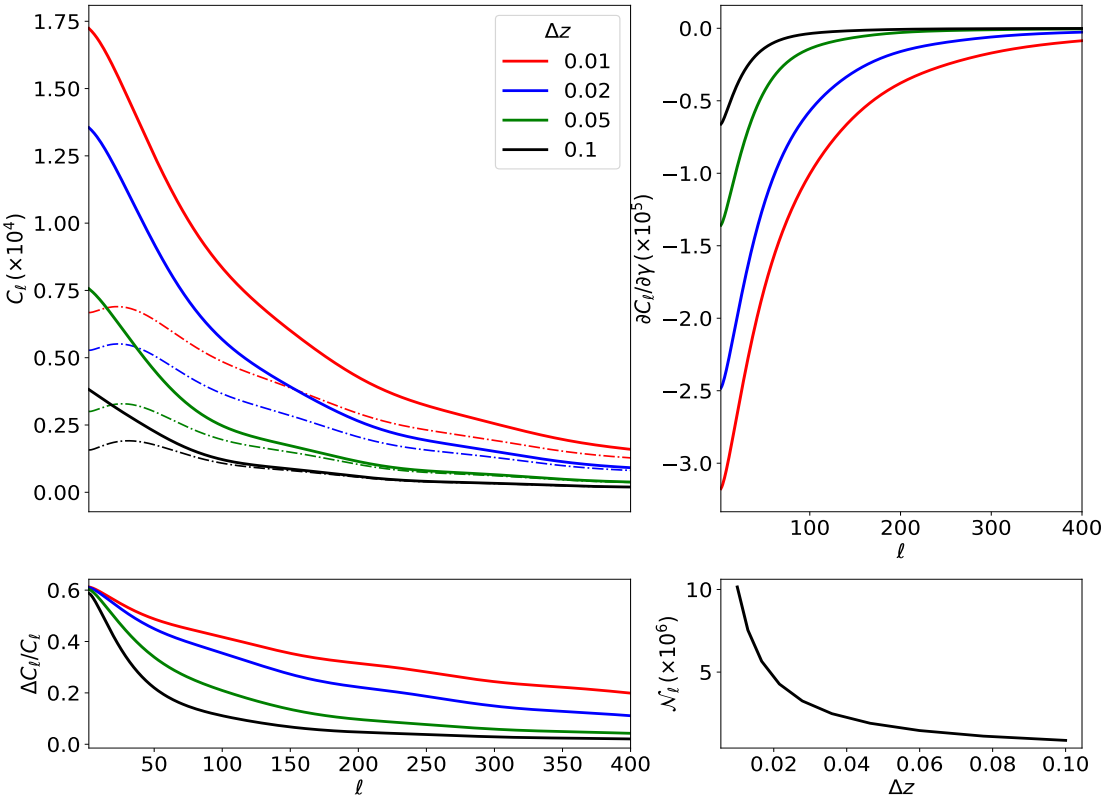

Fig. 4.1 *Top left:* $C_\ell(z_i, z_i)$ without RSD (*dashed*) and with RSD (*solid*). *Bottom left:* fractional RSD contribution to total angular power spectrum, where $\Delta C_\ell = C_\ell(\text{total}) - C_\ell(\text{density only})$. *Top right:* Fisher derivative $\partial C_\ell/\partial\gamma$. *Bottom right:* shot-noise (3.72). For a Euclid-like survey, with different bin widths at $z_i = 1$.

we have neglected *cross-correlations*. Decreasing the bin width means an increase in the number of bins, and consequently an even greater increase in the number of auto- and cross-spectra amongst the redshift bins. The additional information from these correlations compensates for the increased shot-noise per bin, as illustrated in the right panel of Figure 4.2. We fix the total redshift range to 0.1, subdivide it into 50 bins of $\Delta z = 0.002$, 20 bins of $\Delta z = 0.005$, 10 bins with $\Delta z = 0.01$, 5 bins with $\Delta z = 0.02$, 2 bins with $\Delta z = 0.05$ and a single bin with $\Delta z = 0.1$. Then we compute the conditional constraints on γ including cross-correlations between redshift bins. The 'sweet spot' for Euclid (and SKAO IM1) at $\Delta z \sim 0.005$ (0.01) in the left panel is not present once the cross-correlations are included. Therefore we can in principle reduce the bin size down to the size of the receiver bands, which is $\sim 2 \times 10^{-3}$ (2×10^{-4}) at $z_i = 1$[2].

[2] [119] shows that bin widths $\Delta z \lesssim 10^{-3}$ introduce non-linear systematics into the large scale modes.

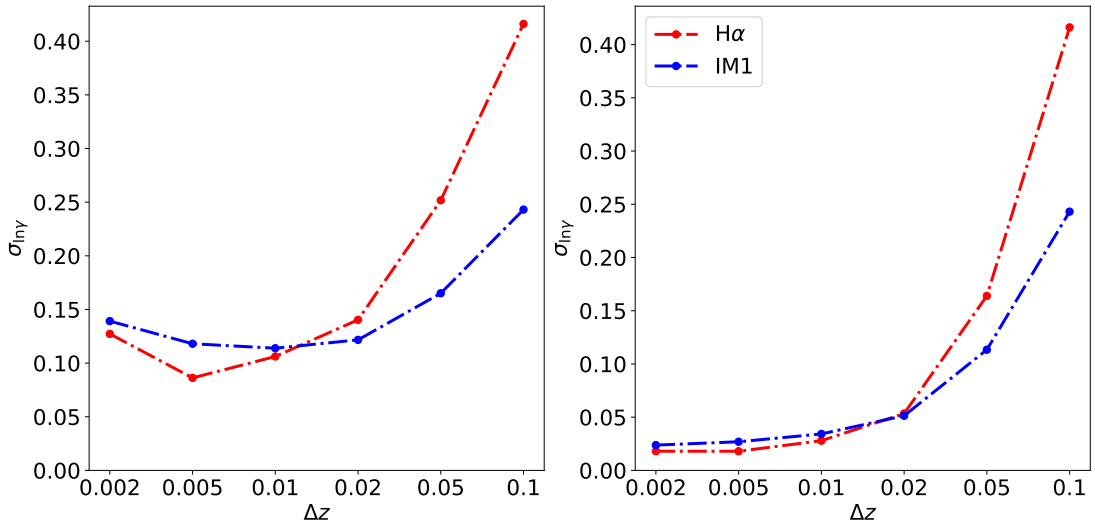

Fig. 4.2 Dependence of the conditional γ error on the redshift bin width: for a single bin of varying width (*left*); for a growing number of sub-divisions with fixed total size of 0.1, including all auto- and cross-correlations (*right*).

The implication is that we should choose a redshift bin width that is as small as possible, given the practical constraints imposed by redshift resolution and especially by numerical computation. In order to extract all the information, we need to include cross-correlations between bins – and this becomes numerically prohibitive for very large numbers of bins. To tackle this problem, we follow the 'hybrid' method proposed in [110] - i.e., we divide the full redshift range of a survey into subsurveys and perform all cross-bin correlations in each subsurvey, but not between subsurvey bins. There is a small loss of information from neglecting some cross-correlations between redshift bins. However, if the subsurveys are wide enough, i.e., bigger than the correlation length (which is typically ~ 0.1 in redshift), this loss is only non-negligible for adjacent bins of subsurveys [110]. We use a redshift bin-width of $\Delta z = 0.01$, which is numerically feasible with the hybrid method and also reduces the effect on non-linearities on low-ℓ modes [119] (see subsection 2.3.1).

In the hybrid approach, the constraints from a survey are just the summed constraints from each subsurvey. We modify this slightly in order to deal with the survey-dependence of the clustering bias. We marginalise over the bias parameters $b(z_i)$ in the Fisher matrices for each subsurvey, before adding these matrices to obtain the Fisher matrix of the full survey. In more detail: let ${}^I\tilde{F}_{\varphi_\alpha\varphi_\beta}$ be the Fisher matrix of subsurvey I marginalised over the clustering bias, so that φ_α are all the parameters in

(4.1) except for $b^I(z_i)$. Then

$$ {}^I\tilde{F}_{\varphi_\alpha\varphi_\beta} = \left[\left({}^I F_{\vartheta_\alpha\vartheta_\beta}\right)^{-1}_{\varphi_\alpha\varphi_\beta}\right]^{-1} , \tag{4.4}$$

and the total Fisher matrix is

$$ \tilde{F}_{\varphi_\alpha\varphi_\beta} = \sum_I {}^I\tilde{F}_{\varphi_\alpha\varphi_\beta} . \tag{4.5}$$

In the case of the low-redshift surveys BGS, SKAO IM2, SKAO Gal, and Lband of MeerKAT IM, the number of bins is low enough compute the full tomographic result. We compared this with the result from the subsurvey approximation with 2 subsurveys, and found that the subsurvey approximation is only slightly worse, at the second significant figure.

4.4 Forecast results

The best forecasts (including Planck 2018 priors) are in the range $\sim 3-5\%$ for the near-future surveys. This is only improved to percent level in the more futuristic HI galaxy survey with SKAO2. The constraints on γ are degenerate with the total matter density today by (1.43), as illustrated in the contour plots for γ and $\Omega_{\rm m0}$ in Figure 4.3. Note that since $\Omega_{\rm m0} = \Omega_{\rm cdm0} + \Omega_{\rm b0}$, we had to transform our Fisher matrix adding the constrains from both parameters (see [163]). We summarise the errors on γ in Table 4.1.

Including cross-bin correlations

Performing all cross-bin correlations is a computational challenge, which becomes increasingly difficult considering the very thin bins in our analysis. However, including cross-bin contributions is very important to maximally extract the information from the C_ℓ, as illustrated in Figure 4.2. In Table 4.2 we show the constraints computed when neglecting all cross-bin correlations and using only auto-correlations. By comparing with Table 4.1, we find that the marginal constraints with priors are degraded by a factor of $\sim 40-150\%$, and those without priors are degraded by much more.

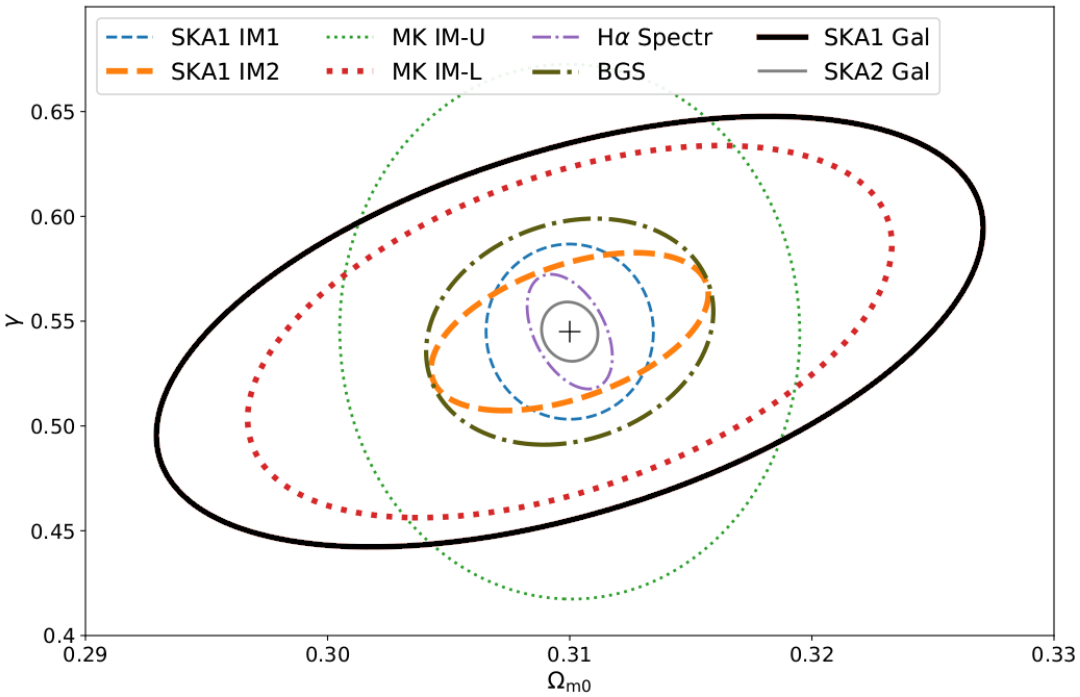

Fig. 4.3 Marginal 1σ contour plots of γ and Ω_{m0} for the surveys considered. Plus sign indicates the fiducial values. No priors included.

Table 4.1 Errors on γ in spectroscopic surveys, with and without Planck 2018 priors. Note that the last subsurvey may have a different number of bins as it is just the remainder.

Redshift	Survey	Subsurveys #	Subsurveys # bins each	$\sigma^{\text{cond}}_{\ln\gamma}$ %	$\sigma_{\ln\gamma}$ no prior %	$\sigma_{\ln\gamma}$ with prior %
Low redshift	BGS	1	50	2.6	6.7	4.5
	SKAO Gal	1	48	3.6	14.0	6.4
	MK IM-L	1	48	2.9	10.8	5.7
	SKAO IM2	1	48	1.2	4.6	2.8
High redshift	Hα Spectr	3	45	1.4	3.9	2.9
	MK IM-U	2	52	2.9	17.8	8.0
	SKAO IM1	5	45	1.2	5.3	3.7
Low and high	SKAO2 Gal	4	47	0.6	1.7	1.4

4.5 Combining multiple surveys

A natural extension to improve the constraints in section 4.4 is to combine different surveys and take advantage of the cross-correlations between tracers to improve the

Table 4.2 As in Table 4.1, but *neglecting* all cross-bin correlations.

Redshift	Survey	$\sigma^{\rm cond}_{\ln\gamma}$	$\sigma_{\ln\gamma}$	
			no prior	with prior
		%	%	%
Low redshift	BGS	3.6	26.1	8.4
	SKAO Gal	4.4	62.0	9.8
	MK IM-L	3.3	65.2	9.1
	SKAO IM2	1.4	27.4	5.1
High redshift	Hα Spectr	1.7	14.6	7.2
	MK IM-U	3.2	124.2	11.0
	SKAO IM1	1.3	26.7	6.4
Low and high	SKAO2 Gal	0.7	4.9	3.4

statistical power. Each survey scans a particular sky area and redshift range, which do not necessarily overlap with another survey. A first approach is to combine surveys via a joint analysis. This is a good approach when we consider different cosmological probes, for example, joining the information from SNIa supernovae and from the CMB. When we consider different galaxy surveys, we can no longer do joint analysis at the posterior level.

A possible approach is the multi-tracer technique [26], which we apply to the overlapping volume of the surveys, i.e., the same redshift range and sky area. This method was applied in [91, 92], using the angular power spectra, to constrain local-type primordial non-Gaussianity, leading to significant improvements over single-tracer constraints as a result of the suppression of cosmic variance. Primordial non-Gaussianity in the power spectrum is an ultra-large scale effect and is therefore heavily impacted by cosmic variance. As a consequence, a smaller overlap volume still produces better results than a simple combination (neglecting the cross-tracer correlations) of the full larger volume of each individual tracer. Since RSD measurements do not rely on ultra-large scales, the gain from the multi-tracer is lower and we benefit from combining information from non-overlap volumes with the multi-tracer information.

By following the hybrid method, we apply two techniques in order to achieve manageable numerical computations when redshift bin widths are $\sim$0.01, giving $O(100)$ bins and the same number of bias nuisance parameters.

The MT is generalised for N number of surveys in (2.13) to find the internal covariance of experiments with multiple probes, for example [4, 5, 97, 164]. However, here we are only considering a combination of two dark matter tracers A and B, with the same sky area Ω_{AB}, the same redshift range and the same redshift binning, by

using the combined matrix [91, 92]:

$$\boldsymbol{C}_\ell = \begin{bmatrix} C_\ell^{AA}(z_i, z_j) & C_\ell^{AB}(z_i, z_j) \\ \\ C_\ell^{BA}(z_i, z_j) & C_\ell^{BB}(z_i, z_j) \end{bmatrix}, \tag{4.6}$$

in (2.15). Similarly to the single-tracer case, we apply the subsurvey division of the common redshift range, marginalise out the bias parameters $b^A(z_i)$ and $b^B(z_i)$ (4.4), and add the subsurvey matrices (4.5) to produce a multi-tracer Fisher matrix $F_{\alpha\beta}^{AB}(\text{overlap})$ on the overlap volume, computed using (4.6) in (2.15).

In general, surveys A and B will not have the same sky area and the same redshift ranges. In this case, there is additional information in the non-overlap volumes of the two surveys A and B. These non-overlap volumes in general include two contributions:

- the non-overlap parts of each sky area, $\Omega_A - \Omega_{AB}$ and $\Omega_B - \Omega_{AB}$, across the full redshift range for each survey, $z_{\text{max}}^A - z_{\text{min}}^A$ and $z_{\text{max}}^B - z_{\text{min}}^B$;
- the overlap sky area Ω_{AB}, across the non-overlap parts of the redshift ranges.

The non-overlap volumes are processed in the same way as above: divide into subsurveys, marginalise out the bias parameters, and add the subsurvey Fisher matrices. This produces two non-overlap Fisher matrices, $F_{\alpha\beta}^A(\text{non-overlap})$ and $F_{\alpha\beta}^B(\text{non-overlap})$, which are then added to the overlap multi-tracer Fisher matrix to produce the total Fisher matrix:

$$F_{\alpha\beta}(\text{total}) = F_{\alpha\beta}^{AB}(\text{overlap}) + F_{\alpha\beta}^A(\text{non-overlap}) + F_{\alpha\beta}^B(\text{non-overlap})\,. \tag{4.7}$$

The volumes of the next-generation spectroscopic surveys are given in Table 3.3, which indicates that there are significant overlaps in the low- and high-redshift ranges. This suggests a multi-tracer combination of IM2 with BGS and another of IM1 with Hα would be feasible. We assume the overlapping sky area between surveys is $\Omega_{AB} = 10^4\,\text{deg}^2$ for both low- and high-z combinations, which then gives the non-overlap areas, $\Omega_A - \Omega_{AB}$ and $\Omega_B - \Omega_{AB}$. These regions are summarised in Table 4.3.

For the low redshift combination there is a good overlap in the redshift range, but for the high redshift case IM1 extends well beyond the Hα range. In practice above $z = 1.8$ and below $z = 0.9$ we only obtain constraints from HI IM, although we still add this information to the overall constraints as in (4.7). We fix the subsurveys to have 20 redshift bins of width 0.01. Note that subsurveys at the edges of the redshift range may have less than 20 redshift bins.

Table 4.3 Overlap and non-overlap sky areas for the low- and high-z combinations.

	Tracer A	Tracer B	$\Omega_A - \Omega_{AB}$ $[10^3\,\mathrm{deg}^2]$	$\Omega_B - \Omega_{AB}$ $[10^3\,\mathrm{deg}^2]$	Ω_{AB} $[10^3\,\mathrm{deg}^2]$
Low-z	SKAO IM2	BGS	10	5	10
High-z	SKAO IM1	Hα	10	5	10

The noise matrix is given by the shot-noise for galaxy counts (3.72) and instrumental noise for IM (3.75). We fix the HI IM instrumental noise by fixing the scanning ratio, i.e, the sky area over time. This implies that the observational time t_{tot}, has to be adjusted proportionally to the reduction in sky area. The shot noise for IM is much smaller than the instrumental noise and the cross shot-noise is negligible [92], as shown in subsection 3.6.3. Therefore, the noise matrix in (2.15) is simply the diagonal matrix (3.85).

The new results are for the combined totals of surveys, i.e., using multi-tracer in the overlap volume and adding single-tracer in the non-overlap volumes. As expected, the combination at low redshift has more constraining power than the one at high redshift, given that f and Ω_{m} are tending to 1 at higher redshifts.

Table 4.4 summarises our results. The single-tracer errors compare well with our previous results Table 4.1, except for the Hα sample, whose specifications we have updated following the Euclid collaboration paper [125], which appeared after the publication of our paper [1] on the ST case. There is a minor difference for the other surveys, since in order to compensate for the increased number of bias parameters in the MT we used narrower subsurveys than before. Therefore the reduced cross-bin correlations simplified the computation but slightly degraded the constraints. We excluded constraints from the SKAO Gal, since the larger observed volume of intensity mapping delivers much higher precision (see Table 4.1). We also did not consider the SKAO2 Gal configuration, because it will not be taking measurements for decades.

In Figure 4.4 we plot the 1σ contours for the low-z (*left*) and high-z (*right*) surveys as well as their combinations. By combining surveys and utilising the full observed volume, we find better results than the best single-tracer survey result. It is therefore natural to extend the combination by a further step – adding the combined totals from low and high redshift, assuming that they too are independent. There is a caveat: in order to avoid double-counting of the IM signal, we remove from the high-z combination the contribution with $z < 0.6$. We choose to exclude the information from SKAO IM1 since the instrumental noise is larger in this band and extracts less information on γ.

Table 4.4 Normalised errors on γ. The combination of surveys ($\otimes$) includes the MT applied to overlapping volumes and ST from non-overlapping volumes added via (4.7). We also consider adding the low- and high-z surveys by adding their Fisher information matrices ($\oplus$).

	Survey	$\sigma_{\ln\gamma}$ (%)
Low redshift	BGS	4.7
	SKAO IM2	2.9
	IM2$\otimes$BGS	1.6
High redshift	Hα survey	4.0
	SKAO IM1	3.8
	IM1$\otimes$Hα	2.3
Low + High redshift	IM2$\otimes$BGS$\oplus$IM1$\otimes$Hα	1.3

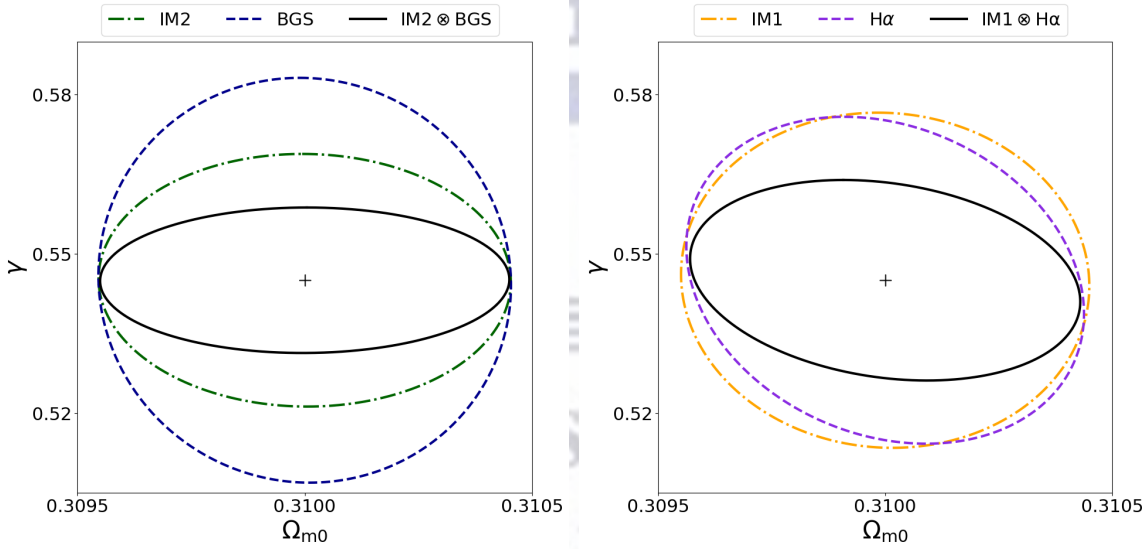

Fig. 4.4 Marginal 1σ contours for matter density and growth index: low-z surveys (*left*); high-z surveys (*right*). Solid black contours denote the combined total, as in (4.7), and + indicates fiducial values.

The result is given in the last row of Table 4.4 ($\sigma_\gamma/\gamma = 1.3\%$) and Figure 4.5 displays the 1σ contours. Despite the higher instrumental noise of SKAO IM1, it observes larger volumes and constrains the density parameter the best, thereby selecting SKAO IM2 for the $z < 0.6$ interval in the total combination slightly degrades the constraints on Ω_{m0}[3].

[3]Note that the solid black contour in Figure 4.5 is not exactly the combination of the red dot-dashed and blue dashed contours, since we removed some IM1 bins to avoid double-counting.

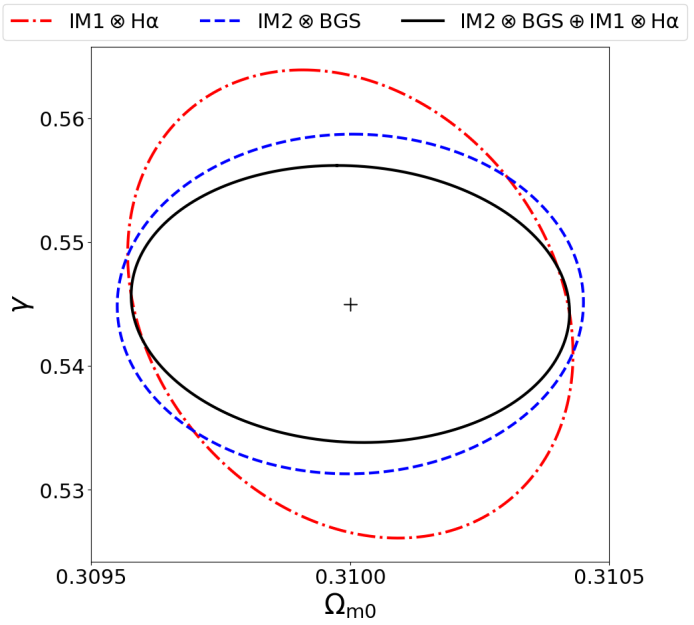

Fig. 4.5 Marginal 1σ contour plots for the low- and high-z combined totals (*solid black*).

Without information in non-overlap volumes

At higher redshift we find that there is still substantial information outside the overlap volume of IM1 and Hα surveys. We repeat our forecasts in the traditional multi-tracer analysis where one only considers the overlap volume. For the low-z combination the degradation in precision is not strong, but for the high-z case the overlap volume alone is not even competitive with the single tracer constraints. We reproduce Table 4.4 by only considering the overlap volume, see Table 4.5. In both cases, the overlap area is the same, $10^4\,\mathrm{deg}^2$. The overlap redshift range is $0.1 \leq z \leq 0.58$ for the low-z combination and $0.9 \leq z \leq 1.8$ for the high-z combination. At low redshifts, one could in principle use only the overlap area and still obtain a good constraint on γ. At higher redshifts, this is not the case, as most of the information to constrain γ comes from the large non-overlap volume.

4.6 Discussion and conclusions

In this chapter, we focused on constraints on the growth index γ using the observed power spectrum, i.e. the angular power spectrum C_ℓ, of spectroscopic cosmological surveys. Instead of an exhaustive study of surveys, we tried to fill the redshift range $0 < z \lesssim 3$ with the potentially best contemporaneous spectroscopic surveys. We first

Table 4.5 As in Table 4.4, but considering only the overlap volumes of low- and high-z combinations.

	Survey	$\sigma_{\ln\gamma}$ (%)
Low redshift	BGS	5.5
	SKAO IM2	3.8
	IM2⊗BGS	1.9
High redshift	Hα survey	4.6
	SKAO IM1	12.9
	IM1⊗Hα	4.2

investigated the effect of redshift bin width on the amount of information on γ that can be extracted. Unlike the case of the Fourier power spectrum $P_{\rm g}$, the choice of redshift bin width has a significant impact in the angular power spectrum. We showed that cross-correlations between bins compensates for the growth in noise, and we concluded that in theory, the thinnest possible width will deliver the highest signal-to-noise. In practice, computing all cross-bin correlations becomes increasingly difficult for the very thin bins. We used a variant of a 'hybrid' method to capture the dominant cross-correlation contribution, where the full range of auto- and cross-bin correlations are computed only within each subsurvey.

We used the growth index γ rather than the growth rate f, since it is redshift-independent and therefore better suited to surveys with very high numbers of redshift bins. Although the γ parametrisation is not valid for scale-dependent modifications of gravity, it still provides a test of the standard cosmological model and a probe of possible deviations from general relativity.

Key advantages of C_ℓ include: it incorporates the redshift evolution of all cosmological, astrophysical and noise variables; it does not impose a flat-sky approximation but naturally incorporates wide-angle correlations; Doppler and lensing corrections to the two-point correlations are also naturally included. Furthermore, since the angular power spectrum is directly observable, constructing the C_ℓ of the data requires no assumptions of a fiducial model and therefore no Alcock-Paczynski correction is needed. These advantages over the Fourier power spectrum $P_{\rm g}$ (which is not an observable) come with a price. Unlike $P_{\rm g}$, C_ℓ does not allow a clean separation of the RSD effect.

In our Fisher forecasts, we marginalised over the standard cosmological parameters, as well as the dark energy equation of state and the clustering bias in each redshift bin for each survey. Our constraints are based only on the information from linear

scales. Our main results for independent surveys are shown in Table 4.1 and in the error contour plots of Figure 4.3. The best marginal constraints (including priors) on γ are $\sim 3-5\%$ for the near-future surveys, with SKAO intensity mapping providing the best near-future constraints, while the SKAO precursor MeerKAT is predicted to be competitive. The more futuristic SKAO2 HI galaxy survey would be necessary to reach sub-percent errors from a single cosmological survey.

In addition, we included all possible information from these surveys, using multi-tracer cross-correlations on overlap volumes and single-tracer correlations on non-overlap volumes. To do this we assumed that different patches of the sky are independent and we only included modes that are contained within each patch.

Our main MT results are shown in Table 4.4 and in the contour plots of Figure 4.4 and Figure 4.5. The best marginal constraints on γ are $\sim$1.6 and $\sim$2.3% for combinations of low- and high-z surveys respectively. Therefore, we find $\sim$45% improvement on the best independent survey. If we take the further step of combining the low- and high-z combinations, we find a precision of 1.3%, which is $\sim$55% better than the best single-tracer. The combination of the low- and high-z surveys renders a similar precision to that of the futuristic SKAO2 galaxy survey.

In conclusion, combining the information from appropriate near-future spectroscopic surveys – via the multi-tracer technique in the overlap volumes and the single-tracer in non-overlap volumes – will significantly improve constraints of the growth rate of the large-scale structure, without using more observational resources. In addition, joining the information from low and high redshifts can break the degeneracy between $\Omega_{\rm m0}$ and γ.

Chapter 5

Future prospects for $f_{\rm NL}$ and relativistic effects

Measuring the effects of primordial non-Gaussianity in the large-scale structure is an important scientific driver of future surveys as their volume increases. Primordial non-Gaussianity of the different types (local, equilateral, folded) are only observable on ultra-large scales, and provides an exquisite window into the physics of the very early universe (see e.g. [22] for a review). We study combinations of future large-scale structure surveys in optical/NIR and radio bands, in order to forecast how well we will be able to constrain $f_{\rm NL}$ (1.36). We also estimate the amount of information we will be able to extract on light-cone effects (i.e. relativistic effects) from future surveys, which can serve as a novel test for gravitational models. In addition, the relativistic effects can mimic a signal similar to $f_{\rm NL}$ and potentially bias its measurement. We also consider the influence that neglecting the light-cone effects has on parameter measurements.

The chapter is based on [4, 5], of which I am first author. It is organised as follows: in section 5.2 we focus on local primordial non-Gaussianity, Doppler effects and lensing magnification effects in a multi-tracer analysis of the observed angular power spectra. We present our results in section 5.4 and conclude in section 5.5.

5.1 Preamble

Non-gaussianities give rise to non-zero odd-point clustering functions, and local-type primordial non-Gaussianity also affects the two-point statistics of tracers of the dark matter [165, 166]. It induces a scale-dependent correction to the bias, $\propto f_{\rm NL}H^2/k^2$

in Fourier space, thereby affecting the power spectrum on very large scales (see subsection 1.4.2). The state-of-the-art constraint on the local-type primordial non-Gaussianity parameter $f_{\rm NL}$ is provided by Planck [10]: $f_{\rm NL} = -0.9 \pm 5.1$ (at 68% CL). Several constraints have also been provided by quasar surveys [18, 167], the most recent being $f_{\rm NL} = -12 \pm 21$ [19].

Future galaxy surveys will improve on current constraints because they will access a greater number of long modes than available in current surveys [43, 47, 123, 168–172]. Measuring the scale-dependent bias (1.38) using the power spectrum on very large scales requires extremely large cosmological volumes to reduce error bars; in most cases this is not enough due to the growth of cosmic variance with scale. In fact, forecasts that are based only on the power spectrum for realistic future cosmological surveys, using the scale-dependent bias of a single tracer on its own, cannot provide a precision of $\sigma(f_{\rm NL}) < 1$. This is an important threshold to distinguish between single-field and many multi-field inflationary scenarios (see e.g. [49]). In order to beat cosmic variance and approach or break through the $\sigma(f_{\rm NL}) \sim 1$ target, one needs to take advantage of the multi-tracer technique [26, 27, 114, 173, 174], as shown in [89–98]. In section 2.2 we give an overview of the technicalities regarding the multi-tracer technique.

It is important to note that the observed power spectrum includes light-cone effects [40, 43, 101, 175] (see section 1.5), which can produce a signal similar to that of $f_{\rm NL}$, potentially leading to a bias in the measurement of $f_{\rm NL}$ [41–43, 85–88][1]. Other theoretical and systematic effects may also be degenerate with $f_{\rm NL}$ in spectroscopic surveys (see e.g. [119, 178, 179]). We include large-scale lensing magnification and all other light-cone effects, and we show that neglecting these relativistic effects in a multi-tracer analysis can bias estimates of $f_{\rm NL}$ and of the standard cosmological parameters (see also [88]). However, lensing and other relativistic effects are not simply a theoretical 'nuisance' that needs to be included in the modelling – they can also be important cosmological probes of gravity (see e.g. [60, 66, 69, 71–78, 180–182]).

One of our goals is to determine how well we could detect the Doppler term, both in single and multiple tracer cases, which requires accurate redshifts. We therefore use 'spectroscopic' to mean cosmological surveys with high redshift accuracy, irrespective of how such redshifts are effectively measured. While photometric surveys provide lower shot-noise, which is an important advantage in the multi-tracer technique, they also lose velocity information via averaging over thick redshift bins. We consider surveys with specifications similar to the following planned surveys: the DESI-like Bright Galaxy Sample [183]; the Euclid-like Hα survey [125]; the 21cm intensity mapping

[1] This is also the case for the bispectrum [48, 148, 176, 177].

surveys in Bands 1 and 2 with the MID telescope of the SKAO [95]. The details of modelling these surveys are found in chapter 3, the fits used in the forecasts are given in subsection 3.7.1, and the survey specifications can be found in Table 3.3. In the multi-tracer we only consider the overlapping sky area of the surveys, which in this case is $\Omega_{\rm sky} = 10^4\,{\rm deg}^2$ for both low- and high-z combinations. As before, we fix the scanning ratio of the SKAO IM surveys to compensate for the reduction in sky area. In this analysis we include all cross-bin correlations by performing the full tomographic analysis.

The multi-wavelength choice of the four surveys is motivated by: a good coverage of redshifts in the range $0 < z < 2$; high redshift resolution in order to detect the Doppler effect; a negligible cross-shot noise between optical and 21cm intensity samples; and the very different systematics affecting optical and radio surveys, which are suppressed in cross-correlations.

We show that combining these surveys can provide a detection of the Doppler term with a signal-to-noise of ∼8. In the case of the lensing magnification contribution, the Hα survey on its own can deliver a 4% error, while the full combination improves this to 2%. For $f_{\rm NL}$, the forecast multi-tracer constraint significantly improves on Planck, at $\sigma(f_{\rm NL}) \sim 1.5$, but falls short of the $\sigma(f_{\rm NL}) \sim 1$ threshold. This is not unexpected, since our choice of surveys is based on the combination of relativistic and primordial non-Gaussian signals and is not optimised for $f_{\rm NL}$ alone. As an example, photometric surveys or radio continuum surveys in a multi-tracer combination [91] are more likely to achieve $\sigma(f_{\rm NL}) < 1$, as they will have lower shot noise. Similarly, combining the bispectrum and power spectrum of a single tracer [46, 184–186] can achieve $\sigma(f_{\rm NL}) < 1$, especially when using spectroscopic surveys [157, 184, 187]. Adding information from higher-order point statistics, such as the trispectra of spectroscopic surveys [188], will help reduce error bars on $f_{\rm NL}$.

We also find that the multi-tracer method approaches the maximum information that can be extracted, since the marginal errors approach the conditional errors.

5.2 Primordial non-Gaussianity and relativistic effects in the multi-tracer

The scale-dependent clustering bias in Fourier space, given by (1.38), grows on large scales as $f_{\rm NL}H_0^2/k^2$, producing a power spectrum monopole $P_{\rm g}(\boldsymbol{k}, z)$ that blows up on ultra-large scales. This behaviour in Fourier space is misleading, since the directly measurable signal of $f_{\rm NL}$ is very small. The point here is that the Fourier power

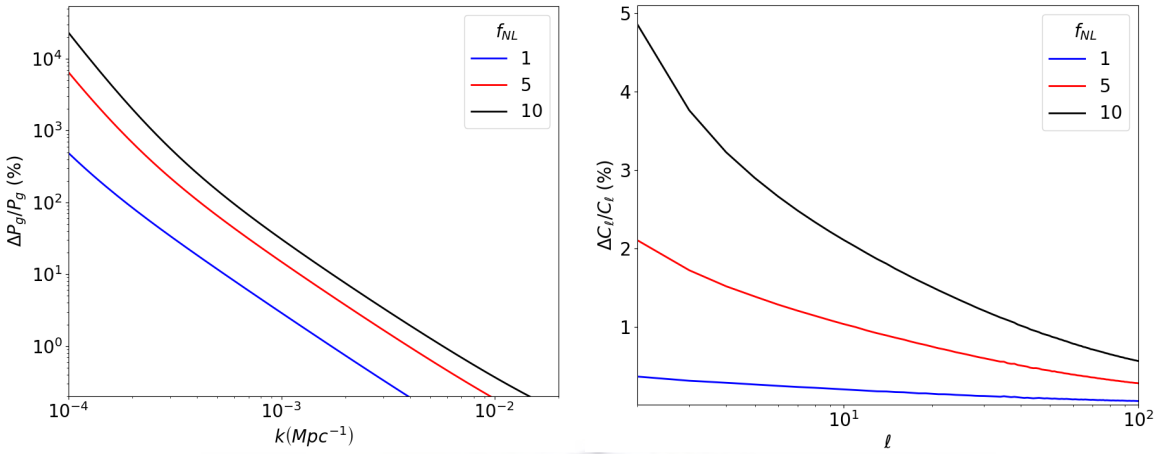

Fig. 5.1 Percentage contribution of the scale-dependent bias to the Fourier power spectrum monopole (*left*) and angular power spectrum (*right*) for an Hα survey at $z = 1.8$ with $\Delta z = 0.03$.

spectrum is not directly observable. One has to de-project measured angular positions and redshifts into a Cartesian three-dimensional volume – which requires assuming a fiducial cosmology. The Fourier power spectrum is a derived quantity, which is also not gauge invariant. By contrast, the angular power spectrum (see subsection 2.1.2) is observable, thus circumvents the requirement of an Alcock-Paczynski correction.

We illustrate this point in Figure 5.1, showing an example of the percentage contribution of $f_{\rm NL}$ to the Fourier (*left*) and angular power spectra (*right*). The blow-up in the unobservable $P_{\rm g}$ is not mirrored by the behaviour of C_ℓ, in which the $f_{\rm NL}$ contribution is only a few percent on the largest scales, where cosmic variance is typically much larger. This is why we require a multi-tracer approach to detect the signal of $f_{\rm NL}$.

The dominant relativistic effects are from the Doppler and lensing magnification terms. The Doppler term depends on both the magnification and evolution biases via (1.50), while the lensing term (1.51) depends only on the magnification bias. Using the fits in subsection 3.7.1, we show in Figure 5.2 the amplitude of the Doppler and lensing contributions to the observed number density and temperature contrasts.

It is apparent that the Doppler coefficient for intensity mapping is significantly smaller than for the galaxy samples. The magnification bias of HI IM surveys is $s^{\rm HI} = 2/5$, therefore by (1.50) we see the $1/\mathcal{H}\chi$ term is cancelled, contributing to the reduced $A_{\rm D}$. Therefore we expect HI surveys to under-perform in extracting information on the Doppler effect, compared to galaxy surveys. We also note that the

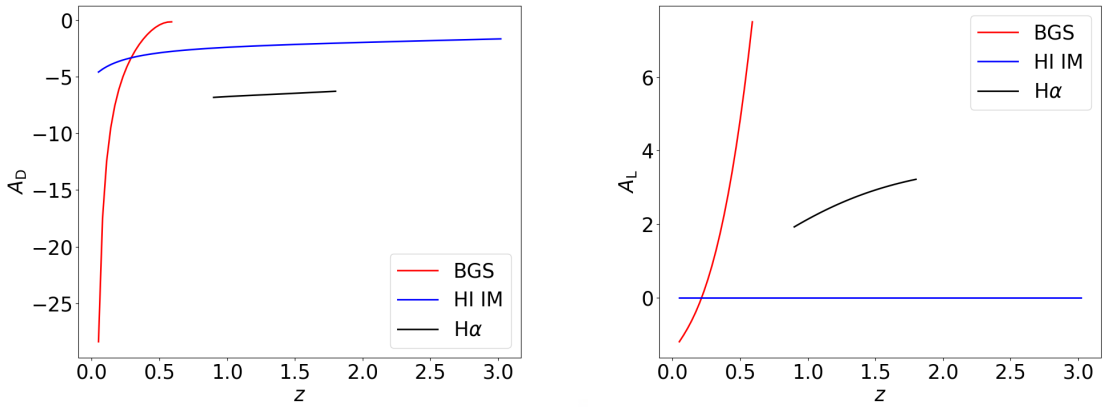

Fig. 5.2 Coefficient of the Doppler (*left*) and lensing (*right*) contributions for the surveys.

Doppler amplitude is strongest at low redshift, so that the BGS survey is best placed to detect it.

The lensing coefficient vanishes for intensity mapping and is largest for the BGS survey. This does not mean that the lensing contribution for BGS is greater than for Hα, since the lensing amplitude is $|A_{\rm L}\kappa|$ and κ will be larger at higher z.

For our Fisher Matrix analysis, we separate the relativistic contributions in (1.46) by introducing fudge factors $\varepsilon = 1$ in order to gauge the detectability of each contribution:

$$\Delta_A = \delta_A + \Delta^{\rm RSD} + \varepsilon_{\rm D}\,\Delta^{\rm Dopp} + \varepsilon_{\rm L}\,\Delta^{\rm Lens} + \varepsilon_{\rm P}\,\Delta^{\rm Pot}\,. \tag{5.1}$$

We determine which correlations add the most information to the analysis, both in single- and multi-tracer cases. We compute the signal-to-noise of a parameter ϑ, constrained by two surveys, from each correlation $C_\ell^{AB}(z_i^A, z_j^B)$, as

$$S^{AB}(\vartheta, z_i^A, z_j^B) = \left\{ \sum_\ell \left[\frac{\partial_\vartheta\, C_\ell^{AB}(z_i^A, z_j^B)}{\Delta C_\ell^{AB}(z_i^A, z_j^B)} \right]^2 \right\}^{1/2}, \tag{5.2}$$

where $A, B = 1, 2$ and

$$\Delta C_\ell^{AB}(z_i^A, z_j^B) = \left\{ \frac{\Gamma_\ell^{AA}(z_i^A, z_j^A)\Gamma_\ell^{BB}(z_i^B, z_j^B) + \left[\Gamma_\ell^{AB}(z_i^A, z_j^B)\right]^2}{(2\ell+1) f_{\rm sky}} \right\}^{1/2}, \tag{5.3}$$

with

$$\Gamma_\ell^{AB} = C_\ell^{AB} + \mathcal{N}_\ell^{AB}\,, \tag{5.4}$$

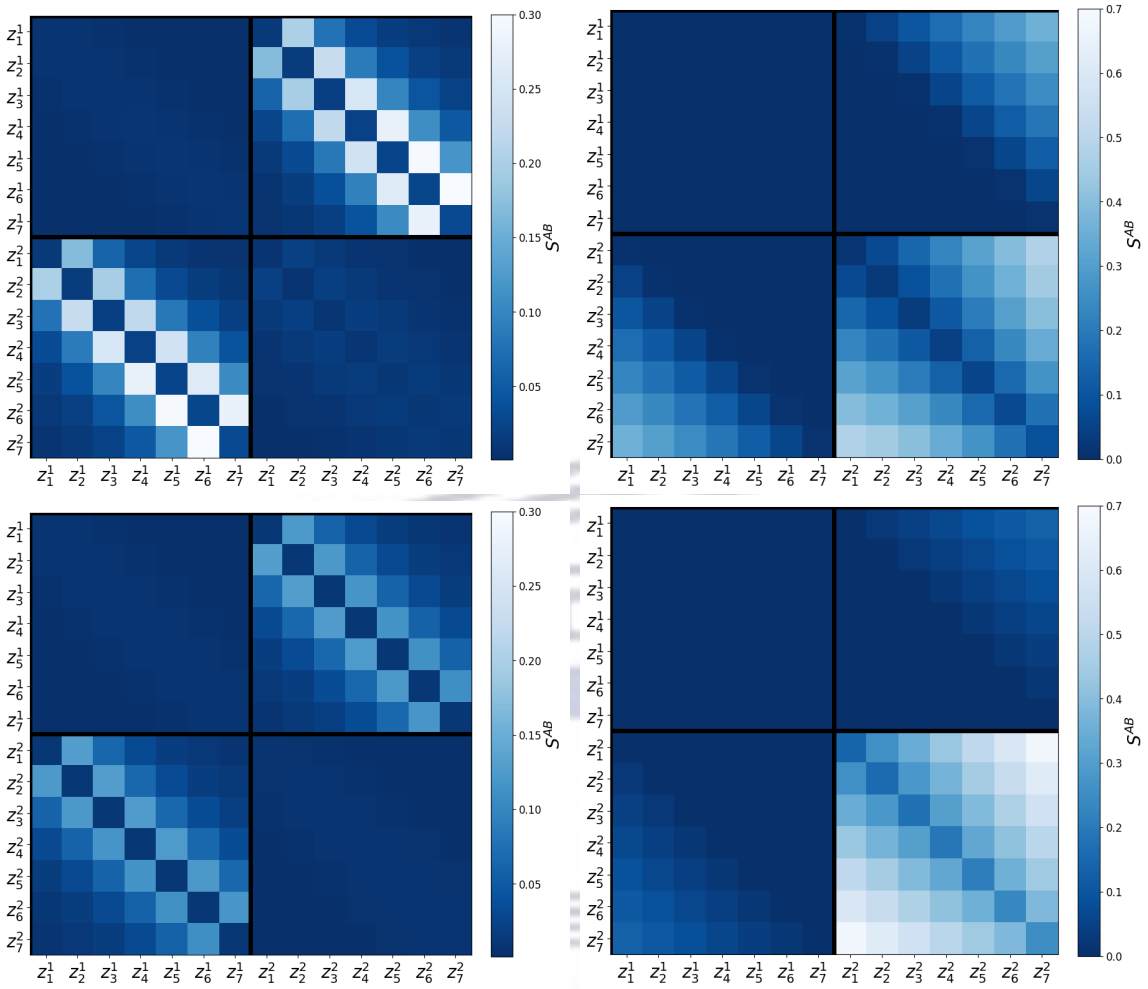

Fig. 5.3 Signal-to-noise $S^{AB}(\theta, z_i^A, z_j^B)$ for the Doppler contribution ($\theta = \varepsilon_{\rm D}$) (*left*) and the lensing magnification contribution ($\theta = \varepsilon_{\rm L}$) (*right*). *Top panels:* $1 \otimes 2 = {\rm IM2} \otimes {\rm BGS}$ for $0.35 < z < 0.56$. *Bottom panels:* $1 \otimes 2 = {\rm IM1} \otimes {\rm H}\alpha$ for $0.90 < z < 1.11$. The colour bar shows the signal-to-noise ratio.

where the noise is given by (3.72) for galaxy surveys and (3.75) for IM.

As we confirm below, the potential terms are very poorly constrained, and we set $\varepsilon_{\rm P} = 0$ in this discussion. In Figure 5.3 we show examples of S^{AB} for $\vartheta = \varepsilon_{\rm D}$ (*left*) and $\vartheta = \varepsilon_{\rm L}$ (*right*) using both low-redshift (*top*) and high-redshift (*bottom*) survey pairs. The axes indicate which z-bins are correlated, where z_i^1 is the i-bin of SKAO IM2 (*top panels*) and IM1 (*bottom panels*), while z_i^2 corresponds to BGS (*top panels*) and Hα (*bottom panels*). For the multi-tracer combination $1 \otimes 2 = {\rm IM2} \otimes {\rm BGS}$ (*top panels*) we use the redshift range $0.35 < z < 0.56$, while for $1 \otimes 2 = {\rm IM1} \otimes {\rm H}\alpha$ (*bottom panels*) we use $0.9 < z < 1.11$. In both cases a bin-width $\Delta z = 0.03$ is used. The colour bar shows the signal-to-noise S^{AB} of the parameter for each pair (z_i^A, z_j^B).

The plots show that the bulk of the information on $\varepsilon_{\rm D}$ comes from the cross-spectra, which contribute 3–5 times more than the individual surveys. This contribution is mainly from the cross-tracer spectra, although at low redshift it is also marginally from cross-correlations between consecutive redshift bins of the same tracer. The latter feature is the basis of the estimator constructed in [189], which is the angular power spectrum counterpart of the Doppler dipole in the two-point correlation function [180]. Although there is some residual information in the low-redshift BGS-BGS correlations, the bulk clearly comes from the off-diagonal, i.e. the cross-tracer correlations. BGS contains the most information on the Doppler term, given the $1/\chi$ term in (1.50) (see Figure 5.2).

In the case of lensing magnification, the analysis is slightly different. Firstly, IM has no lensing magnification contribution ($A_{\rm L} = 0$). However, IM can act as a lens of background galaxies in BGS and Hα. In both cases, we see that the furthest off-diagonal cross-bin correlations are providing the most information on $\varepsilon_{\rm L}$. As expected, this comes from the lower redshift field lensing the higher redshift field. For this reason, when the higher redshift field is traced by IM, no information is obtained – as seen in the right column of Figure 5.3. We also see that most information on $\varepsilon_{\rm L}$ is obtained by galaxy surveys on their own, especially at high redshift. In fact, for the Hα survey, cross-correlations with an IM survey seem to be irrelevant for lensing. Most information lives in the furthest off-diagonal cross-bin correlations of Hα-Hα.

5.3 Fisher forecast

Having gained qualitative insights into the multi-tracer precision on $f_{\rm NL}$ and relativistic effects, we turn now to the quantitative estimate of constraints via Fisher forecasting. Later, we also consider constraints on the standard cosmological parameters. The multi-tracer Fisher matrix for the angular power spectra is defined in section 2.3, while the noise is the diagonal matrix (3.85) where we use (3.72) for galaxy surveys and (3.75) for intensity mapping.

In our forecasts we consider the set of parameters

$$\vartheta_\alpha = \left\{ f_{\rm NL},\, \varepsilon_{\rm D},\, \varepsilon_{\rm L},\, \varepsilon_{\rm P};\, \Omega_{\rm cdm},\, \Omega_{\rm b},\, w,\, n_s,\, H_0,\, A_s;\, b_A(z_i^A) \right\}. \tag{5.5}$$

As before, we assume the fiducial cosmology: $A_s = 2.142 \times 10^{-9}$, $n_s = 0.967$, $\Omega_{\rm cdm} = 0.26$, $\Omega_{\rm b} = 0.05$, $w = -1$, $H_0 = 67.74$ km/s/Mpc. Note that the ε_I do not have physical meaning; instead they are used to model the detectability of the relativistic

contributions. We also consider the uncertainty in the Gaussian clustering biases by marginalising over the bias in each redshift bin, $b_A(z_i^A)$. In the single-tracer case, the forecasts are degraded by this marginalisation, but the multi-tracer analysis is only weakly affected by marginalisation over the clustering bias, consistent with [92]. We do not marginalise over the magnification and evolution biases. Instead, we consider $\varepsilon_{\rm L}$ and $\varepsilon_{\rm D}$ as rough proxies of the uncertainties in these astrophysical parameters.

We are also interested in the effect that neglecting the light-cone contributions has on parameter estimation, and follow the method set out in subsection 2.3.2. By considering the Doppler, lensing and potential effects, the fixed subset in (5.5) is:

$$\varphi_I = \left\{\varepsilon_{\rm D},\, \varepsilon_{\rm L},\, \varepsilon_{\rm P}\right\}. \tag{5.6}$$

Neglecting the relativistic effects means setting $\hat{\varepsilon}_{\rm I} = 0$, which implies a shift from the true values of

$$\delta\varepsilon_{\rm D} = \delta\varepsilon_{\rm L} = \delta\varepsilon_{\rm P} = -1\,. \tag{5.7}$$

We then determine the bias on the best-fit values of the remaining parameters:

$$\psi_i = \left\{f_{\rm NL};\, \Omega_{\rm m0},\, w,\, n_{\rm s},\, H_0,\, A_{\rm s}\right\}. \tag{5.8}$$

This bias is best expressed as normalised by the errors $\sigma(\psi_i)$. We define the normalised biases from neglecting individual relativistic effect as

$$\delta^I\psi_i \equiv \frac{\delta\psi_i(\varphi_I)}{\sigma(\psi_i)}\,, \tag{5.9}$$

where $\delta\psi_i(\varphi_I)$ denotes the case of (2.26) when I is fixed at one value and only j is summed over. It follows that the normalised bias from all relativistic effects combined is

$$\delta^{\rm rel}\psi_i = \frac{\delta\psi_i}{\sigma(\psi_i)} \quad \text{where} \quad \delta\psi_i = \sum_I \delta\psi_i(\varphi_I)\,. \tag{5.10}$$

In general, if $|\delta^I\psi_i| < 1$, then any induced bias is smaller than the error bars and can be safely neglected. On the other hand, if $|\delta^I\psi_i| > 1$ the effect I should not be neglected in the model. Note however that the approximation made in deriving (2.26) breaks down when $|\delta^I\psi_i| > 1$. For biases above 1σ, the value of $\delta^I\psi_i$ is not reliable – it does not quantify the bias, but qualitatively it confirms that the bias is larger than the error bars. This is sufficient for our purposes.

Table 5.1 Marginal uncertainties on $f_{\rm NL}$ and relativistic effects ε_I, computed by marginalising over the standard cosmological parameters and $b_A(z_i)$ only. Results are for individual surveys and their combination using the multi-tracer technique ($\otimes$). When combining low- and high-redshift information, we also consider adding their Fisher information matrices ($\oplus$). HI intensity mapping surveys are unaffected by lensing and cannot constrain $\varepsilon_{\rm L}$. Results exclude priors.

Redshift	Survey	$\sigma(f_{\rm NL})$	$\sigma(\varepsilon_{\rm D})$	$\sigma(\varepsilon_{\rm L})$	$\sigma(\varepsilon_{\rm P})$
$0.1-0.58$	BGS	26.38	7.57	0.39	33.3
	IM2	35.74	18.07	–	228.3
	IM2$\otimes$BGS	2.12	0.14	0.13	6.86
$0.9-1.8$	Hα	9.34	9.08	0.04	10.0
$0.35-3.05$	IM1	4.72	6.29	–	10.89
$0.60-3.05$	IM1$\otimes$Hα	3.06	0.37	0.03	4.71
$0.1-3.05$	(IM2$\otimes$BGS)$\oplus$(IM1$\otimes$Hα)	1.70	0.13	0.03	3.79
	IM2$\otimes$BGS$\otimes$IM1$\otimes$Hα	1.55	0.13	0.02	3.47

5.4 Results

5.4.1 Precision on $f_{\rm NL}$ and light-cone effects

The forecast precision on $f_{\rm NL}$ and relativistic effects from future surveys is computed for individual surveys, as well as for the multi-tracer case that includes all correlations between different surveys. In Table 5.1 we show the marginal error on $f_{\rm NL}$ and ε_I, marginalised over the uncertainty of the standard cosmological parameters and the biases $b_A(z_i)$. This approach is in some sense closer to reality, since including the light-cone corrections in the transfer function is the correct model to use. The caveat is that this assumes the magnification and evolution biases are known. Later we will partly incorporate this uncertainty in the biases by including marginalisation over the ε_I, which can be seen as a 'marginalisation' over the amplitude uncertainties of the relativistic terms.

The highest precision on $f_{\rm NL}$ from an individual survey is $\sigma(f_{\rm NL}) = 4.72$ from SKAO IM1. This is not surprising since IM1 boasts the largest observed volume among the surveys. The bigger the volume, the larger the scales we observe and the more frequently we can sample correlations at scales that carry an $f_{\rm NL}$ signal (see Figure 5.1). The IM1 precision on $f_{\rm NL}$ can be improved by a factor of 3 by combining all low- and high-z surveys (IM2$\otimes$BGS$\otimes$IM1$\otimes$Hα), resulting in $\sigma(f_{\rm NL}) = 1.55$. This is significantly better than current constraints.

It is interesting to note that individually the high-z surveys constrain $f_{\rm NL}$ remarkably better than the low-z, since the volumes observed are considerably larger. Individually the low-z surveys cannot access as many correlations on large scales, and therefore being dominated by cosmic variance, cannot constrain $f_{\rm NL}$ well. However, the multi-tracer eliminates cosmic variance, which enables the low-z combination to gain access to the $f_{\rm NL}$ signal on ultra-large scales. This is a clear example of how the multi-tracer works. By cancelling cosmic variance, dark matter tracer combinations in smaller overlapping volumes can perform as well as, or better than, single tracers covering large volumes. In fact, the low-z combination IM2⊗BGS does better than its IM1⊗Hα counterpart, because of the reduced noise at lower redshift, as shown in Figure 3.13.

The best single-survey constraint on the Doppler contribution is again from the SKAO IM1 survey, with $\sigma(\varepsilon_{\rm D}) = 6.29$. This survey has the largest volume, which compensates for the small amplitude of its Doppler term (1.50). The BGS survey has the highest amplitude: its Doppler coefficient is largest (see Figure 5.2) and the radial peculiar velocity $\boldsymbol{n}\cdot\boldsymbol{v}$ is largest at low z. Nevertheless, the volume beats the amplitude for a term that has signal on ultra-large scales. As soon as we multi-trace the surveys, again the domination of survey volume fades away due to the cancellation of cosmic variance. Similar to $f_{\rm NL}$, the low-z combination outperforms the high-z combination by a factor of nearly 3 – since moving to lower z both increases $\Delta^{\rm Dopp}$ (1.49) and reduces survey noise. This effect can also be seen in Figure 5.3. The full combination of four surveys offers a precision of $\sigma(\varepsilon_{\rm D}) = 0.13$, only slightly better than the low-z combination. The multi-tracer improvement in precision over the best single tracer is a factor of nearly 50. This precision on the Doppler amplitude corresponds to a signal-to-noise of ∼8, sufficient for a detection of the Doppler term. It also suggests that we can make some constraint on the evolution bias, assuming that the magnification bias is constrained by the lensing term (see below).

HI intensity mapping is unaffected by lensing magnification and so cannot constrain the lensing term. The best single-survey constraint comes from the high-redshift Hα survey, as expected, delivering $\sigma(\varepsilon_{\rm L}) = 0.04$. This precision is about double that found in [79]. The reason is that we use updated survey specifications with a reduced redshift range. Even though IM does not constrain lensing by itself, its correlation with a galaxy survey does improve the error – since galaxies at z_i behind HI at $z_j < z_i$ are lensed by the IM, as confirmed by Figure 5.3. As a result, IM2⊗BGS improves the BGS-only lensing constraint by a factor of ~ 3, while IM1⊗Hα improves on Hα-only by ∼25%. The correlation of all four surveys improves on the Hα-only constraint by a factor of 2, with $\sigma(\varepsilon_{\rm L}) = 0.02$. This is a high enough precision to place reasonable

Table 5.2 Fully marginal uncertainties on $f_{\rm NL}$ and relativistic effects ε_I. The same as Table 5.1, except that $\sigma(f_{\rm NL})$ and each $\sigma(\varepsilon_I)$ are computed by marginalising over *all* other parameters, not just the standard cosmological parameters.

Redshift	Survey	$\sigma(f_{\rm NL})$	$\sigma(\varepsilon_{\rm D})$	$\sigma(\varepsilon_{\rm L})$	$\sigma(\varepsilon_{\rm P})$
$0.1-0.58$	BGS	45.15	8.70	0.40	60.07
	IM2	44.64	26.18	–	303.32
	IM2⊗BGS	2.71	0.14	0.13	8.87
$0.9-1.8$	Hα	30.73	26.9	0.05	15.51
$0.35-3.05$	IM1	6.77	9.52	–	21.24
$0.6-3.05$	IM1⊗Hα	4.37	0.37	0.03	6.78
$0.1-3.05$	(IM2⊗BGS)⊕(IM1⊗Hα)	1.71	0.13	0.03	3.84
	IM2⊗BGS⊗IM1⊗Hα	1.55	0.13	0.03	3.51

constraints on the magnification bias s. According to [87], we need to know $s(z)$ within $5-10\%$ accuracy to avoid systematic parameter biases.

Finally, we computed the combined uncertainty $\sigma(\varepsilon_{\rm P})$ on the relativistic potential effects (1.52). Even the full multi-tracer combination is unable to achieve $\sigma(\varepsilon_{\rm P})<1$. In other words, the potential contribution to the power spectrum is not detectable (signal-to-noise <1).

Table 5.2 presents a variation of Table 5.1 in which we include marginalisation over $f_{\rm NL}$ and the relativistic parameters ε_I. As mentioned earlier, this incorporates the uncertainties on the astrophysical parameters s and $b_{\rm e}$, in addition to the cosmological parameters. Comparing Table 5.1 with Table 5.2, we see that for individual surveys the constraints can be substantially degraded, especially for higher redshift surveys. One exception is lensing which is only slightly affected in single tracer. When we combine all four surveys, the constraints become insensitive to the additional marginalisation.

Figure 5.4 displays the contour plots for the relativistic parameters $f_{\rm NL}$ and ε_I. The covariances include marginalisation over all parameters in (5.5), as in Table 5.2. The contours show the total correlated information (*black*), with its low-z (*blue*) and high-z (*red*) components. In *green* we show constraints from the simple addition of the low-z and high-z Fisher information. This is computationally far less expensive, although some information is lost on $f_{\rm NL}$ and lensing magnification. In fact, for relativistic effects, it suffices to consider cross-tracer correlations only in the overlapping footprints.

We also find that combining low-z and high-z samples breaks degeneracies between $\varepsilon_{\rm D}$ and $\varepsilon_{\rm L}$, as well as between $\varepsilon_{\rm D}$ and $\varepsilon_{\rm P}$. As an example, the degeneracy between $f_{\rm NL}$ and $\varepsilon_{\rm L}$ (or $\varepsilon_{\rm P}$) at low-z is orthogonal to the degeneracy at high-z. This explains the

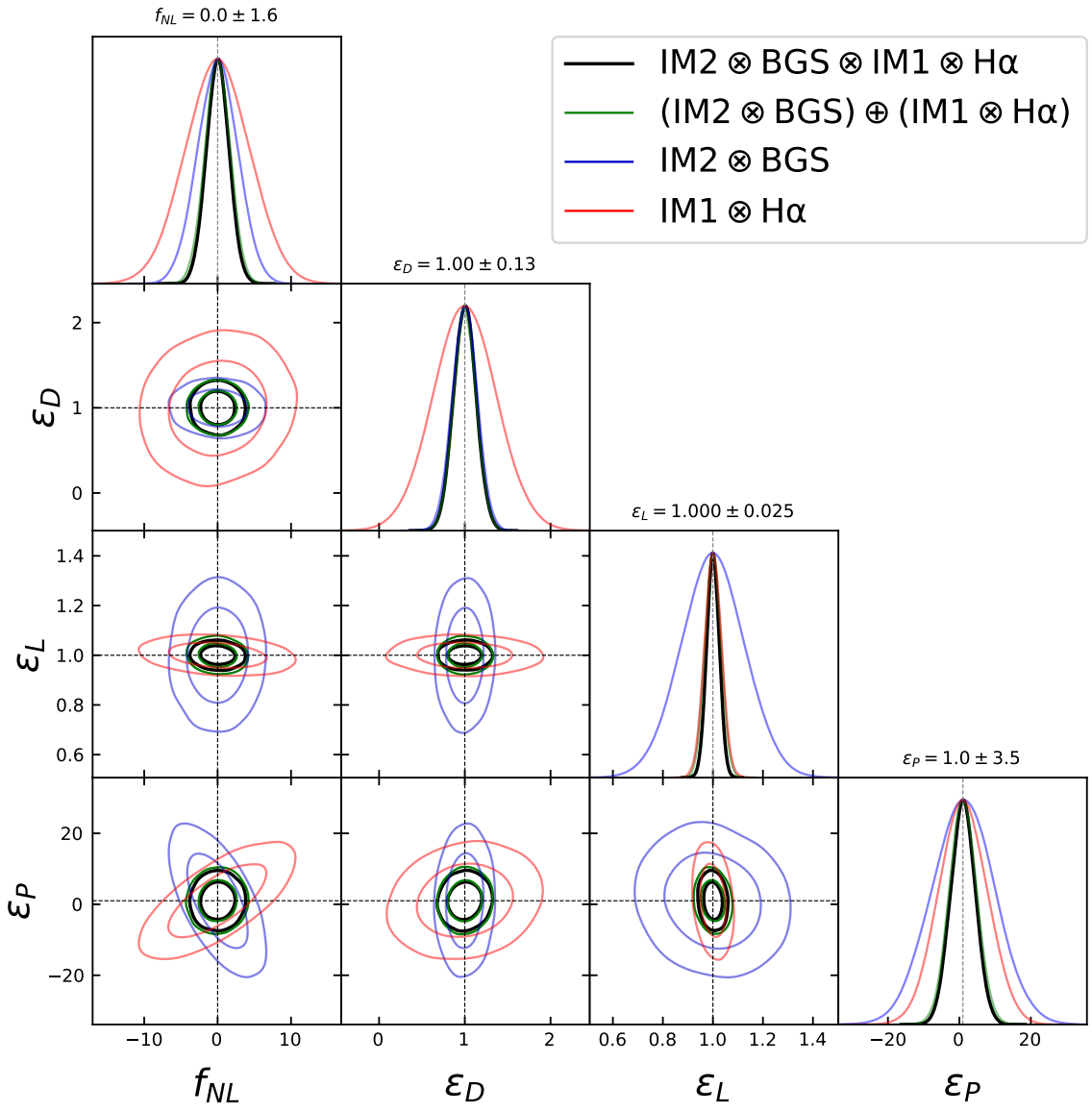

Fig. 5.4 Contour plots of $f_{\rm NL}$ and relativistic parameters. The correlation of all surveys is shown in *black*, with dotted lines giving the fiducial values. The low-z combination is shown in *blue*, high-z in *red*, and the sum of their Fisher information in *green*. Constraints exclude priors.

great improvement seen in Table 5.2 from multi-tracer pairs at low and high redshift, to the full multi-tracer combination.

In Table 5.3 we give the conditional uncertainties on $f_{\rm NL}$ and the relativistic parameters to illustrate the robustness of the multi-tracer to uncertainty in the cosmological model. Comparing Table 5.2 and Table 5.3, it is apparent that the error for single surveys is catastrophically increased by marginalising over the cosmological model,

Table 5.3 Similar to Table 5.1, except that here we display the *conditional* uncertainties on $f_{\rm NL}$ and relativistic effects ε_I.

Redshift	Survey	$\sigma(f_{\rm NL})$	$\sigma(\varepsilon_{\rm D})$	$\sigma(\varepsilon_{\rm L})$	$\sigma(\varepsilon_{\rm P})$
$0.1-0.6$	BGS	10.56	7.41	0.39	29.79
	IM2	14.17	17.17	–	173.93
	IM2⊗BGS	2.0	0.14	0.12	6.8
$0.9-1.8$	Hα	4.49	8.3	0.04	7.59
$0.35-3.05$	IM1	4.42	5.52	–	9.25
$0.6-3.05$	IM1⊗Hα	2.72	0.37	0.03	4.43
$0.1-3.05$	(IM2⊗BGS)⊕(IM1⊗Hα)	1.60	0.13	0.03	3.71
	IM2⊗BGS⊗IM1⊗Hα	1.47	0.13	0.02	3.40

especially at low z. The least affected is IM1, due to the high amount of cross-bin correlations included in the analysis. By contrast, the multi-tracer constraints are only slightly improved by not marginalising over cosmological parameters and clustering bias nuisance parameters.

Systematics

In reality, we cannot perfectly extract all the observable scales from the data – there will be a loss of ultra-large-scale modes due to systematics, e.g., extinction due to Galactic dust or stellar contamination in galaxy surveys, or foreground contamination of intensity mapping. The cosmological signal from 21cm emission is several orders of magnitude lower than the galactic and extra-galactic foreground contamination. In order to extract the cosmological information, it is therefore necessary to first remove or model the systematics in galaxy and intensity mapping surveys. Recent treatments of ultra-large scale systematics are given in [190] (galaxy survey data) and [191] (21cm intensity mapping simulations). In both cases, information is lost on the largest scales, but the loss is more severe in intensity mapping.

In [19, 190] it was found that one of the biggest complications regarding the improvement of precision on $f_{\rm NL}$ are as a result of large-scale systematics. In order to take account of the loss of some ultra-large scale signal due to systematics, we need to impose a minimum angular multipole $\ell_{\rm min}$. For a multi-tracer analysis, the same $\ell_{\rm min}$ is used for each survey. In the case of very large sky area, $\ell_{\rm min} \sim 5$ may be feasible for intensity mapping [115], thus we take this as our 'optimistic' minimum. Then we investigate how the constraints on ultra-large-scale parameters are affected by increasing $\ell_{\rm min}$.

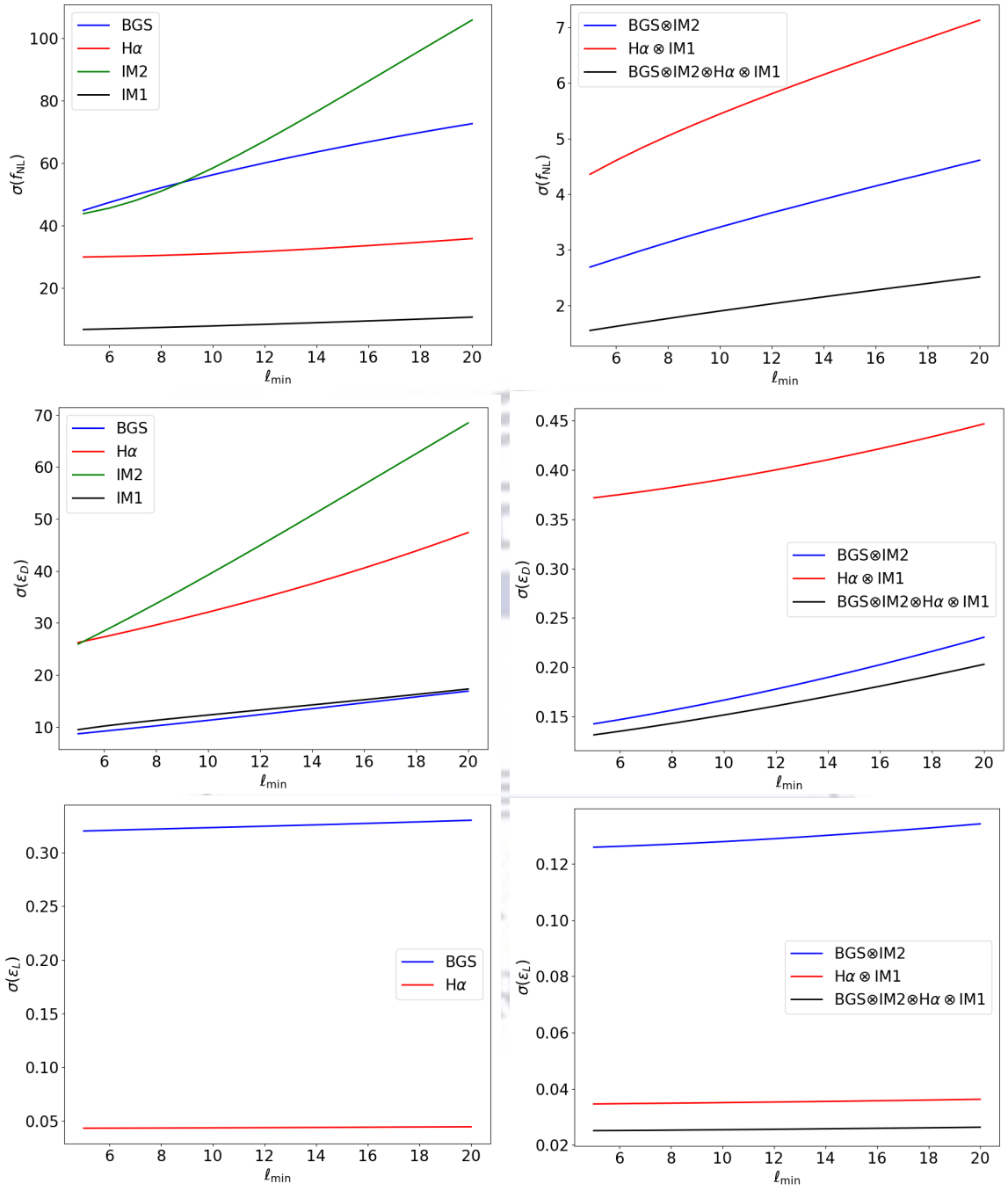

Fig. 5.5 Uncertainty on $f_{\rm NL}$ (*top*), $\varepsilon_{\rm D}$ (*middle*), and $\varepsilon_{\rm L}$ (*bottom*) as a function of the minimum angular multipole $\ell_{\rm min}$, in the single-tracer (*left panels*) and multi-tracer (*right panels*) cases.

The results for the non-Gaussianity and Doppler parameters are shown in Figure 5.5. It is clear that reducing the maximum scale (lowest ℓ) does significantly affect the

uncertainty in single surveys (*left panels*), for both $f_{\rm NL}$ (*top*) and $\varepsilon_{\rm D}$ (*middle*), as expected. By contrast, since cosmic variance is cancelled in the multi-tracer (*right panels*), the ultra-large scales have a smaller influence on the constraints, as previously highlighted. The constraints are much more robust to the loss of the largest scales. We conclude that our constraints should not be much affected by ultra-large scale systematics when using the multi-tracer technique.

It is worth noting that the constraints from the IM1 survey are less susceptible to increasing $\ell_{\rm min}$, because it includes extremely large-scale correlations along the line of sight, up to $(z_i, z_j) = (0.35, 3.05)$. In addition, we find that the uncertainty on $\varepsilon_{\rm D}$ from the BGS survey closely follows IM1, because of the effect mentioned earlier: despite the reduction in observed volume at low z, the Doppler amplitude $A_{\rm D}$ is much bigger for BGS, and the magnitude of $\boldsymbol{n} \cdot \boldsymbol{v}$ is notably larger. The improved noise properties at low z also contributes to the fact that IM2⊗BGS constrains $\varepsilon_{\rm D}$ much better than IM1⊗Hα.

In the case of lensing magnification, the signal does not depend significantly on ultra-large scales and we expect little effect from increasing $\ell_{\rm min}$. This expectation is confirmed by Figure 5.5 (bottom panels).

5.4.2 Constraints on standard cosmological parameters

Before estimating the biases on best-fit values, we first determine at which precision the standard cosmological parameters can be constrained. The marginal errors on the cosmological parameters as a fraction of the fiducial values are presented in Table 5.4, expressed in percentages. Generally the high-redshift surveys give better constraints – since they observe a larger volume and hence sample more correlations between points. However, in the multi-tracer combination, the low-z surveys provide better constraints than the high-z surveys. The reason is that cosmic variance is effectively cancelled in the MT analysis, thereby negating the advantage of the bigger volume at high z. Furthermore, the low z surveys have the advantage of lower noise. The exception is the dark energy equation of state w, which benefits from measurements before and after dark energy domination, that are available only in SKAO IM1. The best constraints are achieved when all surveys are combined. In particular, the error on Ω_{m0} is sub-percent, while all others are a few percent. The full multi-tracer combination produces a significant improvement in precision.

Figure 5.6 displays the contour plots for the standard cosmological parameters, together with $f_{\rm NL}$. Fiducial values are indicated by the dotted lines, and *black* contours indicate the multi-tracer correlation of all the surveys. The low- and high-z multi-tracer

Table 5.4 Marginal errors (in percentage) on standard cosmological parameters, for individual surveys and in multi-tracer ($\otimes$) combination, including all relativistic effects. $\oplus$ denotes the sum of independent multi-tracer pairs (excluding the IM2 band overlap in band IM1). Results exclude priors.

Redshift	Survey	$\Omega_{\rm m0}$	$n_{\rm s}$	H_0	w	$A_{\rm s}$
$0.10-0.58$	BGS	2.34	5.95	12.43	5.25	19.41
	IM2	3.57	8.89	18.57	4.85	28.03
	IM2$\otimes$BGS	1.14	2.04	3.78	3.30	5.96
$0.90-1.80$	Hα	1.18	3.57	6.79	3.19	10.37
$0.35-3.05$	IM1	2.27	5.64	11.23	2.53	16.57
$0.60-3.05$	IM1$\otimes$Hα	1.13	2.85	5.60	2.29	8.32
$0.10-3.05$	(IM2$\otimes$BGS)$\oplus$(IM1$\otimes$Hα)	0.69	1.58	3.08	1.35	4.61
	IM2$\otimes$BGS$\otimes$IM1$\otimes$Hα	0.68	1.55	3.02	1.34	4.51

pairs are in *blue* and *red* respectively. The sum of their Fisher information is in *green*. A strong degeneracy is apparent between $n_{\rm s}$, H_0, and $A_{\rm s}$, which is reduced as more data sets are added. By contrast, w and $\Omega_{\rm m0}$ are differently degenerate with the other parameters at low and high redshifts. Except for w, all cosmological parameters appear to be uncorrelated with $f_{\rm NL}$, which is not unexpected.

Another feature of Figure 5.6 and Table 5.4 is that the constraints and contours do not improve significantly when the sum of multi-tracer pairs is replaced by the full multi-tracer. This indicates that taking them as uncorrelated is a good approximation, since little information is added from low-$z \otimes$ high-z cross-correlations. The approximation considerably decreases the computation time needed.

5.4.3 Bias from neglecting relativistic effects

We now consider the bias on the best-fit value from neglecting all relativistic effects, beginning with the standard cosmological parameters. Table 5.5 shows the biases on the best-fit of ψ_i, normalised to $\sigma(\psi_i)$, that follows from neglecting all relativistic effects in the modeling – i.e., $\delta^{\rm rel}\psi_i$, defined in (5.10). At low z, neglecting the relativistic effects is justified, even for the multi-tracer pair IM2$\otimes$BGS. The same is true for the high-z IM1 on its own. By contrast, neglecting the relativistic effects in the Hα survey on its own leads to a significant bias for all parameters. This bias is then passed on to any multi-tracer that includes the Hα survey.

Figure 5.7 shows the contours corresponding to Table 5.5. The low-z multi-tracer pair and the high-z multi-tracer pair disagree on the best-fit value for all parameters

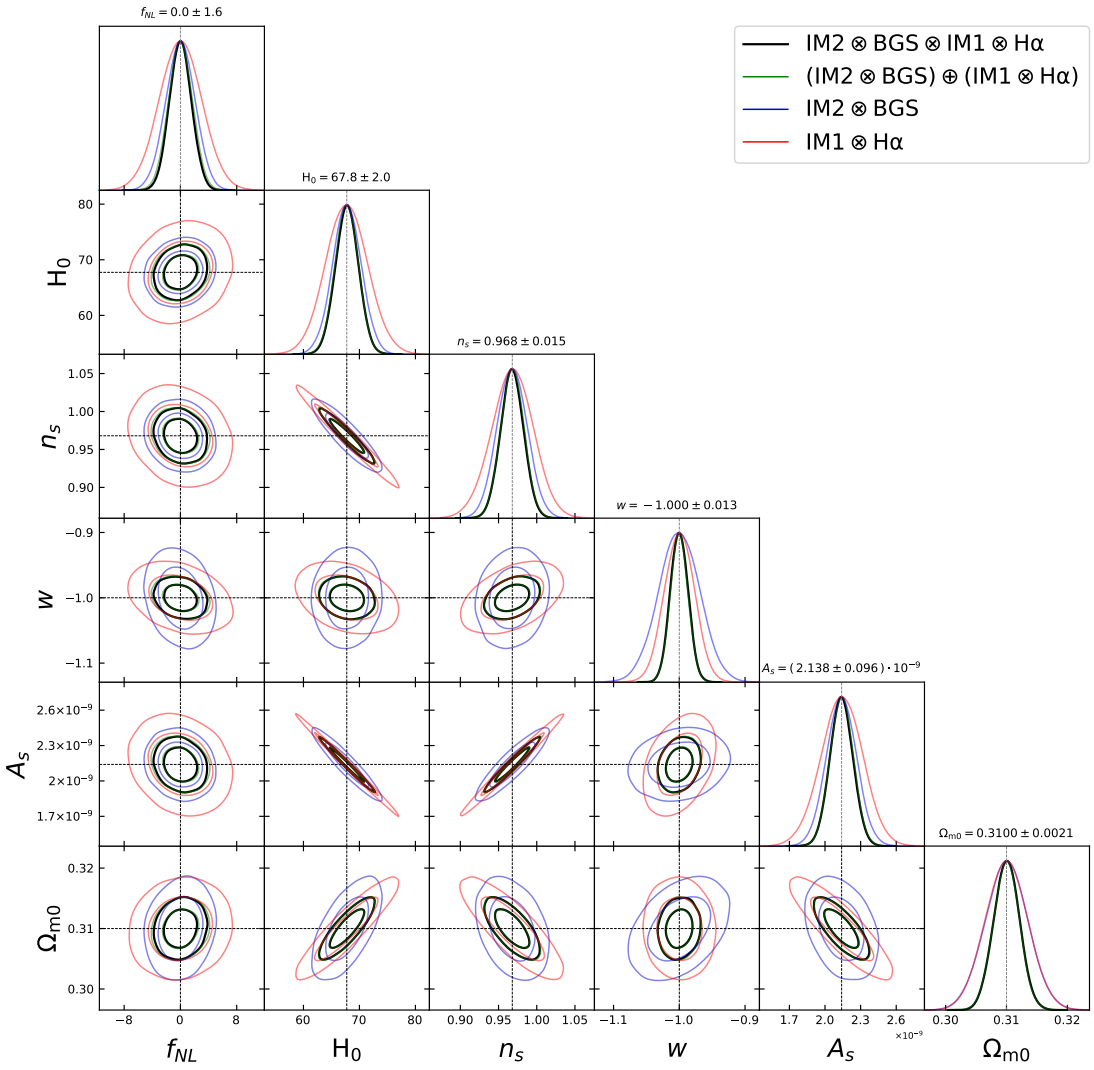

Fig. 5.6 Contour plots of the standard cosmological parameters and $f_{\rm NL}$: full multi-tracer combination of all 4 surveys (*black*); low-z multi-tracer pair (*blue*); high-z multi-tracer pair (*red*); sum of low-z and high-z Fisher information (*green*). Fiducial values are indicated by dotted lines. Constraints exclude priors.

when relativistic effects are neglected. In other words, there is a tension between low-z and high-z results, which is not eased by combining them. This clearly exemplifies the problem of theoretical systematics.

In Table 5.6, we present the marginal error on $f_{\rm NL}$ and the bias on its best-fit value, arising from neglecting the Doppler, lensing and potential effects, (5.9), and their combination, (5.10). The first column reproduces the results already presented in Table 5.1, and serves to normalise the biases on the true value $\bar{f}_{\rm NL} = 0$. The last column is the equivalent of Table 5.5 for $f_{\rm NL}$. The columns in between break down the

Table 5.5 Bias on the best-fit value of each standard cosmological parameter (normalised by the standard deviation) that follows from neglecting relativistic effects.

Redshift	Survey	$\delta^{\rm rel}\Omega_{\rm m0}$	$\delta^{\rm rel}n_{\rm s}$	$\delta^{\rm rel}H_0$	$\delta^{\rm rel}w$	$\delta^{\rm rel}A_{\rm s}$
$0.10-0.58$	BGS	0.17	-0.17	0.18	-0.1	-0.18
	IM2	0.01	-0.01	0.01	0.0	-0.02
	IM2⊗BGS	0.25	-0.30	0.44	-0.67	-0.51
$0.90-1.80$	Hα	5.46	-7.23	6.98	-7.81	-7.14
$0.35-3.05$	IM1	0.01	-0.01	0.01	-0.02	-0.01
$0.60-3.05$	IM1⊗Hα	6.12	-8.71	8.04	-9.14	-8.14
$0.10-3.05$	(IM2⊗BGS)⊕(IM1⊗Hα)	3.42	-4.66	4.28	-4.81	-4.17
	IM2⊗BGS⊗IM1⊗Hα	6.07	-7.53	7.25	-7.34	-7.05

Table 5.6 Marginal error and normalised best-fit biases $\delta^I f_{\rm NL}$ on $f_{\rm NL}$, from neglecting the Doppler, lensing and potential effects, and their combination, $\delta^{\rm rel}f_{\rm NL}$.

Redshift	Survey	$\sigma(f_{\rm NL})$	$\delta^{\rm D}f_{\rm NL}$	$\delta^{\rm L}f_{\rm NL}$	$\delta^{\rm P}f_{\rm NL}$	$\delta^{\rm rel}f_{\rm NL}$
$0.10-0.58$	BGS	26.38	-0.05	0.17	0.02	0.14
	IM2	35.74	-0.03	–	0.0	-0.03
	IM2⊗BGS	2.12	0.04	0.49	0.09	0.62
$0.90-1.80$	Hα	9.34	0.10	6.03	-0.08	6.06
$0.35-3.05$	IM1	4.72	0.04	–	-0.06	-0.02
$0.60-3.05$	IM1⊗Hα	3.06	0.08	3.11	-0.15	3.04
$0.10-3.05$	(IM2⊗BGS)⊕(IM1⊗Hα)	1.70	0.06	1.84	-0.01	1.89
	IM2⊗BGS⊗IM1⊗Hα	1.55	0.10	2.60	-0.01	2.69

bias into the three components of the relativistic effects. Note that intensity mapping is unaffected by lensing magnification.

As in the case of the standard cosmological parameters, neglecting the relativistic effects at low redshift does not significantly bias the best-fit value of $f_{\rm NL}$. Similarly, the high redshift IM1 survey does not show significant bias in $f_{\rm NL}$, and it is again only the Hα survey that suffers a significant bias on the best-fit. This $> 1\sigma$ bias propagates into all multi-tracer combinations with Hα. It is apparent that the $> 1\sigma$ bias is mainly due to the neglect of lensing magnification, and it follows that lensing must be included in the analysis.

The Doppler and potential effects can lead to a bias up to 13% of the error bars, in the case of IM2⊗BGS. This is a significant fraction of the total 62% bias, with lensing contributing 49%. If we are only interested in biases above 1σ, we can neglect the

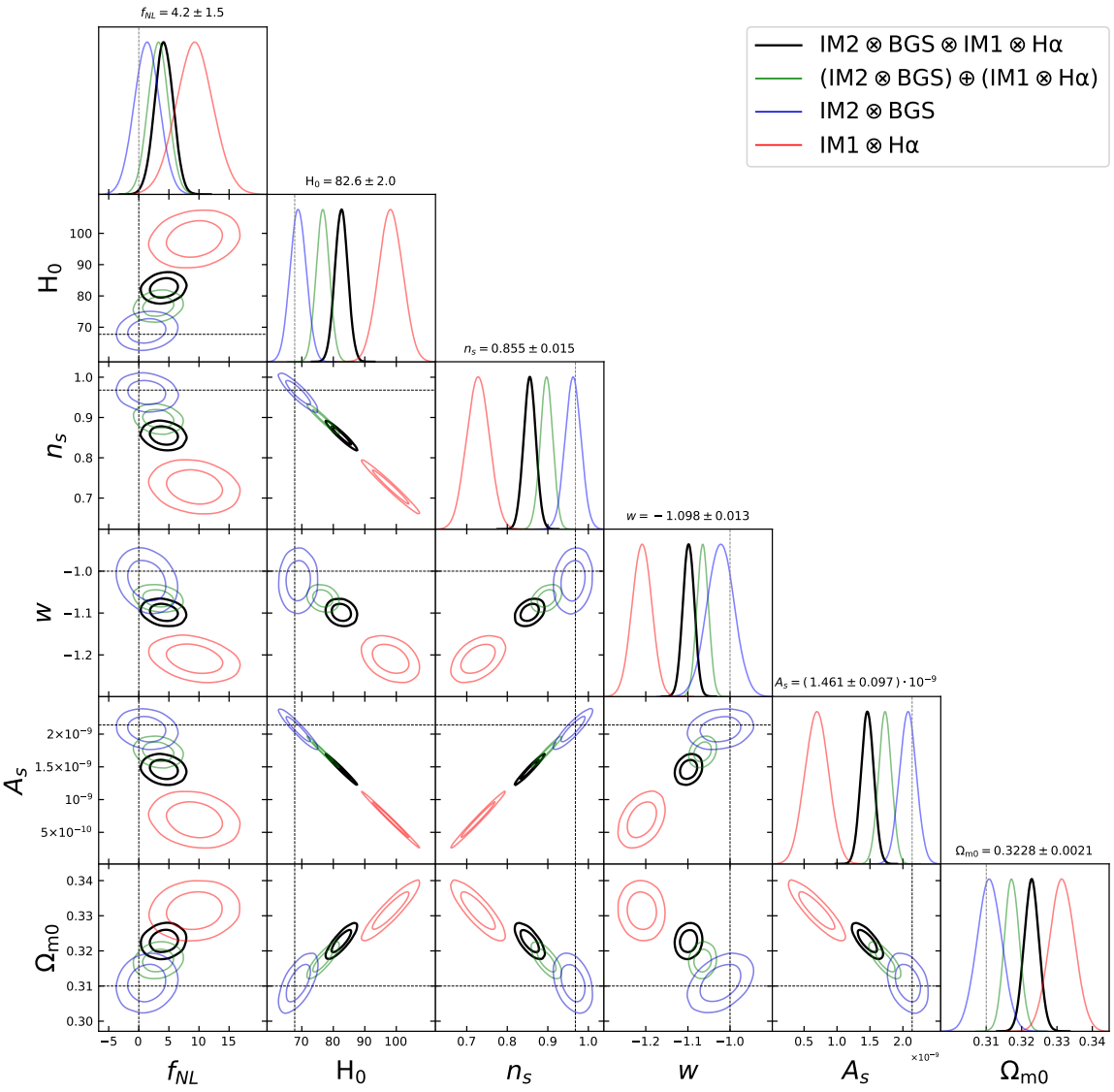

Fig. 5.7 Same as Figure 5.6, but now neglecting relativistic effects, i.e. lensing, Doppler and potential effects. The best-fit values from the full multi-tracer combination (*black*) are given above the distributions, showing the consequent bias on the true values (marked by dotted lines).

Doppler and potential contribution. However, there may be other survey combinations for which the Doppler and potential effects, when added to the lensing effect, push the bias above 1σ (or pull it below 1σ).

Figure 5.7 presents the contours in the case where all relativistic effects are neglected. This incorrect model will introduce theoretical systematics in the form of a bias on the best-fit values of the parameters. For the low-z multi-tracer pair, the bias is small enough that the fiducials are still contained within the 1σ contours. On the other hand,

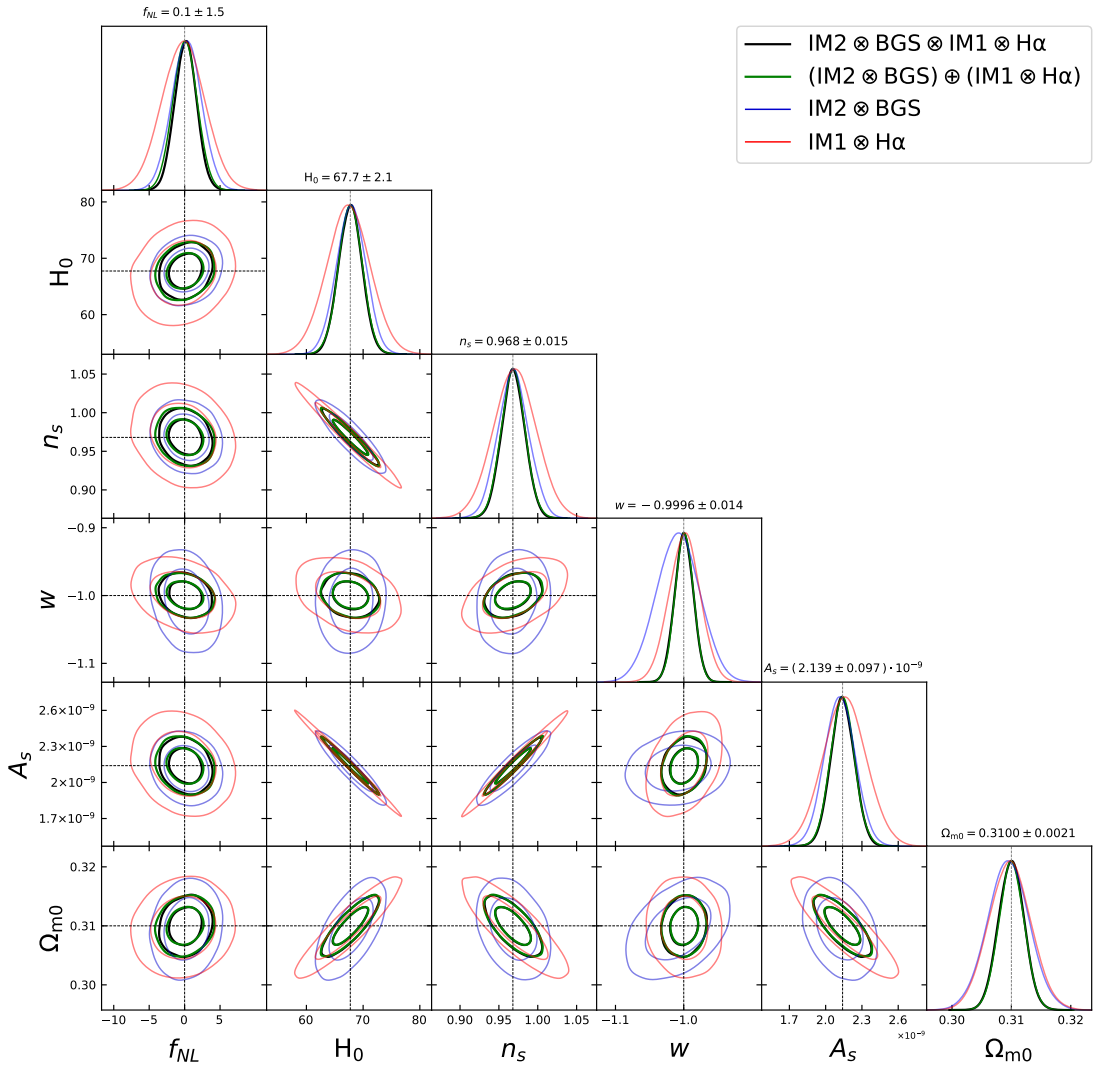

Fig. 5.8 As in Figure 5.7, but now neglecting the Doppler and potential effects, while including the lensing effect.

the high-z multi-tracer pair shows strong biases in all best-fit values, in tension with the low-z pair. In particular, the wrong theoretical model in the high z case leads us to detect a spurious $f_{\rm NL} \sim 10$ at 3σ, whereas the true value implies Gaussian initial conditions. It is also apparent that when combining the low- and high-z data sets, the spurious $f_{\rm NL}$ detection remains (~ 4 at $\sim 2\sigma$).

Table 5.5, Table 5.6 and Figure 5.7 show that the biases in the best-fit parameters come overwhelmingly from the Euclid-like Hα survey. It is clear that relativistic effects must be included in the modeling for theoretical accuracy. Table 5.6 confirms that we can safely omit the Doppler and potential effects for the surveys considered.

To confirm this, we compute the bias on the best-fit value from neglecting the Doppler and potential but keeping the lensing effect. Figure 5.8 shows that including lensing in the modelling is sufficient to de-bias all parameters. Although some residual bias remains, it is within the 1σ contours. Therefore we conclude that for these surveys, and their combinations, it is safe to neglect Doppler and potential effects, if the goal is to measure $f_{\rm NL}$ and the standard cosmological parameters.

We emphasise that the Doppler contribution itself is detectable, with signal-to-noise of ~ 8, and for the purpose of detection, it should be included in the modeling. We do not expect any significant bias on the standard cosmological parameters from neglecting the Doppler term, since this term is only non-negligible on ultra-large scales, which contribute little to the standard constraints. This is confirmed in Table 5.7 to Table 5.11 below. The $f_{\rm NL}$ constraints do rely critically on ultra-large scales, and neglecting the Doppler effect biases the $f_{\rm NL}$ best-fit by 10% for the full multi-tracer combination of the surveys considered here (Table 5.6). There may be other combinations of surveys for which the neglect of the Doppler term produces a more significant bias on the $f_{\rm NL}$ best-fit.

5.4.4 Gaussian universe

Let us also consider the impact of relativistic effects in a Gaussian universe, i.e. where $f_{\rm NL} = 0$. *Is it necessary to include the light-cone effects to avoid any bias in the measurements of the standard cosmological parameters?* As before, we use (2.26) to compute the relative bias on the best-fit value from neglecting the Doppler effect $\delta^{\rm D}$, lensing $\delta^{\rm L}$, and potential terms $\delta^{\rm P}$, as well as the combination of them $\delta^{\rm rel}$. However, here we also include primordial non-Gaussianity in the subset

$$\varphi_I = \left\{ f_{\rm NL}, \varepsilon_{\rm D}, \varepsilon_{\rm L}, \varepsilon_{\rm P} \right\}, \tag{5.11}$$

and fix it to the fiducial value, such that $\delta f_{\rm NL} = \bar{f}_{\rm NL} - \hat{f}_{\rm NL} = 0$. We summarise the results for single- and multi-tracer cases in Table 5.7 to Table 5.11 for the parameters $\Omega_{\rm m0}$, $n_{\rm s}$, H_0, w and $A_{\rm s}$.

As expected, neglecting the Doppler and potential effects does not bias any best-fit values significantly. The largest bias is $\sim 25\%$ on w in the low-z multi-tracer IM2⊗BGS, which is less than 1σ. For the lensing effect, the same applies at low redshifts. Once again, it is only a Euclid-like Hα survey and its combinations with the other surveys, that leads to significant biases in all parameters when lensing is neglected. Although the trend is the same as found previously, the relative biases are generally smaller.

Table 5.7 Normalised best-fit bias in the matter density $\delta^I\Omega_{\rm m0}$, from neglecting Doppler, lensing and potential effects, and their combination $\delta^{\rm rel}\Omega_{\rm m0}$.

Redshift	Survey	$\delta^{\rm D}\Omega_{\rm m0}$	$\delta^{\rm L}\Omega_{\rm m0}$	$\delta^{\rm P}\Omega_{\rm m0}$	$\delta^{\rm rel}\Omega_{\rm m0}$
$0.10-0.58$	BGS	0.01	0.17	0.0	0.18
	IM2	0.02	–	0.0	0.02
	IM2⊗BGS	-0.15	0.4	0.01	0.26
$0.90-1.80$	Hα	0.01	5.59	0.0	5.6
$0.35-3.05$	IM1	-0.01	–	0.01	0.01
$0.60-3.05$	IM1⊗Hα	-0.09	6.24	0.01	6.15
$0.10-3.05$	(IM2⊗BGS)⊕(IM1⊗Hα)	-0.01	3.46	0.0	3.45
	IM2⊗BGS⊗IM1⊗Hα	0.0	6.13	0.0	6.13

Table 5.8 As in Table 5.7, for the spectral index $n_{\rm s}$.

Redshift	Survey	$\delta^{\rm D}n_{\rm s}$	$\delta^{\rm L}n_{\rm s}$	$\delta^{\rm P}n_{\rm s}$	$\delta^{\rm rel}n_{\rm s}$
$0.10-0.58$	BGS	0.0	-0.18	0.0	-0.19
	IM2	-0.01	–	0.0	-0.01
	IM2⊗BGS	0.03	-0.32	-0.01	-0.30
$0.90-1.80$	Hα	-0.02	-7.57	-0.01	-7.60
$0.35-3.05$	IM1	-0.01	–	0.01	0.01
$0.60-3.05$	IM1⊗Hα	0.10	-8.96	-0.01	-8.87
$0.10-3.05$	(IM2⊗BGS)⊕(IM1⊗Hα)	0.02	-4.76	0.0	-4.74
	IM2⊗BGS⊗IM1⊗Hα	0.02	-7.65	-0.01	-7.63

Table 5.9 As in Table 5.7, for the Hubble parameter H_0.

Redshift	Survey	$\delta^{\rm D}H_0$	$\delta^{\rm L}H_0$	$\delta^{\rm P}H_0$	$\delta^{\rm rel}H_0$
$0.10-0.58$	BGS	0.0	0.19	0.0	0.20
	IM2	0.02	–	0.0	0.02
	IM2⊗BGS	0.05	0.39	0.01	0.44
$0.90-1.80$	Hα	0.02	7.42	0.0	7.44
$0.35-3.05$	IM1	0.0	–	0.01	0.01
$0.60-3.05$	IM1⊗Hα	-0.10	8.26	0.01	8.17
$0.10-3.05$	(IM2⊗BGS)⊕(IM1⊗Hα)	0.0	4.35	0.01	4.36
	IM2⊗BGS⊗IM1⊗Hα	0.0	7.34	0.01	7.36

This may be caused by the reduction in the parameter space volume when $f_{\rm NL}$ is fixed to zero. In any case, such marginal reduction should be interpreted qualitatively,

Table 5.10 As in Table 5.7, for the dark energy equation of state w.

Redshift	Survey	$\delta^{\rm D}w$	$\delta^{\rm L}w$	$\delta^{\rm P}w$	$\delta^{\rm rel}w$
$0.10-0.58$	BGS	0.03	-0.14	-0.01	-0.12
	IM2	0.0	–	0.0	0.0
	IM2⊗BGS	-0.25	-0.43	-0.01	-0.69
$0.90-1.80$	Hα	-0.03	-8.59	-0.0	-8.63
$0.35-3.05$	IM1	-0.03	–	0.01	-0.02
$0.60-3.05$	IM1⊗Hα	0.05	-9.63	0.0	-9.58
$0.10-3.05$	(IM2⊗BGS)⊕(IM1⊗Hα)	0.07	-4.97	-0.02	-4.93
	IM2⊗BGS⊗IM1⊗Hα	0.06	-7.52	-0.03	-7.48

Table 5.11 As in Table 5.7, for the primordial power spectrum amplitude $A_{\rm s}$.

Redshift	Survey	$\delta^{\rm D}A_{\rm s}$	$\delta^{\rm L}A_{\rm s}$	$\delta^{\rm P}A_{\rm s}$	$\delta^{\rm rel}A_{\rm s}$
$0.10-0.58$	BGS	0.01	-0.21	-0.01	-0.21
	IM2	-0.02	–	0.0	-0.02
	IM2⊗BGS	-0.18	-0.33	0.0	-0.52
$0.90-1.80$	Hα	-0.03	-7.71	0.0	-7.74
$0.35-3.05$	IM1	0.0	–	-0.01	-0.01
$0.60-3.05$	IM1⊗Hα	0.10	-8.39	-0.01	-8.30
$0.10-3.05$	(IM2⊗BGS)⊕(IM1⊗Hα)	0.0	-4.23	-0.01	-4.24
	IM2⊗BGS⊗IM1⊗Hα	-0.01	-7.13	-0.01	-7.15

given the approximation used to compute the bias. The take-home message is that for high-z spectroscopic galaxy surveys, lensing magnification must be included for unbiased measurements of the standard cosmological parameters.

5.5 Discussion and conclusion

In this chapter, we investigated how combinations of next-generation large-scale structure surveys in the optical and radio can constrain primordial non-Gaussianity and relativistic effects. Primordial non-Gaussianity is a powerful probe of the very early Universe and its signal in the power spectrum is preserved on ultra-large scales. The relativistic effects include the contribution of lensing magnification to the number density contrast, which provides a probe of gravity and matter that is independent of the probes delivered by weak lensing shear surveys. Of the remaining relativistic

effects, the Doppler effect is the most important, and provides another new probe of gravity and matter.

We chose a pair of spectroscopic surveys at low redshift and another at high redshift, which have the lowest noise in the respective parts of the electromagnetic spectrum, and which cover large areas of the sky. At low z we chose a DESI-like Bright Galaxy Sample [183] in the optical and an HI intensity mapping survey with Band 2 of the SKAO MID telescope [95]. The high redshift pair is a Euclid-like Hα spectroscopic survey [125] and HI IM with Band 1 of SKAO MID [95].

We identified which pairs of correlations are most sensitive to the lensing and Doppler effects, using a signal-to-noise estimator S^{AB} in (5.2) for angular power spectra (similar to the estimator used in the two-point correlation function by [84]). The observable angular power spectra $C_\ell^{AB}(z_i, z_j)$ are used in the analysis, since they naturally include relativistic light-cone effects, wide-angle effects and correlations between all redshift bins, and do not require an Alcock-Paczynski correction. The results are summarised in Figure 5.3. This shows clearly that pairs (z_i^A, z_{i+1}^B) are optimal for the Doppler effect and are central to the results in [180, 189]. The Doppler effect (1.50) is also more prominent at low redshifts which is broadly explained by the $1/\chi$ in its amplitude, as well as by the greater magnification bias and growth of the radial peculiar velocity at low z.

On the other hand, the lensing contribution is stronger at higher redshift and is most relevant in pair correlations (z_1^A, z_n^A), where n is the total number of bins. Although this is expected, since lensing is a line-of-sight integrated effect, Figure 5.3 shows it in a visually intuitive manner.

Figure 5.3 also revealed a counter-intuitive feature – that the cross-correlation between a galaxy survey and an intensity mapping survey enhances the lensing signal, even though the intensity mapping on its own has no lensing signal. The point is that background galaxies are lensed by foreground intensity.

We then computed Fisher forecasts of the constraints on $f_{\rm NL}$ and the relativistic effects, for all single-tracer cases, for multi-tracer pairs at low and high z, and for the full multi-tracer combination of all four surveys. As expected, the full combination provides the most stringent constraints on $f_{\rm NL}$, improving on the state-of-the-art constraint from Planck [10] by a factor of more than 3. The lensing contribution can be detected at $\sim$2% accuracy, while the Doppler contribution can be detected with a signal-to-noise of $\sim$8.

We presented our forecasts in two scenarios. First, we assumed that the light-cone effects are perfectly modelled, i.e., the magnification and evolution biases are perfectly

known. In the second case, we incorporated the model uncertainties in the amplitude of the relativistic contribution to the angular power, by marginalising over $\varepsilon_{\rm D}, \varepsilon_{\rm L}$ and $\varepsilon_{\rm P}$ parameters. Predictably, the first scenario provides the best possible constraints. However, the second scenario constraints approach those of the first when we consider multi-tracer pairs – and even more when we combine all surveys. The multi-tracer shows one of its strengths: robustness against marginalisation.

It is notable that for the lensing contribution most information comes from the Hα survey alone. For the Doppler term, most of the constraints come from the low-redshift multi-tracer. For Doppler and lensing, there is sufficient sensitivity to detect their effects in the C_ℓ. On the other hand, the relativistic potential terms are too small to be detected, even when combining all surveys.

In the case of $f_{\rm NL}$, the multi-tracer results with spectroscopic galaxy surveys delivers $\sigma(f_{\rm NL}) \sim 1.5$. This is not as good as some forecasts with photometric galaxy surveys (see e.g. [91, 95, 97]). Photometric surveys utilise wider redshift bins which contain more galaxies, and hence lower noise. The survey noise is the limiting factor in the multi-tracer, since cosmic variance has been cancelled. Therefore, spectroscopic multi-tracer (with relativley thin z-bins) is not optimised for $f_{\rm NL}$, and this was not our focus here. On the other hand, the spectroscopic combination delivers a $\sim$10% detection of the Doppler effect, which is not possible with photometric surveys.

We stress that it is important to join the low and high redshift surveys to break degeneracies between $f_{\rm NL}$ and the relativistic effects, as seen in Figure 5.4. In addition, the multi-tracer technique provides critical robustness against the loss of information due to systematics on ultra-large scales, as shown in Figure 5.5.

Next we focused on the potential theoretical systematic bias on measurements of $f_{\rm NL}$ and standard cosmological parameters, which can arise if the relativistic effects are neglected in the modeling.

First we estimate the expected precision on the standard cosmological parameters via a Fisher forecast – using the correct theoretical model, which includes lensing magnification, Doppler and potential effects, in addition to the standard redshift-space distortion effect. Table 5.4 shows that the multi-tracer significantly improves on single-tracer precision, due to the combination of information, inclusion of cross-spectra and the elimination of cosmic variance. The contour plots in Figure 5.6 visually demonstrate the improvement in precision from combining low- and high-z survey combinations, as well as showing the breaking of degeneracies between several parameters. The same qualitative features apply to the precision on $f_{\rm NL}$.

Then we investigated what happens when we use the incorrect theoretical model, i.e. when we neglect one or more of the relativistic effects in the model. This leads to a theoretical systematic that threatens accurate measurement – by biasing the best-fit (or measured) values of the parameters, as given by (2.26), (5.9) and (5.10). The important question is: exactly how large is this bias for $f_{\rm NL}$ and the cosmological parameters? If the bias is $< 1\sigma$, the relativistic effect can be neglected if necessary; otherwise it must be included. Each parameter in the model that is not fixed will be biased by disregarding a relativistic effect. The more free parameters there are, the greater the parameter space volume and hence the larger the potential bias.

The results on best-fit bias are summarised in Table 5.5–Table 5.11 and Figure 5.7. When we separate the relativistic effects, we see that only the neglect of lensing leads to a bias above 1σ on $f_{\rm NL}$ and cosmological parameters, while neglecting the Doppler leads to at most a 25% bias. If we are pressed to save computation time, we can therefore neglect the Doppler and potential effects, as confirmed in Figure 5.8.

It is clear that lensing effects cannot be neglected for the Hα-like survey, or for any multi-tracer combination involving the Hα survey, – including the full multi-tracer combination considered here. The special role of lensing in the Hα survey is due to: (a) its high redshift reach which boosts the lensing effects, as shown in Figure 5.9; (b) the fact that the 21cm intensity surveys are unaffected by lensing magnification, although they can contribute to the lensing of galaxies in cross-correlations. The BGS galaxy survey can also detect the lensing effect, but only at low significance, given its low redshift reach.

We confirmed that the same qualitative statements apply in the case of the bias on the cosmological parameters in a Gaussian universe, where $f_{\rm NL}$ is fixed at zero. The results are summarised in Table 5.7 to Table 5.11.

One might ask how lensing drives the bias on $f_{\rm NL}$, given that its signal does not require ultra-large scales in order to be significant. The point is that the lensing magnification contribution $(5s-2)\,\kappa$ is a weighted average along the line of sight of the matter density contrast – and therefore it can mimic a change in the Gaussian clustering bias, which in turn can bias the amplitude of the $f_{\rm NL}$ contribution [85, 87].

Our results are broadly consistent with previous work on galaxy surveys, in particular [79, 80, 85–88, 192], but we consider a different combination of surveys and we use the full multi-tracer combination of four surveys.

In [84], the bias on cosmological parameters is negligible for spectroscopic surveys but significant for photometric surveys. However, [84] uses the two-point correlation function, without cross-bin correlations, for spectroscopic surveys. A similar result

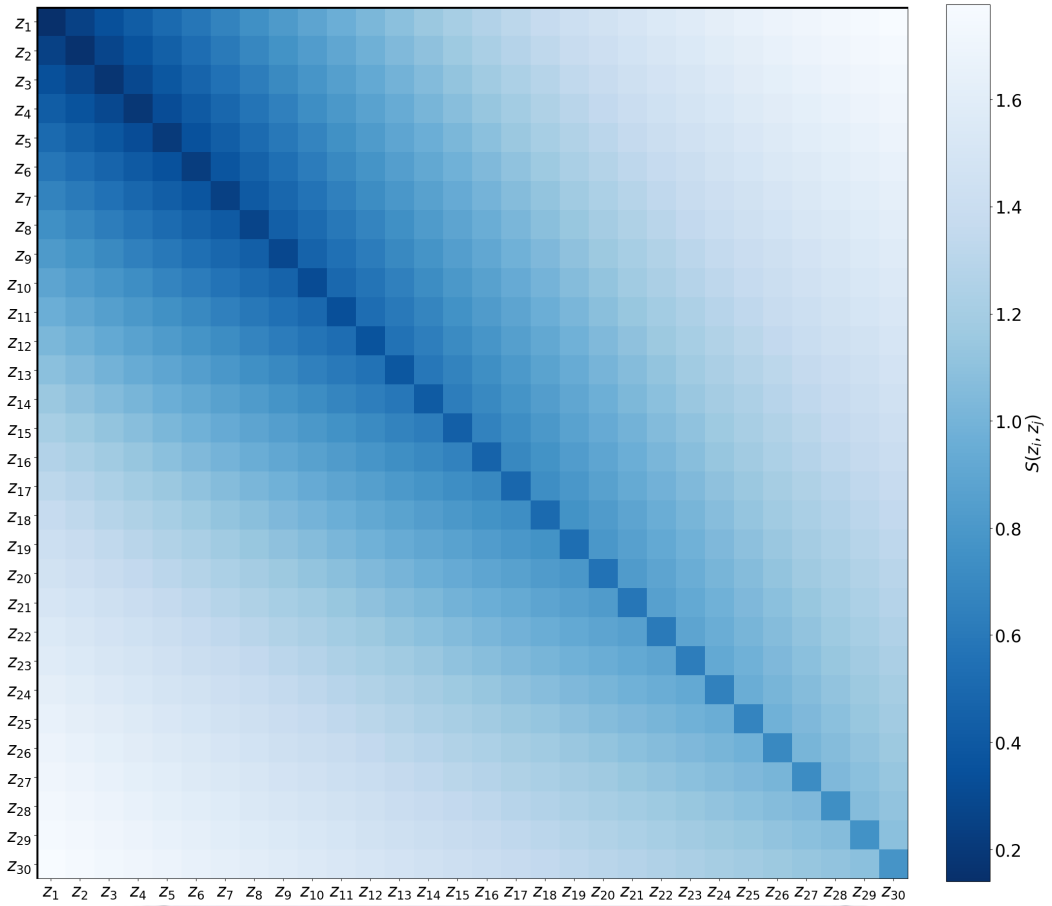

Fig. 5.9 Signal-to-noise $S(z_i, z_j)$ of the lensing magnification contribution in the Euclid-like Hα survey over its redshift range $0.9 < z < 1.8$.

was found in [110] for spectroscopic surveys using the angular power spectrum in a hybrid approach which, like [84], does not consider correlations from large redshift differences. By contrast, we include all cross-bin correlations amongst many thin bins. In Figure 5.9, we show the lensing magnification contribution from each individual auto- and cross-bin correlation of a Euclid-like Hα survey. The signal-to-noise ratio S is given by (5.2). It is clear that widely separated cross-bin correlations have the highest signal-to-noise. This accounts for our different conclusion – and also explains why we agree with the result of [84] on photometric surveys, for which they do include cross-bin correlations via a tomographic analysis.

The key point is that, in order to avoid serious bias on the best-fit values of $f_{\rm NL}$ and cosmological parameters, the effect of lensing magnification on the galaxy power spectrum must be included in upcoming surveys which cover high redshifts. The inclusion of lensing in the theoretical modeling highlights the importance of

Table 5.12 Survey volumes and uncertainties on $f_{\rm NL}$ and relativistic terms in (2.10), marginalising over the standard cosmological parameters (excluding priors). $\sigma(\varepsilon_{\rm P})$ is always $\gg 1$ and is not shown. Uncertainties when marginalising *also* over the Gaussian clustering biases in each bin, $b_A(z_i)$, are in brackets.

Redshift	Survey	$\Omega_{\rm sky}/{\rm deg}^2$	$\sigma(f_{\rm NL})$	$\sigma(\varepsilon_{\rm D})$	$\sigma(\varepsilon_{\rm L})$
$0.1-0.58$	BGS (DESI-like)	15,000	26.36 (26.38)	7.57 (7.57)	0.32 (0.39)
	IM2 (SKAO-like)	20,000	35.33 (35.74)	18.04 (18.07)	–
	IM2⊗BGS	10,000	2.10 (2.12)	0.14 (0.14)	0.12 (0.13)
$0.9-1.8$	Hα (Euclid-like)	15,000	9.32 (9.34)	9.08 (9.08)	0.04 (0.04)
$0.35-3.05$	IM1 (SKAO-like)	20,000	4.65 (4.72)	6.28 (6.29)	–
$0.60-3.05$	IM1⊗Hα	10,000	3.05 (3.06)	0.37 (0.37)	0.03 (0.03)
$0.1-3.05$	(IM2⊗BGS)⊕(IM1⊗Hα)	10,000	1.70 (1.70)	0.13 (0.13)	0.03 (0.03)
	IM2⊗BGS⊗IM1⊗Hα	10,000	1.55 (1.55)	0.13 (0.13)	0.02 (0.02)

good-precision estimates of the lensing magnification bias parameter (see also [3, 43, 78–80, 84, 87, 88, 91, 92, 171]). The lensing magnification and associated parameter s are given in section 3.3

The precision on the lensing and Doppler contributions would be washed away if s and b_e are poorly measured. We have partially allowed for uncertainties in s and b_e by marginalising over the lensing and Doppler parameters $\varepsilon_{\rm L}$ and $\varepsilon_{\rm D}$. Based on the analysis in [91], we can estimate that errors on s and b_e need to be $\lesssim 10\%$ in order to preserve detectability of the lensing and Doppler effects.

Finally, we note that our simplified analysis based on Fisher forecasts means that our estimates of the impact of lightcone effects should be regarded as optimistic. We have fully included uncertainties from cosmological parameters and from the modelling of Gaussian clustering biases $b_A(z_i)$. These are important, but they have little impact on the multi-tracer, as shown in Table 5.12. Observational systematics have not been incorporated into our analysis. Systematics on ultra-large scales include stellar contamination and dust extinction for galaxy surveys (see e.g. [190]), and foreground contamination for intensity surveys (see e.g. [123, 193, 194]). We have made some allowance for these systematics by excluding the largest scales via the cut $\ell \geq \ell_{\rm min} = 5$. In Figure 5.5 we showed that the full multi-tracer constraints on $f_{\rm NL}$, $\varepsilon_{\rm L}$ and $\varepsilon_{\rm D}$ are robust to an increase of $\ell_{\rm min}$, up to $\sim 10-20$.

Chapter 6

Summary

In chapter 1 we gave a brief overview of the standard model of cosmology and perturbation theory, as well as light-cone effects in general relativity. We recall how the matter distribution is analysed in cosmological surveys in chapter 2, and how to combine information using the multi-tracer technique. Specifically, we used the angular power spectrum C_ℓ in our analysis, which is observed in redshift space. Key advantages of C_ℓ include: it incorporates the redshift evolution of all cosmological, astrophysical and noise variables; it does not impose a flat-sky approximation but naturally incorporates wide-angle correlations; critically, the Doppler and lensing corrections to the two-point correlations are naturally included. Furthermore, since the angular power spectrum of the data is directly observable, its construction makes no assumptions regarding a fiducial model and circumvents the need of the Alcock-Paczynski correction.

In order to assess the precision on several cosmological and astrophysical parameters from future spectroscopic galaxy surveys, we employed a Fisher Matrix analysis. The details of the statistical technique is reviewed in chapter 2. In all our Fisher forecasts, we marginalised over the standard cosmological parameters, as well as the dark energy equation of state and the clustering bias in each redshift bin, for each survey. Our constraints are based only on the information from linear scales.

The technicalities of theoretically modelling galaxy surveys and intensity mapping surveys are explained in chapter 3. We focus on how to compute the magnification bias and evolution bias for several different surveys, as well as their associated noise properties. Instead of an exhaustive study of surveys, we tried to fill the redshift range $0 < z \lesssim 3$ with the potentially best contemporaneous spectroscopic surveys. Specifically, we considered large-scale structure surveys in the optical and radio bands: DESI-like BGS and Euclid-like Hα galaxy surveys, together with SKAO-like 21cm

intensity mapping surveys in lower- and higher-frequency bands. Our choice was motivated by: high redshift resolution (to detect RSD and the Doppler effect); a negligible cross-shot noise between optical and 21cm intensity samples; and with very different systematics affecting optical and 21cm radio surveys.

6.1 Constraints on growth rate

In chapter 4, we focused on constraints on the growth index γ, which offers a powerful consistency test for ΛCDM. We showed that cross-correlations between z-bins compensates for the growth in noise, and we concluded that in theory the thinnest possible width will deliver the highest signal-to-noise.

The main results for independent surveys are shown in Table 4.1 and in 1σ contour plots of Figure 4.3. The best marginal constraints (including priors) on γ are $\sim 3-5\%$ for the near-future surveys, with SKAO intensity mapping providing the best near-future constraints.

In addition, we included all possible information from these surveys, using multi-tracer cross-correlations on overlap volumes and single-tracer correlations on non-overlap volumes. The results from the MT are shown in Table 4.4 and in the contour plots of Figure 4.4 and Figure 4.5. The best marginal constraints on γ are $\sim$1.6 and $\sim$2.3% for combinations of low- and high-z surveys, respectively. By utilising the MT, the constraints from independent surveys are improved by up to $\sim$45%. If we take the further step of combining the low- and high-z combinations, we find a precision of 1.3%, which is $\sim$55% better than the best single-tracer. Therefore, combining the information from future spectroscopic surveys will significantly improve constraints of the growth rate of large-scale structure, without using more observational resources. In addition, another advantage of joining the information from low and high redshifts can break the degeneracy between $\Omega_{\rm m0}$ and γ.

6.2 Constraints on $f_{\rm NL}$ and light-cone effects

In chapter 5 we investigated how combinations of next-generation large-scale structure surveys in the optical and radio bands can constrain primordial non-Gaussianity and relativistic effects. Primordial non-Gaussianity is a powerful probe of the very early Universe and its signal in the power spectrum is preserved on ultra-large scales. The relativistic effects include the contribution of lensing magnification to the number density contrast, which provides a probe of gravity and matter that is independent

of the probes delivered by weak lensing shear surveys. Of the remaining relativistic effects, the Doppler effect is the most important, and provides another new probe of gravity and matter.

We identified which pairs of correlations are most sensitive to the lensing and Doppler effects, using a signal-to-noise estimator S^{AB} in (5.2) for angular power spectra. The results are summarised in Figure 5.3. This shows clearly that pairs (z_i^A, z_{i+1}^B) are optimal for the Doppler effect. The $1/\chi$ relation in the Doppler amplitude and growth of the radial peculiar velocity broadly explains why this effect is more prominent at low z. On the contrary, the lensing contribution is stronger at higher redshift and is most relevant in pair correlations (z_1^A, z_n^A), where n is the total number of bins.

Figure 5.3 also revealed a counter-intuitive feature – that the cross-correlation between a galaxy survey and an intensity mapping survey enhances the lensing signal, even though the intensity mapping on its own has no lensing signal. The reason is that background galaxies are lensed by foreground intensity.

Quantitatively we determined the constraints on $f_{\rm NL}$ and the relativistic effects, for all single-tracer cases, for multi-tracer pairs at low and high z, and for the full multi-tracer combination of all four surveys. As expected, the full combination provides the most stringent constraints on $f_{\rm NL}$, improving on the state-of-the-art constraint from Planck [10] by a factor of more than 3. The lensing contribution can be detected at $\sim$2% accuracy, while the Doppler contribution can be detected with a signal-to-noise of $\sim$8. Therefore, there is sufficient sensitivity to detect the Doppler and lensing effects in the C_ℓ. For the Doppler term, most of the constraints power comes from the low-redshift multi-tracer, and Hα provides most information on lensing. We also illustrate the robustness of the MT against marginalisation.

We stress that it is important to join the low and high redshift surveys to break degeneracies between $f_{\rm NL}$ and the relativistic effects, as seen in Figure 5.4. Also, it was found that the cancellation of cosmic variance in the multi-tracer has greatly improved the constraints on large-scale parameters such as $f_{\rm NL}$ and Doppler effect. In addition, the multi-tracer technique provides critical robustness against the loss of information due to systematics on ultra-large scales, as shown in Figure 5.5. In the case of $f_{\rm NL}$, the multi-tracer results with spectroscopic galaxy surveys delivers $\sigma(f_{\rm NL}) \sim 1.5$.

Also, we investigated what happens when one uses a simplified theoretical model, i.e. when we neglect one or more of the relativistic effects. We found that this will lead to a theoretical systematic that threatens accurate measurements – by biasing the best-fit (or measured) values of the parameters, as given by (2.26), (5.9) and

(5.10). The results on the best-fit bias are summarised in Figure 5.7, with detailed information in Table 5.5–Table 5.11. By separately considering the relativistic effects, we see that only neglecting lensing leads to a bias above 1σ on $f_{\rm NL}$ and cosmological parameters, while the neglect of Doppler leads to at most a 25% bias. If we are pressed to save computation time, we can therefore neglect the Doppler and potential effects, as illustrated in Figure 5.8. We confirmed that the same qualitative statements apply in the case of the bias on the cosmological parameters in a Gaussian universe, where $f_{\rm NL}$ is fixed at zero. The results are summarised in Table 5.7 to Table 5.11.

Our results are broadly consistent with previous work on galaxy surveys, in particular [79, 80, 85–88, 192], although we consider a different combination of surveys and we use the full multi-tracer combination of four surveys.

The key point is that, in order to avoid serious bias on the best-fit values of $f_{\rm NL}$ and cosmological parameters, the effect of lensing magnification on the galaxy power spectrum must be included in upcoming surveys which cover high redshifts.

6.3 Future work

In order to improve the accuracy of the forecast constraints, we should properly include the uncertainty of the astrophysical parameters, like magnification bias and evolution bias. We have partly included the uncertainty in these parameters by marginalising over the amplitude of the light-cone effects, i.e. magnification lensing, Doppler effect, as well as the potential terms. However, in future work we plan to include such uncertainties in the model by marginalising over the b_e and $\mathcal{Q}$ parameters explicitly. As shown, it is essential to properly model the uncertainty in these parameters in order to avoid biases on the measurements. Furthermore, we are interested to know how neglecting light-cone effects can influence the best-fit bias on the growth rate, assuming the full model of lensing effects and magnification bias at low-z.

The precision on RSD can be improved by including the vast amount of information available in the smaller scales of the non-linear regime. There have been great progress in modelling the non-linear scales and the "finger-of-god" effect in Fourier space. However, in order to accomplish this in harmonic space, more work should be done regarding the theoretical modelling of non-linear scales in the angular power spectrum. In [119] they found that very narrow bin widths can introduce non-linear effects into the large scale effects, which can significantly influence the ultra-large scale parameters like $f_{\rm NL}$. This means that in future work we will have to consider these effects modelling the precision using very thin bins in C_ℓ.

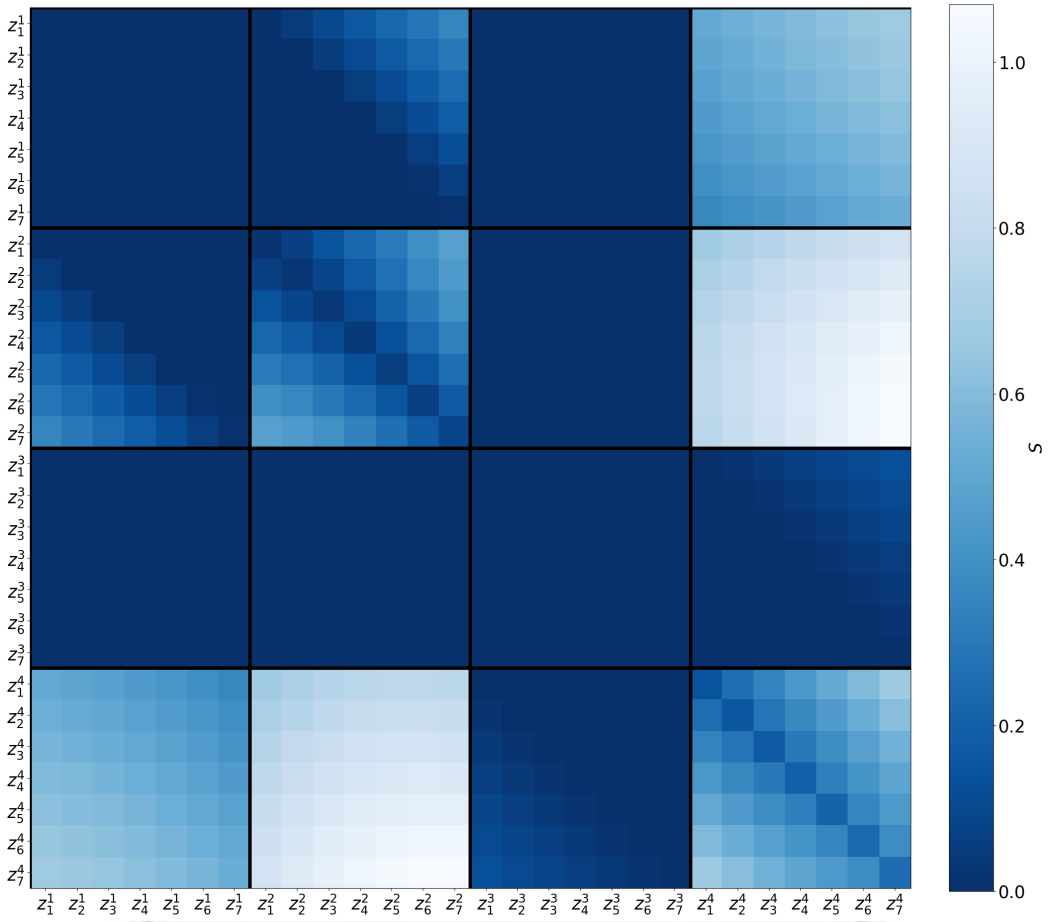

Fig. 6.1 Signal-to-noise $S^{AB}(\theta, z_i^A, z_j^B)$ computed in (5.2) for the lensing magnification contribution ($\theta = \varepsilon_{\rm L}$) for the total survey combination $1 \otimes 2 \otimes 3 \otimes 4 = \text{IM2} \otimes \text{BGS} \otimes \text{IM1} \otimes \text{H}\alpha$. The low-$z$ overlap $1 \otimes 2 = \text{IM2} \otimes \text{BGS}$ for $0.35 < z < 0.56$, is correlated with the high-z overlap $3 \otimes 4 = \text{IM1} \otimes \text{H}\alpha$ for $0.90 < z < 1.11$. Colour bar shows the signal-to-noise.

Lastly, we should be able to further improve constraints by considering the correlation between multiple photometric and spectroscopic surveys. By including several different tracers from various different types of cosmological surveys and redshift binning configurations, we should be able to optimise the constraints on ultra-large scale parameters, without the loss of precision on parameters dependent on peculiar velocity field. In other words, the wide redshift bins of a photometric survey will reduce the shot-noise, such that the large scale observables like $f_{\rm NL}$ and $A_{\rm D}$ can better benefit from the cancellation of cosmic variance. Simultaneously, we can include spectroscopic surveys with a much thinner z-bins to provide information on the peculiar velocity fields via RSD.

Additionally, we can include a CMB survey in the cross-correlation, which will naturally add the priors from Planck 2018, as well as include extra information on lensing magnification. Figure 6.1 makes it apparent that most of the information comes from the correlation between the optical galaxy survey $2 \otimes 4 = \mathrm{BGS} \otimes \mathrm{H}\alpha$, which is not unexpected. A significant amount of information is coming from the high-z galaxies lensed by the low-z IM, i.e. $1 \otimes 4 = \mathrm{IM2} \otimes \mathrm{H}\alpha$, which is perhaps not so intuitive. As explained before, it is the Hα galaxies at z_i being lensed by HI distribution at $z_j < z_i$. By adding the CMB lensing, we will receive a lensing signal from all surveys over the entire redshift range in the multi-tracer - since the CMB photons transverse from deeper in redshift, they will be lensed by all the matter along the way. Therefore, we can extract information on κ from the entire volume of the massive HI IM surveys.

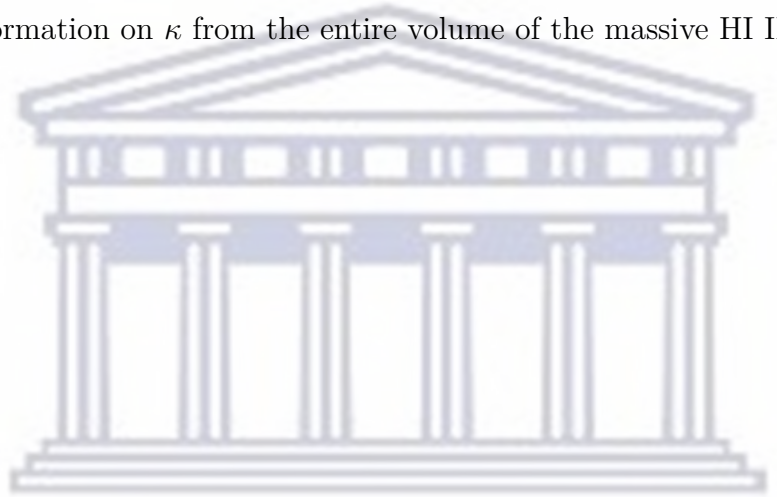

References

[1] J. Fonseca, J.-A. Viljoen and R. Maartens, *Constraints on the growth rate using the observed galaxy power spectrum*, *JCAP* **1912** (2019) 028 [1907.02975].

[2] J.-A. Viljoen, J. Fonseca and R. Maartens, *Constraining the growth rate by combining multiple future surveys*, *JCAP* **09** (2020) 054 [2007.04656].

[3] R. Maartens, J. Fonseca, S. Camera, S. Jolicoeur, J.-A. Viljoen and C. Clarkson, *Magnification and evolution biases in large-scale structure surveys*, *JCAP* **12** (2021) 009 [2107.13401].

[4] J.-A. Viljoen, J. Fonseca and R. Maartens, *Multi-wavelength spectroscopic probes: prospects for primordial non-Gaussianity and relativistic effects*, *JCAP* **11** (2021) 010 [2107.14057].

[5] J.-A. Viljoen, J. Fonseca and R. Maartens, *Multi-wavelength spectroscopic probes: biases from neglecting light-cone effects*, *JCAP* **12** (2021) 004 [2108.05746].

[6] COBE collaboration, *Structure in the COBE differential microwave radiometer first year maps*, *Astrophys. J. Lett.* **396** (1992) L1.

[7] Boomerang collaboration, *A Flat universe from high resolution maps of the cosmic microwave background radiation*, *Nature* **404** (2000) 955 [astro-ph/0004404].

[8] WMAP collaboration, *First year Wilkinson Microwave Anisotropy Probe (WMAP) observations: Determination of cosmological parameters*, *Astrophys. J. Suppl.* **148** (2003) 175 [astro-ph/0302209].

[9] Planck Collaboration, P. A. R. Ade, N. Aghanim, M. Arnaud, F. Arroja, M. Ashdown et al., *Planck 2015 results. XVII. Constraints on primordial non-Gaussianity*, *arXiv:1502.01592* (2015) [1502.01592].

[10] Planck collaboration, *Planck 2018 results. IX. Constraints on primordial non-Gaussianity*, *Astron. Astrophys.* **641** (2020) A9 [1905.05697].

[11] S. P. Driver and Gama Team, *Galaxy and Mass Assembly (GAMA)*, *Anglo-Australian Observatory Epping Newsletter* **114** (2008) 3.

[12] I. K. Baldry, A. S. G. Robotham, D. T. Hill, S. P. Driver, J. Liske, P. Norberg et al., *Galaxy and mass assembly (gama): the input catalogue and star-galaxy separation*, *Monthly Notices of the Royal Astronomical Society* (2010) .

[13] J. Loveday et al., *Galaxy and Mass Assembly (GAMA): ugriz galaxy luminosity functions*, *Mon. Not. Roy. Astron. Soc.* **420** (2012) 1239 [1111.0166].

[14] SDSS collaboration, *Spectroscopic Target Selection in the Sloan Digital Sky Survey: The Main Galaxy Sample*, *Astron. J.* **124** (2002) 1810 [astro-ph/0206225].

[15] K. S. Dawson, D. J. Schlegel, C. P. Ahn, S. F. Anderson, É. Aubourg, S. Bailey et al., *The Baryon Oscillation Spectroscopic Survey of SDSS-III*, *The Astronomical Journal* **145** (2013) 10 [1208.0022].

[16] BOSS collaboration, *Large-scale clustering of Lyman emission intensity from SDSS/BOSS*, *Mon. Not. Roy. Astron. Soc.* **457** (2016) 3541 [1504.04088].

[17] A. Loureiro et al., *ZXCorr: Cosmological Measurements from Angular Power Spectra Analysis of BOSS DR12 Tomography*, *Mon. Not. Roy. Astron. Soc.* **485** (2019) 326 [1809.07204].

[18] E. Castorina et al., *Redshift-weighted constraints on primordial non-Gaussianity from the clustering of the eBOSS DR14 quasars in Fourier space*, *JCAP* **09** (2019) 010 [1904.08859].

[19] E.-M. Mueller et al., *The clustering of galaxies in the completed SDSS-IV extended Baryon Oscillation Spectroscopic Survey: Primordial non-Gaussianity in Fourier Space*, 2106.13725.

[20] C. Blake et al., *The WiggleZ Dark Energy Survey: mapping the distance-redshift relation with baryon acoustic oscillations*, *Mon. Not. Roy. Astron. Soc.* **418** (2011) 1707 [1108.2635].

[21] C. Blake et al., *The WiggleZ Dark Energy Survey: Joint measurements of the expansion and growth history at $z < 1$*, *Mon. Not. Roy. Astron. Soc.* **425** (2012) 405 [1204.3674].

[22] N. Bartolo, E. Komatsu, S. Matarrese and A. Riotto, *Non-Gaussianity from inflation: Theory and observations*, *Phys. Rept.* **402** (2004) 103 [astro-ph/0406398].

[23] T. Clifton, P. G. Ferreira, A. Padilla and C. Skordis, *Modified Gravity and Cosmology*, *Phys. Rept.* **513** (2012) 1 [1106.2476].

[24] K. Koyama, *Cosmological Tests of Modified Gravity*, *Rept. Prog. Phys.* **79** (2016) 046902 [1504.04623].

[25] D. Langlois, *Dark energy and modified gravity in degenerate higher-order scalar–tensor (DHOST) theories: A review*, *Int. J. Mod. Phys.* **D28** (2019) 1942006 [1811.06271].

[26] U. Seljak, *Extracting primordial non-gaussianity without cosmic variance*, *Phys. Rev. Lett.* **102** (2009) 021302 [0807.1770].

[27] P. McDonald and U. Seljak, *How to measure redshift-space distortions without sample variance*, *JCAP* **0910** (2009) 007 [0810.0323].

[28] B. F. Schutz, *A FIRST COURSE IN GENERAL RELATIVITY*. Cambridge Univ. Pr., Cambridge, UK, 1985.

[29] P. Peter and J.-P. Uzan, *Primordial Cosmology*, Oxford Graduate Texts. Oxford University Press, 2, 2013.

[30] G. Ellis, R. Maartens and M. MacCallum, *Relativistic cosmology*. Cambridge University Press, United Kingdom, 2012, 10.1017/CBO9781139014403.

[31] A. G. Lemaître, *A Homogeneous Universe of Constant Mass and Increasing Radius accounting for the Radial Velocity of Extra-galactic Nebulæ*, *Monthly Notices of the Royal Astronomical Society* **91** (1931) 483.

[32] T. M. Davis and C. H. Lineweaver, *Expanding confusion: common misconceptions of cosmological horizons and the superluminal expansion of the universe*, *Publ. Astron. Soc. Austral.* **21** (2004) 97 [astro-ph/0310808].

[33] S. Dodelson, *Modern cosmology*. 2003.

[34] A. A. Starobinsky, *A New Type of Isotropic Cosmological Models Without Singularity*, pp. 771–774. 1996. 10.1142/9789814317344_0079.

[35] A. H. Guth, *Inflationary universe: A possible solution to the horizon and flatness problems*, *Phys. Rev. D* **23** (1981) 347.

[36] A. D. Linde, *A new inflationary universe scenario: A possible solution of the horizon, flatness, homogeneity, isotropy and primordial monopole problems*, *Physics Letters B* **108** (1982) 389.

[37] A. Albrecht and P. J. Steinhardt, *Cosmology for grand unified theories with radiatively induced symmetry breaking*, *Phys. Rev. Lett.* **48** (1982) 1220.

[38] P. Svrcek and E. Witten, *Axions In String Theory*, *JHEP* **06** (2006) 051 [hep-th/0605206].

[39] S. Dimopoulos, S. Kachru, J. McGreevy and J. G. Wacker, *N-flation*, *JCAP* **08** (2008) 003 [hep-th/0507205].

[40] A. Challinor and A. Lewis, *The linear power spectrum of observed source number counts*, *Phys. Rev. D* **84** (2011) 043516 [1105.5292].

[41] M. Bruni, R. Crittenden, K. Koyama, R. Maartens, C. Pitrou and D. Wands, *Disentangling non-Gaussianity, bias and GR effects in the galaxy distribution*, *Phys. Rev.* **D85** (2012) 041301 [1106.3999].

[42] D. Jeong, F. Schmidt and C. M. Hirata, *Large-scale clustering of galaxies in general relativity*, *Phys. Rev.* **D85** (2012) 023504 [1107.5427].

[43] D. Alonso, P. Bull, P. G. Ferreira, R. Maartens and M. Santos, *Ultra large-scale cosmology in next-generation experiments with single tracers*, *Astrophys. J.* **814** (2015) 145 [1505.07596].

[44] A. Barreira, G. Cabass, F. Schmidt, A. Pillepich and D. Nelson, *Galaxy bias and primordial non-Gaussianity: insights from galaxy formation simulations with IllustrisTNG*, *JCAP* **12** (2020) 013 [2006.09368].

[45] A. Barreira, *On the impact of galaxy bias uncertainties on primordial non-Gaussianity constraints*, *JCAP* **12** (2020) 031 [2009.06622].

[46] A. Barreira, *Predictions for local PNG bias in the galaxy power spectrum and bispectrum and the consequences for $f_{\rm NL}$ constraints*, 2107.06887.

[47] S. Camera, M. G. Santos and R. Maartens, *Probing primordial non-Gaussianity with SKA galaxy redshift surveys: a fully relativistic analysis*, *Mon. Not. Roy. Astron. Soc.* **448** (2015c) 1035 [1409.8286].

[48] R. Maartens, S. Jolicoeur, O. Umeh, E. M. De Weerd and C. Clarkson, *Local primordial non-Gaussianity in the relativistic galaxy bispectrum*, *JCAP* **04** (2021) 013 [2011.13660].

[49] R. de Putter, J. Gleyzes and O. Doré, *Next non-Gaussianity frontier: What can a measurement with (fNL)1 tell us about multifield inflation?*, *Phys. Rev.* **D95** (2017) 123507 [1612.05248].

[50] V. Springel, *The Cosmological simulation code GADGET-2*, *Mon. Not. Roy. Astron. Soc.* **364** (2005) 1105 [astro-ph/0505010].

[51] Y.-S. Song and W. J. Percival, *Reconstructing the history of structure formation using Redshift Distortions*, *JCAP* **10** (2009) 004 [0807.0810].

[52] A. Raccanelli, D. Bertacca, D. Pietrobon, F. Schmidt, L. Samushia, N. Bartolo et al., *Testing Gravity Using Large-Scale Redshift-Space Distortions*, *Mon. Not. Roy. Astron. Soc.* **436** (2013) 89 [1207.0500].

[53] P. J. E. Peebles, *The large-scale structure of the universe*. 1980.

[54] N. Frusciante and L. Perenon, *Effective Field Theory of Dark Energy: a Review*, *Phys. Rept.* **857** (2020) 1 [1907.03150].

[55] L. Guzzo et al., *A test of the nature of cosmic acceleration using galaxy redshift distortions*, *Nature* **451** (2008) 541 [0802.1944].

[56] A. Hamilton, *Linear redshift distortions: A review*, *arXiv: Astrophysics* **231** (1997) 185.

[57] N. Kaiser, *Clustering in real space and in redshift space*, *Mon. Not. Roy. Astron. Soc.* **227** (1987) 1.

[58] J. A. Peacock et al., *A Measurement of the cosmological mass density from clustering in the 2dF Galaxy Redshift Survey*, *Nature* **410** (2001) 169 [astro-ph/0103143].

[59] J. A. Peacock, *Errors on the measurement of via cosmological dipoles*, *Monthly Notices of the Royal Astronomical Society* **258** (1992) 581.

[60] C. Bonvin, S. Andrianomena, D. Bacon, C. Clarkson, R. Maartens, T. Moloi et al., *Dipolar modulation in the size of galaxies: The effect of Doppler magnification*, *Mon. Not. Roy. Astron. Soc.* **472** (2017) 3936 [1610.05946].

[61] C. Bonvin, *Effect of Peculiar Motion in Weak Lensing*, *Phys. Rev.* **D78** (2008) 123530 [0810.0180].

[62] D. J. Bacon, S. Andrianomena, C. Clarkson, K. Bolejko and R. Maartens, *Cosmology with Doppler Lensing*, *Mon. Not. Roy. Astron. Soc.* **443** (2014) 1900 [1401.3694].

[63] A. Raccanelli, D. Bertacca, D. Jeong, M. C. Neyrinck and A. S. Szalay, *Doppler term in the galaxy two-point correlation function: wide-angle, velocity, Doppler lensing and cosmic acceleration effects*, *Phys. Dark Univ.* **19** (2018) 109 [1602.03186].

[64] E. Di Dio and U. s. Seljak, *The relativistic dipole and gravitational redshift on LSS*, *JCAP* **04** (2019) 050 [1811.03054].

[65] M. S. Wang, F. Beutler and D. Bacon, *Impact of Relativistic Effects on the Primordial Non-Gaussianity Signature in the Large-Scale Clustering of Quasars*, *Mon. Not. Roy. Astron. Soc.* **499** (2020) 2598 [2007.01802].

[66] F. Beutler and E. Di Dio, *Modeling relativistic contributions to the halo power spectrum dipole*, *JCAP* **07** (2020) 048 [2004.08014].

[67] P. McDonald, *Gravitational redshift and other redshift-space distortions of the imaginary part of the power spectrum*, *JCAP* **0911** (2009) 026 [0907.5220].

[68] C. Bonvin, L. Hui and E. Gaztanaga, *Optimising the measurement of relativistic distortions in large-scale structure*, *JCAP* **1608** (2016) 021 [1512.03566].

[69] A. Hall and C. Bonvin, *Measuring cosmic velocities with 21 cm intensity mapping and galaxy redshift survey cross-correlation dipoles*, *Phys. Rev.* **D95** (2017) 043530 [1609.09252].

[70] L. R. Abramo and D. Bertacca, *Disentangling the effects of Doppler velocity and primordial non-Gaussianity in galaxy power spectra*, *Phys. Rev.* **D96** (2017) 123535 [1706.01834].

[71] F. Lepori, E. Di Dio, E. Villa and M. Viel, *Optimal galaxy survey for detecting the dipole in the cross-correlation with 21 cm Intensity Mapping*, *JCAP* **1805** (2018) 043 [1709.03523].

[72] C. Bonvin and P. Fleury, *Testing the equivalence principle on cosmological scales*, *JCAP* **05** (2018) 061 [1803.02771].

[73] F. O. Franco, C. Bonvin and C. Clarkson, *A null test to probe the scale-dependence of the growth of structure as a test of General Relativity*, *Mon. Not. Roy. Astron. Soc.* **492** (2020) L34 [1906.02217].

[74] C. Clarkson, E. M. De Weerd, S. Jolicoeur, R. Maartens and O. Umeh, *The dipole of the galaxy bispectrum*, *Mon. Not. Roy. Astron. Soc.* **486** (2019) L101 [1812.09512].

[75] R. Maartens, S. Jolicoeur, O. Umeh, E. M. De Weerd, C. Clarkson and S. Camera, *Detecting the relativistic galaxy bispectrum*, *JCAP* **03** (2020) 065 [1911.02398].

[76] S. Jolicoeur, R. Maartens, E. M. De Weerd, O. Umeh, C. Clarkson and S. Camera, *Detecting the relativistic bispectrum in 21cm intensity maps*, *JCAP* (2021) in press [2009.06197].

[77] O. Umeh, K. Koyama and R. Crittenden, *Testing the equivalence principle on cosmological scales using the odd multipoles of galaxy cross-power spectrum and bispectrum*, 2011.05876.

[78] F. Montanari and R. Durrer, *Measuring the lensing potential with tomographic galaxy number counts*, *JCAP* **10** (2015) 070 [1506.01369].

[79] W. Cardona, R. Durrer, M. Kunz and F. Montanari, *Lensing convergence and the neutrino mass scale in galaxy redshift surveys*, *Phys. Rev.* **D94** (2016) 043007 [1603.06481].

[80] E. Villa, E. Di Dio and F. Lepori, *Lensing convergence in galaxy clustering in ΛCDM and beyond*, *JCAP* **1804** (2018) 033 [1711.07466].

[81] M. Ballardini and R. Maartens, *Measuring ISW with next-generation radio surveys*, *Mon. Not. Roy. Astron. Soc.* **485** (2019) 1339 [1812.01636].

[82] M. Jalilvand, E. Majerotto, C. Bonvin, F. Lacasa, M. Kunz, W. Naidoo et al., *New Estimator for Gravitational Lensing Using Galaxy and Intensity Mapping Surveys*, *Phys. Rev. Lett.* **124** (2020) 031101 [1907.00071].

[83] A. Witzemann, A. Pourtsidou and M. G. Santos, *Prospects for cosmic magnification measurements using H i intensity mapping*, *Mon. Not. Roy. Astron. Soc.* **496** (2020) 1959 [1907.00755].

[84] G. Jelic-Cizmek, F. Lepori, C. Bonvin and R. Durrer, *On the importance of lensing for galaxy clustering in photometric and spectroscopic surveys*, *JCAP* **04** (2021) 055 [2004.12981].

[85] T. Namikawa, T. Okamura and A. Taruya, *Magnification effect on the detection of primordial non-Gaussianity from photometric surveys*, *Phys. Rev.* **D83** (2011) 123514 [1103.1118].

[86] S. Camera, R. Maartens and M. G. Santos, *Einstein's legacy in galaxy surveys*, *Mon. Not. Roy. Astron. Soc.* **451** (2015) L80 [1412.4781].

[87] C. S. Lorenz, D. Alonso and P. G. Ferreira, *Impact of relativistic effects on cosmological parameter estimation*, *Phys. Rev. D* **97** (2018) 023537 [1710.02477].

[88] J. L. Bernal, N. Bellomo, A. Raccanelli and L. Verde, *Beware of commonly used approximations. Part II. Estimating systematic biases in the best-fit parameters*, *JCAP* **10** (2020) 017 [2005.09666].

[89] L. D. Ferramacho, M. G. Santos, M. J. Jarvis and S. Camera, *Radio galaxy populations and the multitracer technique: pushing the limits on primordial non-Gaussianity*, *Mon. Not. Roy. Astron. Soc.* **442** (2014) 2511 [1402.2290].

[90] D. Yamauchi, K. Takahashi and M. Oguri, *Constraining primordial non-Gaussianity via a multitracer technique with surveys by Euclid and the Square Kilometre Array*, *Phys. Rev.* **D90** (2014) 083520 [1407.5453].

[91] D. Alonso and P. G. Ferreira, *Constraining ultralarge-scale cosmology with multiple tracers in optical and radio surveys*, *Phys. Rev.* **D92** (2015) 063525 [1507.03550].

[92] J. Fonseca, S. Camera, M. Santos and R. Maartens, *Hunting down horizon-scale effects with multi-wavelength surveys*, *Astrophys. J.* **812** (2015) L22 [1507.04605].

[93] J. Fonseca, R. Maartens and M. G. Santos, *Probing the primordial Universe with MeerKAT and DES*, *Mon. Not. Roy. Astron. Soc.* **466** (2017) 2780 [1611.01322].

[94] J. Fonseca, R. Maartens and M. G. Santos, *Synergies between intensity maps of hydrogen lines*, *Mon. Not. Roy. Astron. Soc.* **479** (2018) 3490 [1803.07077].

[95] SKA collaboration, *Cosmology with Phase 1 of the Square Kilometre Array: Red Book 2018: Technical specifications and performance forecasts*, *Publ. Astron. Soc. Austral.* **37** (2020) e007 [1811.02743].

[96] Z. Gomes, S. Camera, M. J. Jarvis, C. Hale and J. Fonseca, *Non-Gaussianity constraints using future radio continuum surveys and the multitracer technique*, *Mon. Not. Roy. Astron. Soc.* **492** (2020) 1513 [1912.08362].

[97] M. Ballardini, W. L. Matthewson and R. Maartens, *Constraining primordial non-Gaussianity using two galaxy surveys and CMB lensing*, *Mon. Not. Roy. Astron. Soc.* **489** (2019) 1950 [1906.04730].

[98] J. R. Bermejo-Climent, M. Ballardini, F. Finelli, D. Paoletti, R. Maartens, J. A. Rubiño Martín et al., *Cosmological parameter forecasts by a joint 2D tomographic approach to CMB and galaxy clustering*, *Phys. Rev. D* **103** (2021) 103502 [2106.05267].

[99] C. Alcock and B. Paczynski, *An evolution free test for non-zero cosmological constant*, *Nature* **281** (1979) 358.

[100] R. Ruggeri, W. J. Percival, E.-M. Mueller, H. Gil-Marin, F. Zhu, N. Padmanabhan et al., *The extended Baryon Oscillation Spectroscopic Survey: testing a new approach to measure the evolution of the structure growth*, *Mon. Not. Roy. Astron. Soc.* **484** (2019) 4100 [1712.03997].

[101] C. Bonvin and R. Durrer, *What galaxy surveys really measure*, *Phys. Rev.* **D84** (2011) 063505 [1105.5280].

[102] E. Di Dio, F. Montanari, R. Durrer and J. Lesgourgues, *Cosmological Parameter Estimation with Large Scale Structure Observations*, *JCAP* **1401** (2014) 042 [1308.6186].

[103] V. Tansella, C. Bonvin, R. Durrer, B. Ghosh and E. Sellentin, *The full-sky relativistic correlation function and power spectrum of galaxy number counts. Part I: theoretical aspects*, *JCAP* **1803** (2018) 019 [1708.00492].

[104] E. C. Cunningham, N. Garavito-Camargo, A. J. Deason, K. V. Johnston, D. Erkal, C. F. P. Laporte et al., *Quantifying the Stellar Halo's Response to the LMC's Infall with Spherical Harmonics*, *Astrophys. J.* **898** (2020) 4 [2006.08621].

[105] C. Bonvin, *Isolating relativistic effects in large-scale structure*, *Class. Quant. Grav.* **31** (2014) 234002 [1409.2224].

[106] J. Asorey, M. Crocce, E. Gaztanaga and A. Lewis, *Recovering 3D clustering information with angular correlations*, *Mon. Not. Roy. Astron. Soc.* **427** (2012) 1891 [1207.6487].

[107] J. E. Campagne, J. Neveu and S. Plaszczynski, *Angpow: a software for the fast computation of accurate tomographic power spectra*, *Astron. Astrophys.* **602** (2017) A72 [1701.03592].

[108] V. Assassi, M. Simonovi and M. Zaldarriaga, *Efficient evaluation of angular power spectra and bispectra*, *JCAP* **1711** (2017) 054 [1705.05022].

[109] H. S. Grasshorn Gebhardt and D. Jeong, *Fast and accurate computation of projected two-point functions*, *Phys. Rev.* **D97** (2018) 023504 [1709.02401].

[110] S. Camera, J. Fonseca, R. Maartens and M. G. Santos, *Optimized angular power spectra for spectroscopic galaxy surveys*, *Mon. Not. Roy. Astron. Soc.* **481** (2018) 1251 [1803.10773].

[111] N. Schneberg, M. Simonovic, J. Lesgourgues and M. Zaldarriaga, *Beyond the traditional Line-of-Sight approach of cosmological angular statistics*, *JCAP* **1810** (2018) 047 [1807.09540].

[112] LSST Dark Energy Science collaboration, *A unified pseudo-C_ℓ framework*, *Mon. Not. Roy. Astron. Soc.* **484** (2019) 4127 [1809.09603].

[113] K. Tanidis and S. Camera, *Developing a unified pipeline for large-scale structure data analysis with angular power spectra – I. The importance of redshift-space distortions for galaxy number counts*, *Mon. Not. Roy. Astron. Soc.* **489** (2019) 3385 [1902.07226].

[114] L. R. Abramo and K. E. Leonard, *Why multi-tracer surveys beat cosmic variance*, *Mon. Not. Roy. Astron. Soc.* **432** (2013) 318 [1302.5444].

[115] A. Witzemann, D. Alonso, J. Fonseca and M. G. Santos, *Simulated multitracer analyses with HI intensity mapping*, *Mon. Not. Roy. Astron. Soc.* **485** (2019) 5519 [1808.03093].

[116] VIRGO Consortium collaboration, *Stable clustering, the halo model and nonlinear cosmological power spectra*, *Mon. Not. Roy. Astron. Soc.* **341** (2003) 1311 [astro-ph/0207664].

[117] Y. Zhang, A. R. Pullen and A. S. Maniyar, *Joint analyses of 2D CMB lensing and 3D galaxy clustering in spherical Fourier-Bessel basis*, 2110.00872.

[118] P. L. Taylor et al., *Euclid: Forecasts for k-cut* 3×2 *Point Statistics*, 2012.04672.

[119] W. L. Matthewson and R. Durrer, *Small scale effects in the observable power spectrum at large angular scales*, 2107.00467.

[120] M. Martinelli, R. Dalal, F. Majidi, Y. Akrami, S. Camera and E. Sellentin, *Ultra-large-scale approximations and galaxy clustering: debiasing constraints on cosmological parameters*, 2106.15604.

[121] A. F. Heavens, T. Kitching and L. Verde, *On model selection forecasting, Dark Energy and modified gravity*, *Mon. Not. Roy. Astron. Soc.* **380** (2007) 1029 [astro-ph/0703191].

[122] S. Camera, C. Carbone, C. Fedeli and L. Moscardini, *Neglecting Primordial non-Gaussianity Threatens Future Cosmological Experiment Accuracy*, *Phys. Rev.* **D91** (2015) 043533 [1412.5172].

[123] J. Fonseca and M. Liguori, *Measuring ultralarge scale effects in the presence of 21 cm intensity mapping foregrounds*, *Mon. Not. Roy. Astron. Soc.* **504** (2021) 267 [2011.11510].

[124] D. Bertacca, *Observed galaxy number counts on the light cone up to second order: III. Magnification bias*, *Class. Quant. Grav.* **32** (2015) 195011 [1409.2024].

[125] Euclid collaboration, *Euclid preparation: VII. Forecast validation for Euclid cosmological probes*, *Astron. Astrophys.* **642** (2020) A191 [1910.09273].

[126] L. Pozzetti, C. M. Hirata, J. E. Geach, A. Cimatti, C. Baugh, O. Cucciati et al., *Modelling the number density of Hα emitters for future spectroscopic near-IR space missions*, *Astron. Astrophys.* **590** (2016) A3 [1603.01453].

[127] DESI collaboration, *The DESI Experiment Part I: Science,Targeting, and Survey Design*, 1611.00036.

[128] O. Ruiz-Macias, P. Zarrouk, S. Cole, C. M. Baugh, P. Norberg, J. Lucey et al., *Characterizing the target selection pipeline for the Dark Energy Spectroscopic Instrument Bright Galaxy Survey*, *"Mon. Not. Roy. Astron. Soc."* **502** (2021) 4328 [2007.14950].

[129] J. Loveday, P. Norberg, I. K. Baldry, S. P. Driver, A. M. Hopkins, J. A. Peacock et al., *Galaxy and Mass Assembly (GAMA): ugriz galaxy luminosity functions*, *Mon. Not. Roy. Astron. Soc.* **420** (2012) 1239 [1111.0166].

[130] O. Ruiz-Macias, P. Zarrouk, S. Cole, P. Norberg, C. Baugh, D. Brooks et al., *Preliminary Target Selection for the DESI Bright Galaxy Survey (BGS)*, *Research Notes of the American Astronomical Society* **4** (2020) 187 [2010.11283].

[131] F. Villaescusa-Navarro et al., *Ingredients for 21 cm Intensity Mapping*, *Astrophys. J.* **866** (2018) 135 [1804.09180].

[132] P. Bull, *Extending cosmological tests of General Relativity with the Square Kilometre Array*, *Astrophys. J.* **817** (2016) 26 [1509.07562].

[133] S. Yahya, P. Bull, M. G. Santos, M. Silva, R. Maartens, P. Okouma et al., *Cosmological performance of SKA HI galaxy surveys*, *Mon. Not. Roy. Astron. Soc.* **450** (2015) 2251 [1412.4700].

[134] M. G. Santos, D. Alonso, P. Bull, M. Silva and S. Yahya, *HI galaxy simulations for the SKA: number counts and bias*, 1501.03990.

[135] T. Sprenger, M. Archidiacono, T. Brinckmann, S. Clesse and J. Lesgourgues, *Cosmology in the era of Euclid and the Square Kilometre Array*, *JCAP* **02** (2019) 047 [1801.08331].

[136] A. Hall, C. Bonvin and A. Challinor, *Testing General Relativity with 21-cm intensity mapping*, *Phys. Rev.* **D87** (2013) 064026 [1212.0728].

[137] M. Jalilvand, E. Majerotto, R. Durrer and M. Kunz, *Intensity mapping of the 21 cm emission: lensing*, *JCAP* **01** (2019) 020 [1807.01351].

[138] P. C. Breysse, E. D. Kovetz, P. S. Behroozi, L. Dai and M. Kamionkowski, *Insights from probability distribution functions of intensity maps*, *Mon. Not. Roy. Astron. Soc.* **467** (2017) 2996 [1609.01728].

[139] MeerKLASS collaboration, *MeerKLASS: MeerKAT Large Area Synoptic Survey*, 2017, 1709.06099, https://inspirehep.net/record/1624378/files/arXiv:1709.06099.pdf.

[140] L. Knox, *Determination of inflationary observables by cosmic microwave background anisotropy experiments*, *Phys. Rev.* **D52** (1995) 4307 [astro-ph/9504054].

[141] P. Bull, P. G. Ferreira, P. Patel and M. G. Santos, *Late-time cosmology with 21cm intensity mapping experiments*, *Astrophys. J.* **803** (2015) 21 [1405.1452].

[142] M. G. Santos et al., *Cosmology from a SKA HI intensity mapping survey*, *PoS* **AASKA14** (2015) 019 [1501.03989].

[143] E. Castorina and F. Villaescusa-Navarro, *On the spatial distribution of neutral hydrogen in the Universe: bias and shot-noise of the HI power spectrum*, *Mon. Not. Roy. Astron. Soc.* **471** (2017) 1788 [1609.05157].

[144] R. K. Sheth and G. Tormen, *Large scale bias and the peak background split*, *Mon. Not. Roy. Astron. Soc.* **308** (1999) 119 [astro-ph/9901122].

[145] T.-C. Chang, U.-L. Pen, J. B. Peterson and P. McDonald, *Baryon Acoustic Oscillation Intensity Mapping as a Test of Dark Energy*, *Phys. Rev. Lett.* **100** (2008) 091303 [0709.3672].

[146] Y. Gong, X. Chen, M. Silva, A. Cooray and M. G. Santos, *The OH line contamination of 21 cm intensity fluctuation measurements for z=1–4*, *Astrophys. J. Lett.* **740** (2011) L20 [1108.0947].

[147] S. Camera, C. Carbone, C. Fedeli and L. Moscardini, *Neglecting primordial non-Gaussianity threatens future cosmological experiment accuracy*, *Phys. Rev. D* **91** (2015) 043533 [1412.5172].

[148] A. Kehagias, A. M. Dizgah, J. Noreña, H. Perrier and A. Riotto, *A Consistency Relation for the Observed Galaxy Bispectrum and the Local non-Gaussianity from Relativistic Corrections*, *JCAP* **1508** (2015) 018 [1503.04467].

[149] A. Pourtsidou, D. Bacon and R. Crittenden, *HI and cosmological constraints from intensity mapping, optical and CMB surveys*, *Mon. Not. Roy. Astron. Soc.* **470** (2017) 4251 [1610.04189].

[150] S.-F. Chen, E. Castorina, M. White and A. z. Slosar, *Synergies between radio, optical and microwave observations at high redshift*, *JCAP* **07** (2019) 023 [1810.00911].

[151] H. Padmanabhan, A. Refregier and A. Amara, *Cross-correlating 21 cm and galaxy surveys: implications for cosmology and astrophysics*, 1909.11104.

[152] Euclid Collaboration collaboration, *Euclid Definition Study Report*, *ESA-SRE* **12** (2011) [1110.3193].

[153] CHIME Collaboration, "CHIME Overview." http://chime.phas.ubc.ca/CHIME_overview.pdf, 2012.

[154] X. Chen, *The Tianlai Project: a 21CM Cosmology Experiment*, *International Journal of Modern Physics Conference Series* **12** (2012) 256 [1212.6278].

[155] R. A. Battye, M. L. Brown, I. W. A. Browne, R. J. Davis, P. Dewdney, C. Dickinson et al., *BINGO: a single dish approach to 21cm intensity mapping*, 1209.1041.

[156] DESI collaboration, *The DESI Experiment, a whitepaper for Snowmass 2013*, 1308.0847.

[157] O. Doré et al., *Cosmology with the SPHEREX All-Sky Spectral Survey*, 1412.4872.

[158] L. B. Newburgh et al., *HIRAX: A Probe of Dark Energy and Radio Transients*, *Proc. SPIE Int. Soc. Opt. Eng.* **9906** (2016) 99065X [1607.02059].

[159] M. G. Santos, M. Cluver, M. Hilton, M. Jarvis, G. I. G. Jozsa, L. Leeuw et al., *MeerKLASS: MeerKAT Large Area Synoptic Survey*, 1709.06099.

[160] G.-B. Zhao et al., *The clustering of the SDSS-IV extended Baryon Oscillation Spectroscopic Survey DR14 quasar sample: a tomographic measurement of cosmic structure growth and expansion rate based on optimal redshift weights*, *Mon. Not. Roy. Astron. Soc.* **482** (2019) 3497 [1801.03043].

[161] L. Amendola et al., *Cosmology and fundamental physics with the Euclid satellite*, *Living Rev. Rel.* **21** (2018) 2 [1606.00180].

[162] Planck collaboration, *Planck 2018 results. VI. Cosmological parameters*, *Astron. Astrophys.* **641** (2020) A6 [1807.06209].

[163] D. Coe, *Fisher Matrices and Confidence Ellipses: A Quick-Start Guide and Software*, *arXiv e-prints* (2009) arXiv:0906.4123 [0906.4123].

[164] E. Krause and T. Eifler, *Cosmolike – cosmological likelihood analyses for photometric galaxy surveys*, *Mon. Not. Roy. Astron. Soc.* **470** (2017) 2100 [1601.05779].

[165] S. Matarrese and L. Verde, *The effect of primordial non-Gaussianity on halo bias*, *Astrophys. J.* **677** (2008) L77 [0801.4826].

[166] N. Dalal, O. Dore, D. Huterer and A. Shirokov, *The imprints of primordial non-gaussianities on large-scale structure: scale dependent bias and abundance of virialized objects*, *Phys. Rev.* **D77** (2008) 123514 [0710.4560].

[167] B. Leistedt, H. V. Peiris and N. Roth, *Constraints on Primordial Non-Gaussianity from 800 000 Photometric Quasars*, *Phys. Rev. Lett.* **113** (2014) 221301 [1405.4315].

[168] T. Giannantonio, C. Porciani, J. Carron, A. Amara and A. Pillepich, *Constraining primordial non-Gaussianity with future galaxy surveys*, *Mon. Not. Roy. Astron. Soc.* **422** (2012) 2854 [1109.0958].

[169] S. Camera, M. G. Santos, P. G. Ferreira and L. Ferramacho, *Cosmology on Ultra-Large Scales with HI Intensity Mapping: Limits on Primordial non-Gaussianity*, *Phys. Rev. Lett.* **111** (2013) 171302 [1305.6928].

[170] A. Font-Ribera, P. McDonald, N. Mostek, B. A. Reid, H.-J. Seo and A. Slosar, *DESI and other dark energy experiments in the era of neutrino mass measurements*, *JCAP* **05** (2014) 023 [1308.4164].

[171] A. Raccanelli, F. Montanari, D. Bertacca, O. Doré and R. Durrer, *Cosmological Measurements with General Relativistic Galaxy Correlations*, *JCAP* **1605** (2016) 009 [1505.06179].

[172] A. Moradinezhad Dizgah, G. K. Keating and A. Fialkov, *Probing Cosmic Origins with CO and [CII] Emission Lines*, *Astrophys. J. Lett.* **870** (2019) L4 [1801.10178].

[173] N. Hamaus, U. Seljak and V. Desjacques, *Optimal Constraints on Local Primordial Non-Gaussianity from the Two-Point Statistics of Large-Scale Structure*, *Phys. Rev.* **D84** (2011) 083509 [1104.2321].

[174] L. R. Abramo, L. F. Secco and A. Loureiro, *Fourier analysis of multitracer cosmological surveys*, *Mon. Not. Roy. Astron. Soc.* **455** (2016) 3871 [1505.04106].

[175] J. Yoo, N. Hamaus, U. Seljak and M. Zaldarriaga, *Going beyond the Kaiser redshift-space distortion formula: a full general relativistic account of the effects and their detectability in galaxy clustering*, *Phys. Rev.* **D86** (2012) 063514 [1206.5809].

[176] E. Di Dio, H. Perrier, R. Durrer, G. Marozzi, A. Moradinezhad Dizgah, J. Noreña et al., *Non-Gaussianities due to Relativistic Corrections to the Observed Galaxy Bispectrum*, *JCAP* **03** (2017) 006 [1611.03720].

[177] K. Koyama, O. Umeh, R. Maartens and D. Bertacca, *The observed galaxy bispectrum from single-field inflation in the squeezed limit*, *JCAP* **07** (2018) 050 [1805.09189].

[178] E. Castorina and E. di Dio, *The observed galaxy power spectrum in General Relativity*, 2106.08857.

[179] P. L. Taylor, K. Markovič, A. Pourtsidou and E. Huff, *The RSD Sorting Hat: Unmixing Radial Scales in Projection*, 2106.05293.

[180] C. Bonvin, L. Hui and E. Gaztanaga, *Asymmetric galaxy correlation functions*, *Phys. Rev.* **D89** (2014) 083535 [1309.1321].

[181] S. Andrianomena, C. Bonvin, D. Bacon, P. Bull, C. Clarkson, R. Maartens et al., *Testing General Relativity with the Doppler magnification effect*, *Mon. Not. Roy. Astron. Soc.* **488** (2019) 3759 [1810.12793].

[182] E. M. de Weerd, C. Clarkson, S. Jolicoeur, R. Maartens and O. Umeh, *Multipoles of the relativistic galaxy bispectrum*, *JCAP* **05** (2020) 018 [1912.11016].

[183] DESI Collaboration, A. Aghamousa, J. Aguilar, S. Ahlen, S. Alam, L. E. Allen et al., *The DESI Experiment Part I: Science,Targeting, and Survey Design*, *arXiv e-prints* (2016) [1611.00036].

[184] D. Karagiannis, A. Lazanu, M. Liguori, A. Raccanelli, N. Bartolo and L. Verde, *Constraining primordial non-Gaussianity with bispectrum and power spectrum from upcoming optical and radio surveys*, *Mon. Not. Roy. Astron. Soc.* **478** (2018) 1341 [1801.09280].

[185] D. Karagiannis, A. Slosar and M. Liguori, *Forecasts on Primordial non-Gaussianity from 21 cm Intensity Mapping experiments*, *JCAP* **11** (2020) 052 [1911.03964].

[186] D. Karagiannis, J. Fonseca, R. Maartens and S. Camera, *Probing primordial non-Gaussianity with the power spectrum and bispectrum of future 21 cm intensity maps*, *Phys. Dark Univ.* **32** (2021) 100821 [2010.07034].

[187] M. Tellarini, A. J. Ross, G. Tasinato and D. Wands, *Galaxy bispectrum, primordial non-Gaussianity and redshift space distortions*, *JCAP* **06** (2016) 014 [1603.06814].

[188] D. Gualdi, S. Novell, H. Gil-Marín and L. Verde, *Matter trispectrum: theoretical modelling and comparison to N-body simulations*, *JCAP* **01** (2021) 015 [2009.02290].

[189] J. Fonseca and C. Clarkson, *Anti-symmetric clustering signals in the observed power spectrum*, 2107.10803.

[190] M. Rezaie et al., *Primordial non-Gaussianity from the Completed SDSS-IV extended Baryon Oscillation Spectroscopic Survey I: Catalogue Preparation and Systematic Mitigation*, 2106.13724.

[191] M. Spinelli, I. P. Carucci, S. Cunnington, S. E. Harper, M. O. Irfan, J. Fonseca et al., *SKAO HI Intensity Mapping: Blind Foreground Subtraction Challenge*, 2107.10814.

[192] K. Tanidis, S. Camera and D. Parkinson, *Developing a unified pipeline for large-scale structure data analysis with angular power spectra – II. A case study for magnification bias and radio continuum surveys*, *Mon. Not. Roy. Astron. Soc.* **491** (2020) 4869 [1909.10539].

[193] D. Alonso, P. Bull, P. G. Ferreira and M. G. Santos, *Blind foreground subtraction for intensity mapping experiments*, *Mon. Not. Roy. Astron. Soc.* **447** (2015) 400 [1409.8667].

[194] S. Cunnington, S. Camera and A. Pourtsidou, *The degeneracy between primordial non-Gaussianity and foregrounds in 21 cm intensity mapping experiments*, *Mon. Not. Roy. Astron. Soc.* **499** (2020) 4054 [2007.12126].